PERFORMANCE-BASED DESIGN AND EVALUATION OF INNOVATIVE STEEL KNEE BRACED TRUSS MOMENT FRAMES

by

Yuanjie Li

B.Sc., South China University of Technology, 2012

B.Sc., Polytechnic Institute of New York University, 2012

A THESIS SUBMITTED IN PARTIAL FULFILLMENT OF

THE REQUIREMENTS FOR THE DEGREE OF

MASTER OF APPLIED SCIENCE

in

THE FACULTY OF GRADUATE AND POSTDOCTORAL STUDIES

(Civil Engineering)

THE UNIVERSITY OF BRITISH COLUMBIA

(Vancouver)

October 2014

Abstract

Steel truss girders are very economical and practical to span large distances, when used efficiently this can create large interior opening which cannot be economically accomplished by any other structural systems. However, due to lack of ductility in connections and poor element energy dissipation capacity, conventional steel trusses are not suitable for seismic applications. To retain the advantages of steel trusses, a novel and innovative steel structural system, named buckling restrained knee braced truss moment frame (BRKBTMF) system has been introduced and extensively studied in this thesis. The BRKBTMF system utilizes buckling restrained braces (BRBs) as the designated structural elements to dissipate earthquake energy. This allows BRKBTMF to span long distances, while having efficient and robust energy dissipation capacity to resist earthquake loads. More importantly, by using the BRBs as structural fuses, the structural damages can be controlled. This allows the structure to be repaired more efficiently and effectively after the earthquake, which reduces the repair time and repair costs, making the BRKBTMF more resilient towards future earthquakes. This thesis consisted of three parts. First, the performance-based plastic design procedure (PBPD) was applied to design a prototype office building located in Berkeley, California. Nonlinear dynamic analysis was conducted to examine the performance of the BRKBTMF under ranges of earthquakes. The result showed that the PBPD was a viable and efficient deign procedure for the BRKBTMF, where both the drift and strength limits were satisfied without design iterations. Second, new material model and element removal techniques were implemented to model the behavior of BRBs and BRKBTMF, where detailed failure modes could be explicitly modeled. Third, detailed parameter studies, including influence of the BRB hysteresis, BRB configuration, and truss span, were conducted. The parameter studies showed that

these parameters can significantly affect the seismic structural performance of the BRKBTMF system.

Preface

Parts of the work in Chapter 6 and 7 of this thesis have been accepted in the following peer reviewed conference proceeding and journal.

- Chapter 6: Yang, T.Y., and **Li, Y.** (2014). "Influence of BRB Hysteresis of the Seismic Response of Buckling Restrained Knee Braced Truss Moment Frames", *Proceedings*, The 7th European Conference on Steel and Composite Structures, Napoli, Italy, Sept. 10-12, 2014.
- Chapter 7: Yang, T.Y., **Li, Y.**, Leelataviwat, S. (2013). "Performance-Based Design and Optimization of Buckling Restrained Knee Braced Truss Moment Frame," *Journal of Performance of Constructed Facilities*. *(Published online: DOI: 10.1061/(ASCE)CF.1943-5509.0000558*

The author of this thesis was responsible for the literature review, model development, computational analysis, data processing, and result presentation. The manuscripts were drafted by the author of the thesis and revised based on the comments from Prof. Tony Yang from University of British Columbia, Prof. Sutat Leelaviwat from King Mongkut's University of Technology and Prof. S. C. Goel from University of Michigan.

Table of Contents

List of Tables

List of Figures

List of Abbreviations

BRB: buckling restrained brace

BRBF: buckling restrained braced frame

BRKBTMF: buckling restrained knee braced truss moment frame

CBF: concentric braced frame

EBF: Eccentric braced frame

EPP-SDOF: elastic and perfectly plastic single-degree-of-freedom

E-SDOF: equivalent elastic single-degree-of-freedom

FBD: free body diagram

MDOF: multiple-degree-of-freedom structure

MF: typical moment frame

PBEE: performance-based earthquake engineering

PBPD: performance-based plastic design

POE: probability of exceedance

SFRS: seismic force resisting system

SPSW: steel plate shear wall

STMF: special truss moment frame

List of Symbols

b : the material strain hardening ratio

D_0 : the depth of truss

E_0 : the material elastic modulus

E_e : the elastic energy absorbed by the EPP-SDOF system.

E_p : the total plastic energy absorbed by the EPP-SDOF

E_i : the total input energy absorbed by the E-SDOF

E_{sh} : the material post yielding modulus

g : the gravitational constant

h_i : the height from the base to the i^{th} floor

h_j : the heights from ground to the level j

h_n : the heights from ground to the roof (level n)

l_d : the length of the first diagonal member of the steel truss

l_1 : the length of first top chord

l_0 : the undeformed length of the BRB

n : the number of floors

N_{BRB} : the axial strength of the BRBs at the top story (level n)

P_y : the BRB yield strength

P_{max}^{+} : the maximum tension force in BRB

P_{max}^{-} : the maximum compression force in BRB

R : the Bauschinger effect parameter

R_d : the system ductility factor

S_a : the first mode spectral acceleration (in unit of g)

T : the fundamental period of the structure

V_y : the total design based shear of the EPP-SDOF system

V_n : the story shear on the top story

W : the weight of the structure

β : the BRB compression to tension ratio

ω : the strength hardening adjustment factor

w_n : the seismic weights at the roof (level n)

w_j : the seismic weight at the level j

α : the vertical inclination of the BRB (vertical angle between the BRB and the column)

δ : the total BRB deformation

Δ_e : the elastic displacement of the E-SDOF system

Δ_y : the yield displacement of the EPP-SDOF system

Δ_t : the total displacement of the EPP-SDOF system

δ_p : the plastic axial deformation of the BRBs

φ : the angle between the column and diagonal chord

γ : the energy reduction factor of the total elastic energy to be absorbed by the E-SDOF

λ_i : the ratio of the equivalent lateral force at the i^{th} floor with respect to the design base shear

μ_s : the ductility of the EPP-SDOF

μ_s : the plastic inter-story drift ratio

θ_p : the total inter-story drift ratio

μ : the ductility of the structure

Ω : the system overstrength factor

Acknowledgements

I would like to sincerely thank my supervisor Professor Tony Yang. His intelligence, patience, passion, diligence and devotion to research and especially to innovative technologies are merits that I deeply admire. It has been a great honor and pleasure to be his student, and I am looking forward to the future collaborations. I would also like to acknowledge his kind pursuit for financial support for me so that I can continue chasing my goals without burdens. I also appreciate advising from Prof. Sutat Leelaviwat from King Mongkut's University of Technology and Prof. S. C. Goel from University of Michigan and their valuable comments have greatly improved this study.

Furthermore, I would like to thank Mr. Dorian Tung for guiding me on different exciting projects and giving me insight on careers and life. Many thanks also go to my other research colleagues, Lisa Tobber, and Jeremy Atkinson for their valuable input to my research. I also owe a tremendous amount of gratitude to many people including Jiulin Bai, Brook Robazza, Yinlan Shen, Lucy Yan, Xi Chen, Jingjing Liu, Yuxin Pan, Mi Liufor their help in my studies and Ken Taggart, Scott Jackson, Harald Schremp, Bill Leung for their assistance in the structural lab. Special thanks will go to my closest friend Jiyi Zhou for his generous friendship during these two years in Vancouver.

Most of all, I would like to express my gratitude for my parents' unconditional love and support for my education and advice for the time when I faced different challenges. Lastly, I am deeply grateful for my girlfriend Qiqi Jiang for her years of continual love and support.

Dedication

To my parents for their unconditional love and support

Chapter 1 Introduction

1.1 Overview

The design philosophy for earthquake engineering applications is shifting towards more resilient design, where the structural damage can be controlled during the maximum credible earthquake shaking. Resiliency is the ability to recover from a devastating event. The importance of resiliency can be found in 2011 Christchurch, New Zealand earthquake (Eguchi et al., 2012). After the 2011 Christchurch earthquake, up to 50% of the buildings in the Christchurch central business district needed to be demolished. This resulted to over 185 confirmed death and costing $20 billion NZ dollars in direct financial loss. With such widespread damage, long-term recovery issues were critical for this region. It raised the question as how we could design buildings to recover quickly and how we could minimize the repair cost after an earthquake.

Resilient structure can be achieved through the use of designated structural fuses, which can protect the structure from the sudden and infrequent surge of loads created by earthquake. More importantly, by using of designated structural fuses, the damage can be controlled and the fuses can be easily replaced after the earthquake. This minimizes the repair cost of the structure, without the need to overly design the structural system and increase the initial construction cost.

1.2 Review of Pre-qualified Steel Seismic Force Resisting Systems in North America

Over the years, several steel seismic force resisting systems (SFRS) have seen adopted by the steel codes in the United States (AISC, 2010a) and Canada (NBCC, 2010). The following paragraphs summarize the design philosophy of these systems.

1.2.1 Steel Moment Resisting Frame

Moment Resisting Frame (MF) was the one of the most commonly used steel SFRS. It utilized the flexural behavior of beams to dissipate the earthquake energy. It had many significant advantages, including large opening and very flexible with architectural planning. A well designed MF should follow "Strong Column – Weak Beam" mechanism (as shown in Figure 1.1). That was achieved by ensuring the beam can deform inelastically through ductile hinging, while column was capacity designed to be stronger than the beam end moments. In order to achieve a full plastic mechanism, the column bases were detailed to form plastic hinge as well. Prior to the 1994 Northridge earthquake, steel MF was assumed to be superior for earthquake application. However, as reported in FEMA-355C (2000), the beam-column connections exhibited brittle fractures at very low level of plastic demands. This led to brittle behavior of the system. Many researchers proposed various moment connections to increase the connection ductility. This included the end-plate moment connections (Tsai & Popov, 1991), reduced beam section connections (Uang et al., 2000), and welded straight haunch connections (Lee et al., 2003). The tests showed that these improved beam-column connections could achieve higher level of ductility. However, the essential drawbacks of MF was in its low structural stiffness, where the structural design of MF was typically governed by the deflection limit instead of strength. Hence, the use of structural material was usually not optimized. More importantly, the design philosophy did not take the post-earthquake repair into account, making the repair of this system difficult after the earthquake.

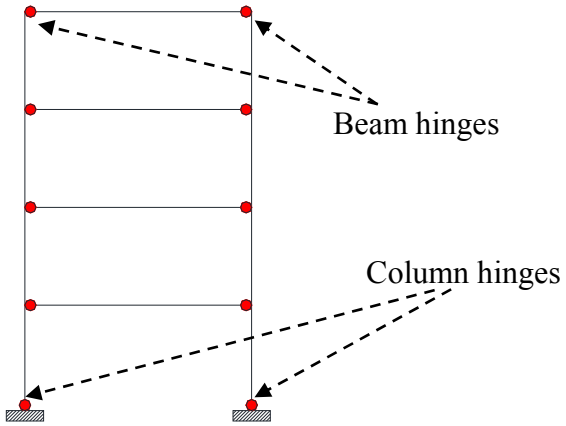

Figure 1.1 Moment resisting frame

1.2.2 Steel Concentrically Braced Frame

Concentrically Braced Frame (CBF) used steel braces to increase the stiffness of the structure (see Figure 1.2). Such system dissipated the earthquake energy by allowing the steel braces to yield in tension and buckle in compression. Because conventional steel brace had higher tension capacity than compression, when the braces were connected in the mid span of the beam, an unbalance force would be created at the mid span of the beam when the brace buckled. Over the last two decades, seismic behaviors of CBF were studied extensively by many researchers (Kim & Choi, 2005; Macrae et al., 2004; Tremblay & Robert, 2001), it was found that conventional CBF were not capable of redistributing the large unbalance vertical forces caused by brace buckling. To mitigate such disadvantage, novel CBFs, suspended zipper braced frames (SZBFs), were developed by researchers (Yang et al., 2009a). Figure 1.2(b) shows that the mechanism of the SZBF. SZBF used intermediate vertical columns to redistribute the unbalance forces to the top story. To prevent the structure from losing all the lateral resistance, the top-story braces were capacity designed to remain elastic. The experimental test showed such design philosophy worked well in redistributing the unbalanced vertical force. Similar to the MF, the design philosophy did

not take the post-earthquake performance into account during the design process. Repair of the CBF would lead to expensive repair cost and long repair time.

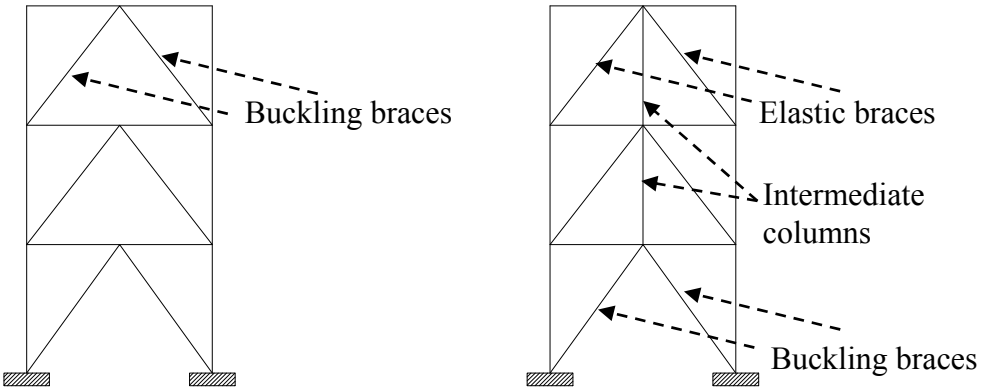

(a) Chevron concentric braced frame (b) Suspended zipper braced frame

Figure 1.2 Concentrically braced frame

1.2.3 Buckling Restrained Braced Frame

Buckling Restrained Braced Frame (BRBF) was an alternative SFRS to solve the vertical unbalance force by using buckling restrained braces (BRBs) to replace the regular buckling braces. Unlike regular buckling braces, BRBs had comparable compression strength as tension. Figure 1.3 shows the configuration of BRBF. The first BRBF research project in North America project started by Clark et al. (1999) . They tested BRBs under cyclic loads. The result showed excellent energy dissipation capability of the BRBs. However, this system was not favorable by architects for its limited openings.

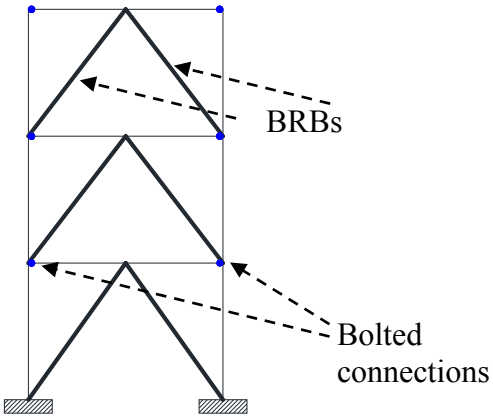

Figure 1.3 Buckling restrained braced frame

1.2.4 Steel Eccentrically Braced Frame

Eccentrically Braced Frame (EBF) was first proposed by Popov (Popov & Engelhart, 1988). This SFRS used stiff braces to yield a portion of the beam. Figure 1.3 shows the different EBF configurations. Depending on the link length, the beam could either fail in shear or flexural, which was known as shear-controlled or flexural-controlled EBF, respectively. Shear-controlled link dissipated the earthquake energy by shearing of the link web. The flexural-controlled link dissipated the earthquake energy by forming moment hinges at the ends of the links. Shear-controlled links were preferred in EBF, because of their excellence in strength, stiffness, and energy dissipation capacity compared to the flexural-controlled links. On the other hand, flexural-controlled links were more favorable by architects for its larger openings. The designated links allowed EBF to dissipate the earthquake energy efficiently, however, as the link was part of the floor beam, it was costly and time consuming to be replaced after an earthquake.

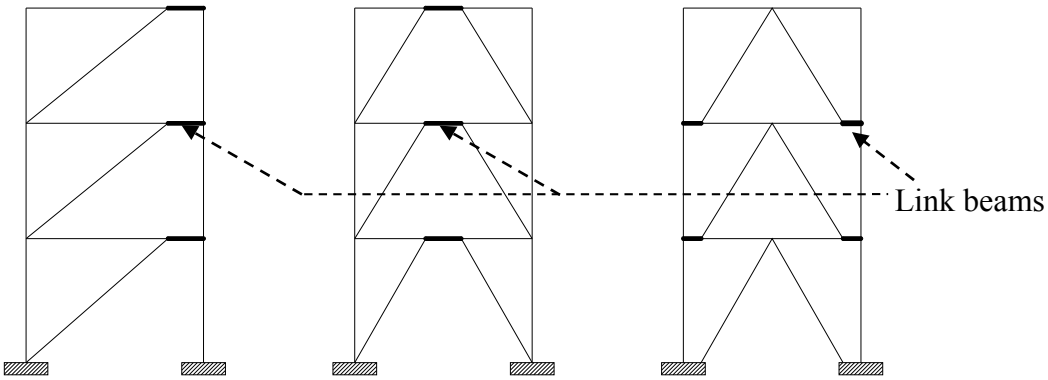

Figure 1.4 Typical bracing arrangement for EBFs

1.2.5 Steel Special Truss Moment Frame

Special truss moment frame (STMF) system was first proposed by Goel and Itani (1994). This system utilized the special segments, as shown in Figure 1.5, to absorb the earthquake energy. Under the earthquake load, the X-diagonals of the special segments were designed to buckle and yield, this resulted in plastic hinges formed at the ends of the special segments. To form the full plastic mechanism, the base of the columns were designed to form the plastic hinges as well. Other than the special segments and column bases, the rest of the structural components were designed to remain elastic. The system had many advantages, including the ability to span long distances and designated energy dissipation zones where damages could be concentrated. However, since the special segments were parts of STMF, they were costly and time consuming to be replaced after earthquake.

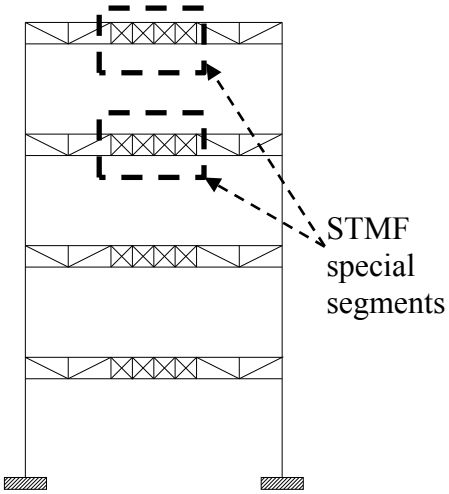

Figure 1.5 Special truss moment frame under earthquake loading

1.2.6 Steel Plate Shear Wall

Steel plate shear wall (SPSW) was another ductile SFRS. It consisted of a steel plate wall, boundary columns and beams. SPSWs were used in the United States since the 1970's and initially used for seismic retrofit of low and median-rise existing hospitals. Nowadays, SPSWs are adopted by tall buildings to resist seismic forces. Figure 1.6 shows the schematic details of SPSW with boundary beams and columns. The benefit of SPSW was that it had high stiffness and could resist larger seismic forces with high stiffness. However, the SPSW may be hard to repair after an earthquake because the boundary elements and shear plates were usually welded together.

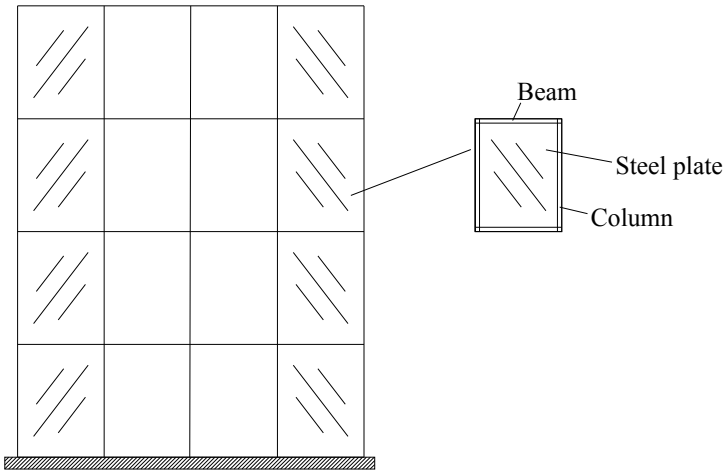

Figure 1.6 Schematic of steel plate shear wall

1.3 Buckling Restrained Knee Braced Truss Moment Frame

Based on the review of the pre-qualified steel SFRS, each system has its advantages and drawbacks. To achieve the objective of resilience, it is necessary to design a structure that can be repaired easily and effectively without significantly affecting the operation of the building after an earthquake. The usage of structural fuses can control the building damage location and allow the structure to be repaired effectively and economically after an earthquake. Inspired by the STMF, an innovative steel SFRS, buckling restrained knee braced truss moment frame (BRKBTMF), is developed. BRKBTMF utilizes the steel trusses to create large interior openings and uses the buckling restrained braces (BRBs) as the designated structural fuses to dissipate the earthquake energy. Figure 1.7 shows the proposed structure.

The development of BRKBTMF was originally initiated by Professors Leelataviwat and Goel as an international collaboration project (Leelataviwat et al., 2012). Since no prior design procedure was established for such novel system, the performance-based plastic design (PBPD) procedure, originally developed by Goel and Leelataviwat (1998), for steel moment frame system,

was modified to design the BRKBTMF (Wongpakdee, 2011). The PBPD procedure used the energy-based plastic design approach to design the structural system effectively. In order to demonstrate the resilience of the proposed structure, the state-of-the-art Performance-Based Earthquake Engineering (PBEE) evaluation framework developed by Yang et al. (2009b) was used to evaluate the repair cost of BRKBTMF under severe earthquakes. This international collaborative project also included small scaled and large scaled sub-assemblage tests led by Prof. Rai in Indian Institute of Technology and Prof. Yang in University of British Columbia, respectively to demonstrate the applicability of the system.

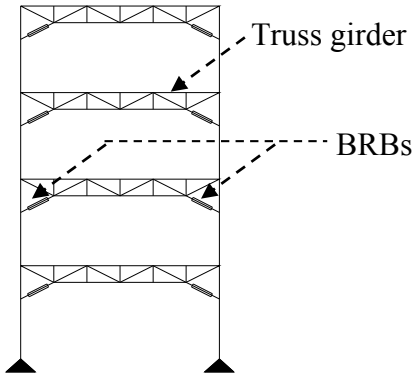

Figure 1.7 BRKBTMF configuration

1.4 Scope of Work

The research presented in this thesis had three objectives:

The first objective was to apply performance based plastic design (PBPD) procedure to design an office building located in Berkeley, California using BRKBTMF. The PBPD procedure developed by Wongpakdee (2011) was modified to design a BRKBTMF building with different BRB inclinations and different truss spans.

The second objective was to develop and calibrate a finite element model of the BRKBTMF system using OpenSees (PEER, 2000). In order to model the asymmetrical kinematic and isotropic behavior of BRB, Steel02 material was modified in OpenSees and calibrated against available test data in the literature. The modified Steel02 allowed users to define an asymmetric properties parameters for the material. Since the failure of the BRBs would lose load resisting capacity once they were fractured, an advanced element removal technique was implemented in OpenSees to appropriately model the impact of the BRB failure.

The third objective was to study the critical parameters of BRKBTMF (this included BRB strain hardening factor, BRB inclination, and truss span length) and apply the PBEE evaluation framework to optimize the BRKBTMF design. Detailed performance assessment in terms of downtime and repair costs was conducted to distinguish the benefit of using BRKBTMF system as an alternative seismic resisting force system.

1.5 Organization of Thesis

Seismic design and performance-based evaluation of BRKBTMF was described in the following eight chapters.

Chapter 2 described the design procedure of BRKBTMF using PBPD method. PBPD used an energy balanced equation to design structural members to satisfy both strength and drift limits without iteration. Detailed design guidelines was provided for practicing engineers to design BRKBTMF.

Chapter 3 described the modeling technique for BRBs and BRKBTMF. Detailed element removal technique was introduced to depict the influence of BRB fracture during dynamic analysis.

Chapter 4 described a prototype office building located in Berkeley, California. Site specific hazard analysis was carried out to select and scale the ground motions used in the analysis. Nonlinear dynamic time history analysis was conducted to study the seismic performance of the prototype building.

Chapter 5 described the theory and application of the performance-based evaluation framework.

Chapters 6 to 8 described the parameters study of the BRKBTMF system. The parameter study included: 1) BRB strain hardening factor; 2) BRB inclination angle; and 3) truss span. Optimal design guidelines to reduce initial and life cycle cost for each parameters were provided.

Chapter 9 presented a summary of research findings, conclusion and a list of topics for future research.

Chapter 2 Seismic Performance-Based Plastic Design (PBPD) Procedure

Performance-based plastic design (PBPD) procedure was originally proposed by Leelataviwat et al. (1999) to design a moment frame building efficiently for seismic application. Compared to the traditional code design procedure, the PBPD procedure had many merits as a thorough design methodology. This chapter first introduced the basic derivation of PBPD procedure, then applied PBPD for the seismic design of BRKBTMF. Design guidelines were also given in this chapter.

2.1 Current Code Practice

It was well known that current code allowed a structure to undergo large inelastic deformation during major seismic event. However, the seismic design approach was primarily based on an equivalent static procedure. In this procedure, the designers calculated the base shear according to the elastic property of the system. This elastic base shear would be reduced by a force modification factor, R (ASCE, 2010) or R_dR_o (NBCC, 2010) depending on the expected structural ductility and overstrength to account for inelastic behaviors during earthquake. After the members were selected to satisfy the strength demand, drift would be checked. If the drift limit was not satisfied, new member sizes would be selected. After some iterations, a set of member sizes would

be selected to satisfy both the strength and drifts. However, this design methodology usually led to "uncontrollable" damages and "unpredictable" damage locations inside the building.

2.2 Design Strategy of PBPD Procedure

In order to achieve more predictable structural performance under strong ground motions, performance-based plastic design (PBPD) was proposed by Goel and Chao (2008). The PBPD method was originally proposed by Goel and Leelataviwat (1998) to design steel moment frame systems. Over the last 15 years, it has been successfully expanded to design steel concentrically braced frames (Chao & Goel, 2006a), eccentrically braced frames (Chao & Goel, 2006b) and special truss moment frames (Chao & Goel, 2008). The PBPD method used pre-selected target drifts and plastic mechanism to define the structural performance. The PBPD procedure assumed the total energy to be dissipated by the multiple-degrees-of-freedom structure (MDOF) could be estimated using an equivalent elastic and perfectly plastic single-degree-of-freedom (EPP-SDOF) system. The total energy to be dissipated by the EPP-SDOF could be estimated using a fraction (γ) of the total elastic energy, E_e to be absorbed by an equivalent elastic single-degree-of-freedom (E-SDOF) system as shown in Figure 2.1. In the figure, Δ_y = yield displacement of the EPP-SDOF system; Δ_e = elastic displacement of the E-SDOF system; Δ_t = ultimate displacement of the EPP-SDOF system; V_y = yield force of the EPP-SDOF system; V_e = elastic force of the E-SDOF system; E_e = elastic energy absorbed by the EPP-SDOF; E_i = total input energy absorbed by the E-SDOF and E_p = total plastic energy absorbed by the EPP-SDOF.

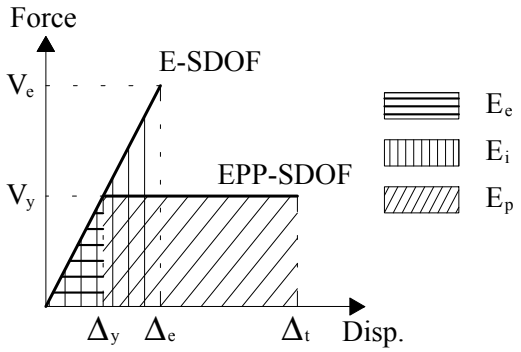

Figure 2.1 Energy balance concept for SDOF

Depending on the period and ductility of the EPP-SDOF, a reduction factor, γ, could be found using Figure 2.2. The reduction factor, γ, was derived by Lee (2002) based on the idealized inelastic spectra published by Newmark and Hall (1982), other inelastic spectra such as the one published by Miranda and Bertero (1994) could also be used. Equation 2.1 shows the energy balanced equation based on Figure 2.1.

$$E_e + E_p = \gamma E_i \qquad \textbf{Equation 2.1}$$

where

$$E_e = \frac{1}{2}\frac{W}{g}\left(\frac{T}{2\pi}\frac{V_y}{W}g\right)^2 \qquad \textbf{Equation 2.2}$$

$$E_i = \frac{1}{2}\frac{W}{g}\left(\frac{T}{2\pi}S_a g\right)^2 \qquad \textbf{Equation 2.3}$$

where W = weight of the structure; V_y = the design base shear; g = the gravitational constant; T = fundamental period of the structure; S_a = the first mode spectral acceleration (in unit of g).

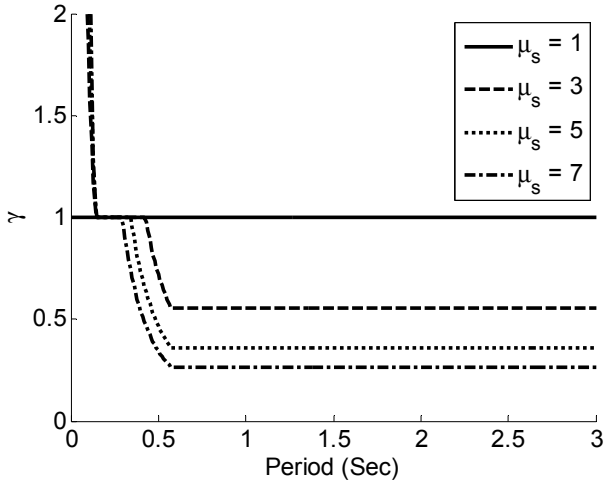

Figure 2.2 Relation of γ, structural period and ductility

Figure 1.7 has shown the configuration of the proposed BRKBTMF. Using the plastic mechanism shown in Figure 2.3 (a desired failure mode), the total energy to be dissipated by the MDOF is given by:

$$E_p = V_y \left(\sum_{i=1}^{n} \lambda_i h_i \right) \theta_p \qquad \textbf{Equation 2.4}$$

where V_y = design base shear; λ_i = the ratio of the equivalent lateral force at the i^{th} floor with respect to the design base shear; h_i = height from the base to the i^{th} floor; n = number of floors; θ_p = plastic inter-story drift ratio;

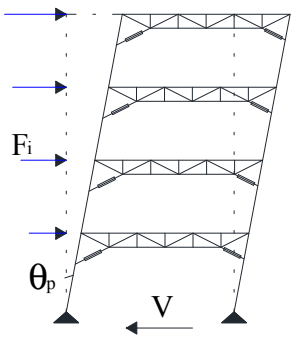

Figure 2.3 BRKBTMF desired plastic mechanism

Substitute Equation 2.2 and Equation 2.3 into Equation 2.4, gives an equation for the base shear coefficient as shown in Equation 2.5,

$$\left(\frac{V_y}{W}\right)^2 + \frac{8\pi^2}{T^2 g}\left(\sum_{i=1}^{n}\lambda_i h_i\right)\theta_p\left(\frac{V_y}{W}\right) - \gamma S_a{}^2 = 0 \qquad \textbf{Equation 2.5}$$

Let $\alpha_0 = \frac{8\pi^2}{T^2 g}\left(\sum_{i=1}^{n}\lambda_i h_i\right)\theta_p$, an admissible solution for the $\frac{V_y}{W}$ can be written as Equation 2.6

$$\frac{V_y}{W} = \frac{-\alpha_0 + \sqrt{\alpha_0{}^2 + 4\gamma S_a^2}}{2} \qquad \textbf{Equation 2.6}$$

To ensure the MDOF system had evenly distributed plastic demand along the height of the structure, Chao et al. (2007) proposed that the structure be designed based on the distribution of story shears given by

$$\beta_i = \frac{V_i}{V_n} = \left(\frac{\sum_{j=i}^{n} w_j h_j}{w_n h_n}\right)^{0.75T^{-0.2}} \qquad \textbf{Equation 2.7}$$

Equation 2.7 represents the normalized story shear distribution with respect to the story shear in the top story, V_n. The equation was obtained from a series of nonlinear dynamic analyses of steel moment frames with a variation of story heights.

Using the given normalized story shear distribution, the distribution of the lateral forces on each level can be obtained as

$$F_i = \lambda_i V_y \qquad \textbf{Equation 2.8}$$

where

$$\lambda_i = (\beta_i - \beta_{i+1}) \left(\frac{w_n h_n}{\sum_{j=1}^{n} w_j h_j} \right)^{0.75T^{-0.2}} \qquad \textbf{Equation 2.9}$$

where w_n and w_j are the seismic weights at the roof (level n) and the level j, respectively; h_n and h_j are the heights from the ground to the roof (level n) and level j, respectively.

In this way, the design base shear for a specified hazard level, V_y was calculated accordingly. This base shear could be distributed along the building height as lateral design force (Chao et al., 2007). Plastic design and capacity design were then performed to detail the designated yielding and non-yielding elements, respectively. Since the PBPD procedure considered target drift and strength design within the calculation, no iteration was needed to redesign members and recheck building drift, which was convenient for designers for daily practice.

2.3 PBPD Application on BRKBTMF System

BRKBTMF is a novel structural system and no prior design procedure has been proposed. Therefore, the PBPD method was used to design this structure. Detailed design was first proposed by Wongpakdee (2011) and further developed by Yang et al. (2013) based on PBEE evaluation framework. BRKBTMF utilized the structural fuses to dissipate earthquake energy and truss to span long distant. By selecting the BRBs as the structural fuses, the damage location could be controlled and BRBs could be replaced easily after an earthquake.

2.3.1 Drift Selection and Base Shear Calculation

The first step in using the PBPD procedure was to select the yield (Δ_y) and target drifts (Δ_t) (Figure 2.1). The yield drift, for most structural systems, was usually the inherent characteristic of the system, which could be obtained from the pushover analysis. The yield drift for steel moment frames and concentrically braced frames were typically around 1% and 0.3%, respectively (Goel & Chao, 2008). A yield drift of 0.75% was selected to design the BRKBTMF, which was obtained from the pushover analysis conducted by Wongpakdee et al. (2011 & 2014). The designer could select different target drift to achieve different performance objectives. The structural period can be estimated according to the experience formula permitted by ASCE (2010). Depending on the period and ductility of BRKBTMF, the energy reduction factor could be obtain through Figure 2.2. Then following Equation 2.6, the design base shear of BRKBTMF could be calculated.

2.3.2 Yielding Member Design

Since the BRBs were the designated energy dissipation devices, these elements would be designed first. Using the plastic mechanism analysis as shown in Figure 2.3, the plastic energy to be dissipated by the BRBs shall equal to the plastic energy calculated in Equation 2.4. Equation 2.10 shows the energy balanced equation between building plastic energy and BRB energy consumption. Note that the column bases were selected as pin bases to avoid damage to the column bases. Hence it was not included in the total plastic energy equation.

After the sizes of the BRBs were determined, the trusses and columns were then capacity designed to remain elastic, hence it was expected that the trusses and columns would be undamaged after the earthquake.

$$E_p = V_y\left(\sum_{i=1}^{n}\lambda_i h_i\right)\theta_p = \sum_{i=1}^{n}2\left(\beta_i N_{BRB}\right)\delta_p \qquad \textbf{Equation 2.10}$$

where N_{BRB} is the axial strength of the BRBs at the top story (level n), and δ_p is the plastic axial deformation of the BRBs (as shown in Equation 2.11).

$$\delta_p = (D_0 \sin\alpha + l_1 \cos\alpha)\theta_p \qquad \textbf{Equation 2.11}$$

where, D_0 is the depth of truss; α is the vertical inclination of the BRB (vertical angle between the BRB and the column); and l_1 is the length of first top chord.

Figure 2.4 shows the deformed and undeformed configuration of the BRKBTMF subassembly used to derive Equation 2.11. In Figure 2.4, φ is the angle between the column and first diagonal truss member; l_d is the length of the first diagonal truss member l_0 is the undeformed length of the BRB; and θ_t and δ are the total inter-story drift ratio and total BRB deformation (including both the elastic and plastic parts), in which only the plastic part is used in Equation 2.11 to represent plastic energy dissipation.

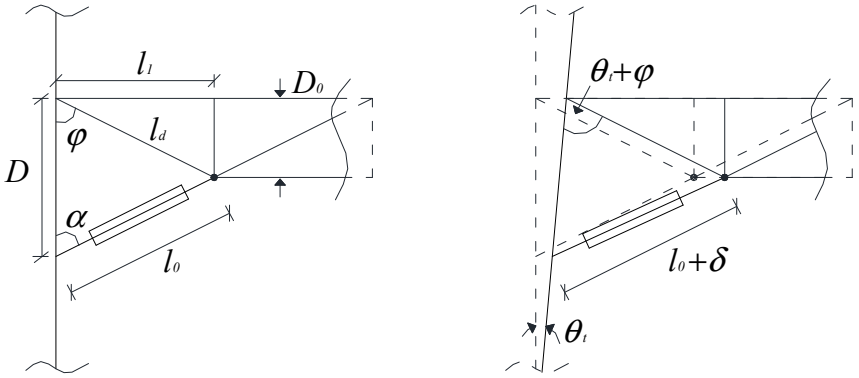

(a) Undeformed geometry (b) Deformed geometry

Figure 2.4 BRKBTMF subassembly

2.3.3 Selection of BRB Inclination

Equation 2.12 and Figure 2.5 show the approximate axial strain in the BRBs as a function of α at different inter-story drift ratio.

$$\varepsilon = \frac{(D_0 \sin^2 \alpha + l_1 \cos\alpha \sin\alpha)\theta_t}{l_1} \qquad \textbf{Equation 2.12}$$

The results showed that, with the geometry presented in this study (D_0 = 2.5 ft. and l_1 = 5 ft.), the BRB had the highest strain when α = 60˚. The axial strain reduced as the BRB inclination deviated away from 60˚. This information was useful in the design. For example, if the BRB had a maximum strain capacity of 2%, which representd the maximum expected inter-story drift ratio of 3% for the building, the engineers should select a BRB inclination angle, α to be less than 37 ˚ or greater than 79 ˚. On the other hand, if the BRB's inclination were selected by the architect (for example, α = 60˚) and the target inter-story drift ratio of 3%, the engineer should select a BRB with fracture strain greater than 2.4%. Similarly, if the inclination of the BRB and the maximum BRB strain capacity were pre-selected, the engineers could also use this information to select the target drift for the design. It should be noted that the BRB used in the BRKBTMF was usually

shorter than the BRBs used in the conventional concentrically braced configuration. This meant the strain demand for these BRBs would be higher than the conventional concentrically braced BRB frame. Based on the research published by López & Sabelli (2004), BRB usually had a fracture strain reaches between 1.6% and 3%.

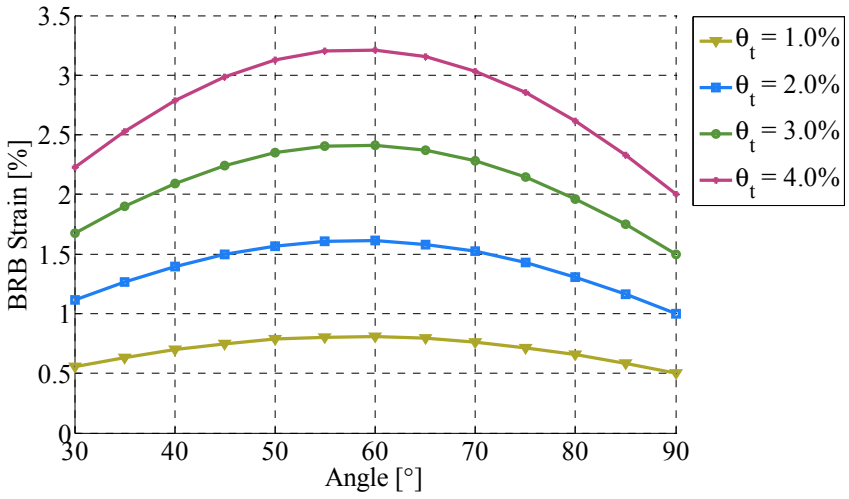

Figure 2.5 BRB strain as a function of α at different inter-story drift ratio

2.3.4 Selection of Truss Span

In design practice, the gravity truss was usually designed with factored load (Equation 2.13(a)), then checked for defection under the service load (Equation 2.13(b)). A deflection limit was usually set as 1/240 of the truss span. The optimal design of truss span and depth existed when strength and deflection demand to capacity ratio both reached 1 at the same time. Truss girder optimization study started from gravity truss. The dimension of the interested truss is shown in Figure 2.6(a). The free body diagram (FBD) for gravity truss is shown in Figure 2.6(b). In order to eliminate the number of variables in the study, the live load (L) in Equation 2.13(a) and (b) was normalized in the format of dead load (D) by live - dead load ratio, $\alpha = L / D$, which would yield Equation 2.14(a) and (b). Since the truss remained elastic under gravity load, and therefore, virtual

method was used to calculate the deflection. The optimal combination of truss span and depth were found according to Figure 2.7 which was based on $\alpha = 1$ and D = 1.4 k/ft. For demonstration, the dash lines were the deflections for the trusses based on strength design, namely strength demand to capacity ratio was 1, and the solid line was the deflection limit of deflection. The crossing points of them gave the truss dimension that both strength and deflection ratio were equal to 1, where these points could be considered as an optimal point for the truss depth at that particular span. These optimal points were recorded to find the trend between span and truss depth variation. Trend lines shown in Figure 2.8 were then generated to capture the depth variation as the truss span was changing for different live to dead load ratios, α, and the general formula is presented in Equation 2.15(a) and simplified into Equation 2.15(b) for practical purposes and the unit is in feet. Note that the common spans for buildings ranged from 20 ft. to 100 ft., and the live to dead load ratios ranged from 0 to 3.

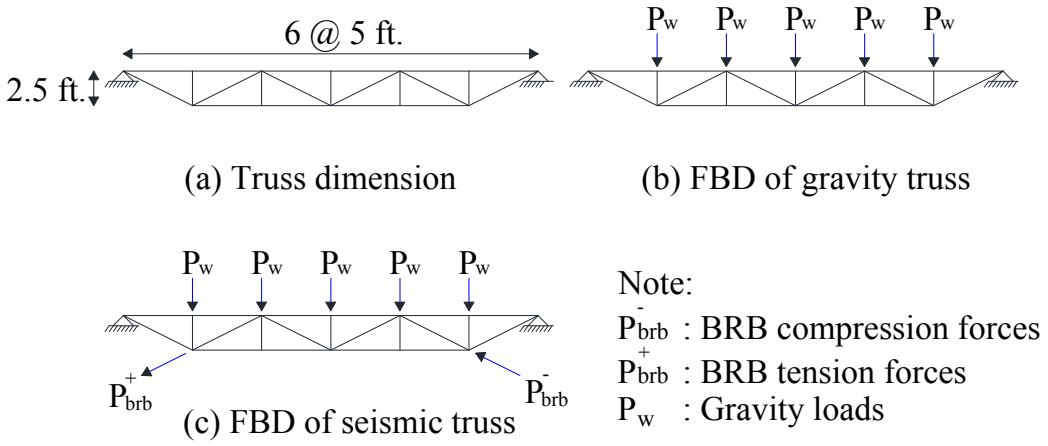

Figure 2.6 Truss loading conditions

$1.2D + 1.6L$ (a) and $D + L$ (b) **Equation 2.13**

$(1.2 + 1.6\alpha)D$ (a) and $(1 + \alpha)D$ (b) **Equation 2.14**

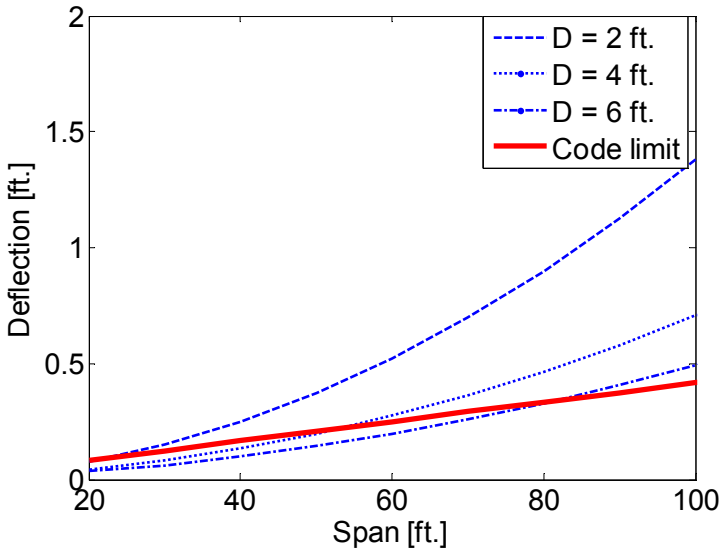

Figure 2.7 Deflection plot based on strength design

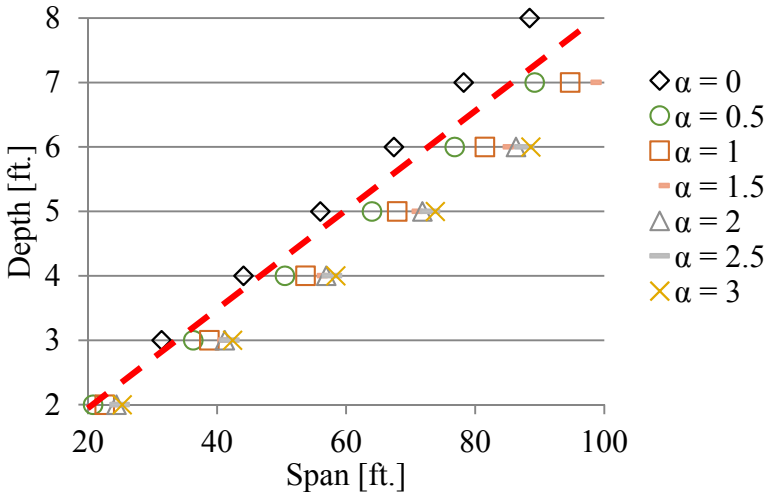

Figure 2.8 Trend line of optimal depth span relationship

$$Depth = \left(\frac{\alpha^2}{264} - \frac{\alpha}{58} + \frac{1}{12}\right)Span + \left(\frac{\alpha^2}{77} - \frac{\alpha}{14} + \frac{1}{3}\right) \quad \text{(a)}$$

$$Depth = \frac{1}{12}Span + \frac{1}{3} \quad \text{(b)}$$

Equation 2.15

Seismic truss design was different from the gravity truss design, although seismic truss was also first designed based on strength, it was not controlled by deflection under gravity loads

because the BRB forces amplified the truss sizes so that the deflection for seismic truss under gravity would be much less than code limit. The study was carried out by varying the truss depth in order to find out the least steel usage. The dimension was the same as gravity truss as shown in Figure 2.6(a) and the FBD of truss under forces from BRBs is shown in Figure 2.6(c). In the particular study here, the 30 ft. span truss was subjected to an average of 360 kips in tension and 420 kips in compression of BRB forces, while the 60 ft. span truss was also subjected to an average of 550 kips in tension and 640 kips in compression of BRB forces. By varying the truss depth, the steel usage was plotted in volume in Figure 2.9. The plot shows that the 30 ft. and 60 ft. seismic truss have optimal truss depth of around 10 ft. and 13 ft. However, these were not practical values for buildings. Since the typical truss depths for buildings range from 1 to 6 ft. and the steel usage was monotonically decreasing within this range, and therefore, the depths of seismic truss could be consistent with the gravity truss in order to keep the same clear height.

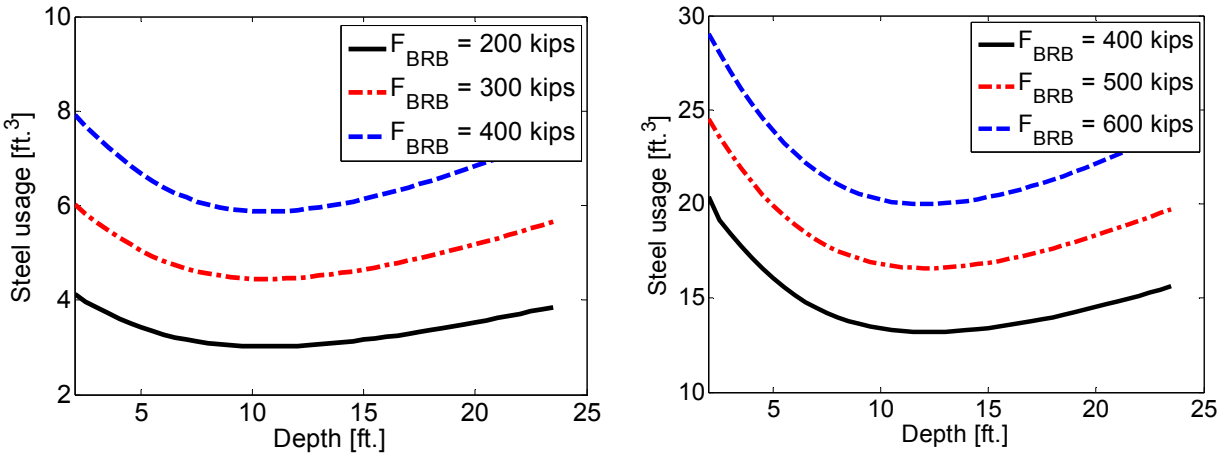

(a) 30 ft. seismic truss (b) 60 ft. seismic truss

Figure 2.9 Steel usage truss with various truss depth and span

2.3.5 Capacity Design

2.3.5.1 Truss Design

The size of BRB could be determined following Equation 2.10, the truss could be designed to remain elastic under the gravity and the largest forces generated by the BRBs. The design FBD of truss under both gravity load and BRB force is shown in Figure 2.6(c). AISC 341 (AISC, 2010a) permitted to use the following two formulas to calculate the maximum BRB forces:

for tension

$$P^{+}_{BRB,\max} = \omega R_y P_y \qquad \text{(a)}$$

for compression

$$P^{-}_{BRB,\max} = \omega \beta R_y P_y \qquad \text{(b)}$$

Equation 2.16

These formulas include the strength hardening adjustment factor, ω, which is the ratio of maximum tension force ($P^{+}_{BRB,\max}$) divided by the expected yield strength ($R_y P_y$); R_y is the material expected strength factor. The equation also includes the compression strength adjustment factor, β , which is defined as the ratio of the maximum compression force ($P^{-}_{\max}$) divided by the maximum tension force ($P^{+}_{BRB,\max}$). Figure 2.10 shows the graphical representation of the above parameters.

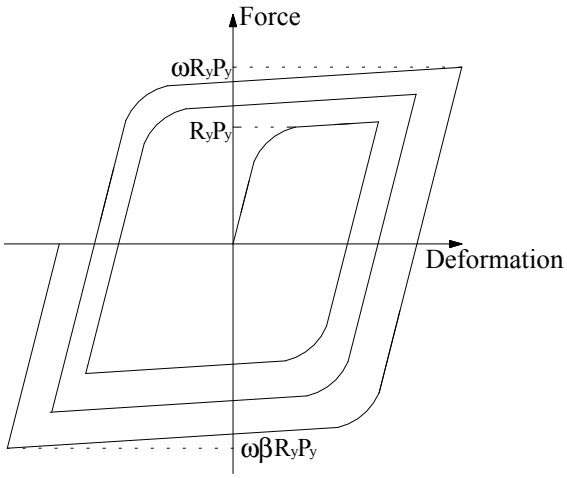

Figure 2.10 Typical BRB parameters

2.3.5.2 Column Design

Exterior Column

The columns in BRKBTMF systems were designed to remain elastic up to the target drift ratio. Therefore, when the frame reacheed its target drift, the maximum tension or compression in BRBs were assumed to reach the maximum expected strengths as described in Equation 2.16. The maximum internal forces in the truss due to both gravity and BRB forces as shown in Figure 2.6(c) were also applied to columns. At this stage, the required lateral forces acting on the columns to the right and left on i^{th} floor, $F_{ext.R,i}$ and $F_{ext.L,i}$ were assumed to maintain the distribution as Equation 2.9 and could be easily calculated by using moment equilibrium of the base of column tree. These lateral forces were used to balance the column tree and they could be determined from Figure 2.11 and could be expressed by

$$F_{ext.R,i} = \alpha_i \frac{\sum_{i=1}^{n}(T_{R,i} - D_{R,i}\sin\varphi)h_i - \sum_{i=1}^{n}(P^{+}_{BRB,i}\sin\varphi)(h_i - D)}{\sum_{i=1}^{n}\alpha_i h_i} \qquad \text{(a)} \qquad \textbf{Equation 2.17}$$

$$F_{ext.L,i} = \alpha_i \frac{\sum_{i=1}^{n}(T_{L,i} - D_{L,i}\sin\varphi)h_i - \sum_{i=1}^{n}(P^{+}_{BRB,i}\sin\varphi)(h_i - D)}{\sum_{i=1}^{n}\alpha_i h_i} \qquad \text{(b)}$$

where $T_{R,i}$ and $T_{L,i}$ are the axial forces in the top chord at any floor level *i*, $D_{R,i}$ and $D_{L,i}$ are axial forces in the diagonal member at any level *i*, $P^{+}_{BRB,i}$ and $P^{-}_{BRB,i}$ are maximum BRB tension and compression forces at any level *i*, Floor *n* is the top floor, h_i is the height from column base, φ is the angle between a diagonal member and a column, and α_i is the distribution factor given by:

$$\alpha_i = \frac{(\beta_i - \beta_{i+1})}{\sum_{i=1}^{n}(\beta_i - \beta_{i+1})} \qquad \textbf{Equation 2.18}$$

when $i = n$, $\beta_{n+1} = 0$

Figure 2.11 shows the free body diagram of the column tree, in general, the columns needed to remain elastic under the loads transferred from BRB, truss, lateral forces and concentrated loads, $P_{c,i}$ from the orthogonal gravity system at any level *i*.

Interior Column

The interior column is only the summation of the left and right exterior forces as shown below.

$$F_{int,i} = F_{ext.R,i} + F_{ext.L,i} \qquad \textbf{Equation 2.19}$$

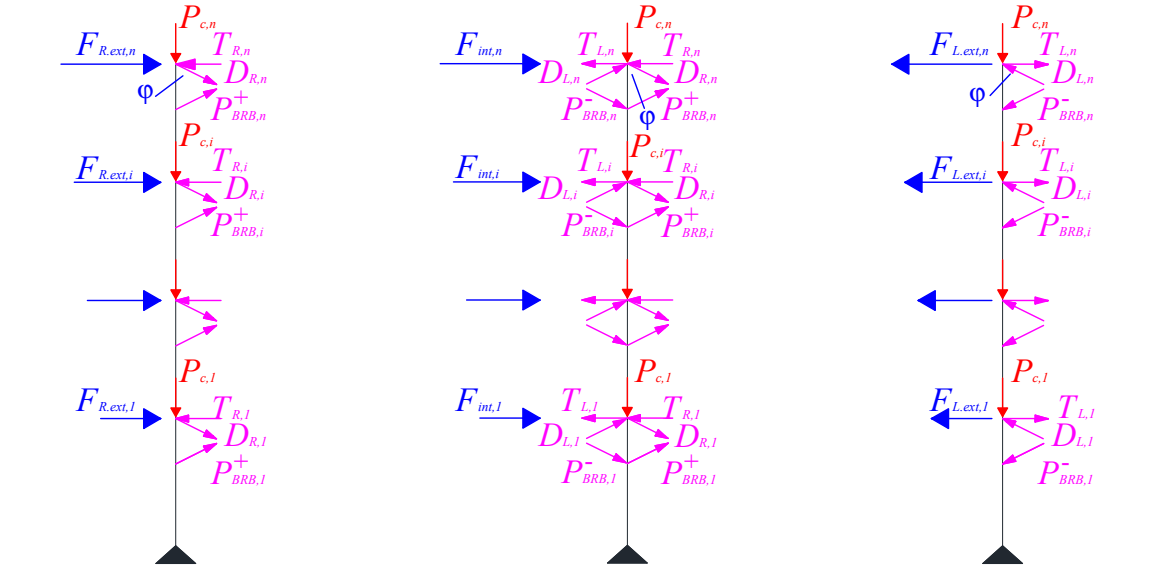

(a) Exterior column (lateral force to the right)

(b) Interior column

(c) Exterior column (lateral force to the left)

Figure 2.11 Free body diagram of column tree

Chapter 3 Analytical Modeling

This chapter introduced the analytical modeling method used in this thesis. Some experiment tests of BRB were introduced and calibrated with numerical models and the BRB cyclic behavior was explained. This chapter also described the logistics to modify Steel02 material in OpenSees to model BRB more accurately. Advanced element removal technique was also developed to simulate the BRB factures and force redistribution in the building. The finite element modeling of the prototype building was also described.

3.1 Experiment Tests of BRB

Buckling restrained braces (BRBs) were studied extensively by researchers around the world. The first research started at Japan by Yoshino at 1971 (Yoshino & Karino, 1971). Researchers from North America studied the behavior of BRBs about a decade ago. The first BRB research in North America was triggered by the design and construction of the first building that utilized BRBs in United States. Clark et al. (1999) conducted three large-scale unbonded brace tests at University of California, Berkeley. The first two specimens had a rectangular yielding cross section and the third specimen had a cruciform cross section. Clark et al. (1999) used the SAC loading protocols, a simulated earthquake displacement record and constant–amplitude low-cycle fatigue tests to examine the force-deformation response of the BRBs. The tests showed that the BRBs had stable force-deformation hysteresis. Merritt et al. (2003) tested a large arrays of subassemblage tests for BRB products from Star Seismic and CoreBrace and reported the relationship between the tensile strength adjustment factor and the brace axial deformation from

these tests. Black et al. (2004) conducted several numerical simulations and experiments to study the stability against global buckling of BRB, buckling of the inner core and plastic torsional buckling of the inner core. Tremblay et al. (2006) tested two types of BRBs, one with long core steel plates and the other one with short core steel plates. The experimental tests showed the BRBs with short steel core had much larger ductility demands than the one with long steel core. Some key experimental tests are summarized in Table 3.1.

Table 3.1 Summary of BRB tests

Year	Reference	Type	No. of tests	Brace sizes range [kip]	Brace length range [ft.]	Max. brace strain (MBS) range [%]	Mean of MBS [%]
1999	Clark et al. (1999)	Component	6	270 - 470	14.75	1.80 - 4.10	2.30
2003	Merritt et. al (2003a)	Subassemblage	6	338 - 897	18.00	2.40 - 2.68	2.50
2003	Merritt et al. (2003b)	Subassemblage	8	160 - 1200	21.00	1.77 - 2.64	2.25
2004	Black et al. (2004)	Component	1	454	10.96	1.75	1.75
2006	Iwata & Murai (2006)	Component	13	108 - 460	7.70	1.60 - 3.00	2.66
2006	Tremblay et al. (2006)	Subassemblage	7	132	14.09	2.70 - 4.8	3.75

3.2 Behaviors of BRB

The outer casing of BRB could prevent the core from buckling in compression. Figure 3.1 shows the BRB characteristics under cyclic loading. The symbols used in Figure 3.1 were defined in Chapter 2 . Because the BRB was restricted from buckling by the outer casing, it could achieve comparable compression strength as the tension strength while the buckling brace had significant compression strength loss as shown in Figure 3.1. Kinematic and isotropic hardening was also observed in typical BRBs.

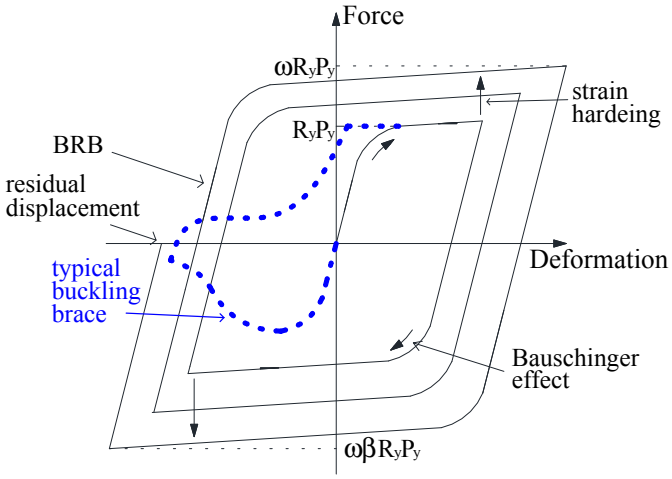

Figure 3.1 BRB hysteresis characteristics

3.3 Numerical Modeling of BRB

The BRB material was modeled using Giuffre-Menegotto-Pinto Model with Filippou isotropic strain hardening (Filippou et al., 1983). This model was presented in an explicit algebraic equation for stress in the function of strain. Due to its simplicity and accuracy, it was one of the most popular models people were using for isotropic material. The model could accurately simulate the Bauschinger effect, which was common for most steel material. The model follows the below formulation.

$$\sigma^* = b\varepsilon^* + \frac{(1-b)\varepsilon^*}{(1+\left|\varepsilon^*\right|^R)^{\frac{1}{R}}}$$ **Equation 3.1**

where

$$\varepsilon^* = \frac{\varepsilon - \varepsilon_r}{\varepsilon_0 - \varepsilon_r}$$ **Equation 3.2**

and

$$\sigma^* = \frac{\sigma - \sigma_r}{\sigma_0 - \sigma_r}$$ **Equation 3.3**

Equation 3.4 represents a curved transition shown in Figure 3.2 from a straight line asymptote with slope E_0, elastic modulus to another asymptote with slope E_{sh}, post yielding modulus. σ_0 and ε_0 are stress and strain at the point where the two asymptotes of the branch under consideration meet; similarly, σ_r and ε_r are stress and strain at the point where the last strain reversal with stress of equal sign took place; b is the strain hardening ratio, that is the ratio between slope E_0 and E_{sh}. R is a parameter which affects the shape of the transition curve and allows a good representation of the Bauschinger effect. And it is considered to be dependent on the strain difference between the current asymptote intersection point (point A) and the previous load reversal point (point B). Parameter R can be calculated as following.

$$R = R_0\left(1 - \frac{cR_1\xi}{cR_2 + \xi}\right) \qquad \textbf{Equation 3.4}$$

where

$$\xi = \frac{\varepsilon - \varepsilon_0}{\varepsilon_y} \qquad \textbf{Equation 3.5}$$

where ξ is updated for each strain reversal. R_0 is the value of the parameter R during first loading. cR_1 and cR_2 are experimentally determined parameters to be defined together with R_0. The definition of ξ remains valid in case that reloading occurs after partial unloading.

The mathematical model (from Equation 3.1 to Equation 3.5) was originally formulated by Giuffre and Pinto (1970), Filippou et al. (1983) improved the model to account for isotropic strain hardening by shifting the position of the yield asymptote before computing the new asymptote intersection point following a strain reversal. The shift was affected by moving the initial yield asymptote through a stress shift σ_{st} parallel to its direction as shown in Figure 3.3. However, the

asymptote shift was modified in this thesis so that the stress needed to travel to the opposite side before the shift was activated. This modification was more realistic than assuming that any strain reversal could trigger the shift and it was useful when the force redistribution occurred after element removal. The relation for stress shift takes the form.

$$\frac{\sigma_{st}}{\sigma_y} = 1 + a_1\left(\frac{\varepsilon_{\max} - \varepsilon_{\min}}{2a_2\varepsilon_y}\right) \qquad \textbf{Equation 3.6}$$

where ε_{max} and $\varepsilon_{\min}$ is the maximum and minimum strain at the instant of strain reversal, ε_y, σ_y are, respectively, strain and stress at yielding, and a_1 and a_2 are the isotropic strain hardening parameters which can be determined experimentally. The model can have different isotropic strain hardening for the tension and compression sides, which means Equation 3.6 can have different values of a_1 and a_2 for both the tension and compression sides. To be further improved, the material model should have different values of post-yielding stiffness, as well as different transition from the elastic to inelastic range to better match the BRB material. With similar logistics, Equation 3.4 and Equation 3.5 can have different values for b , cR_1 and cR_2 of compression and tension behaviors. Figure 3.4 shows the behavior of modified Steel02 model. This material model allowed different strain hardening, post-yielding stiffness, and Bauschinger effect for compression and tension. This modified material model had a better match than original material model. The calibration for BRB against different test data using modified material is shown in Figure 3.5 and the modeling parameter is tabulated in Table 3.2.

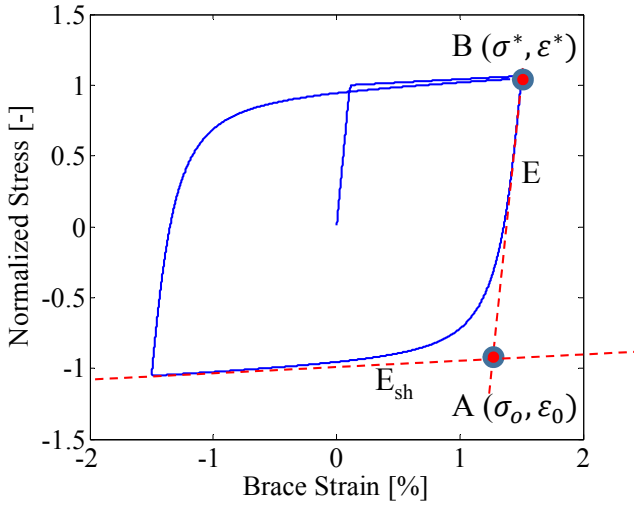

Figure 3.2 Illustration of curved transition

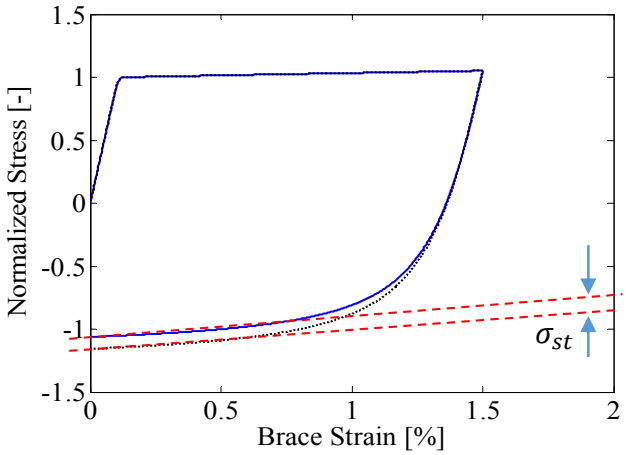

Figure 3.3 Illustration for σ_{st}

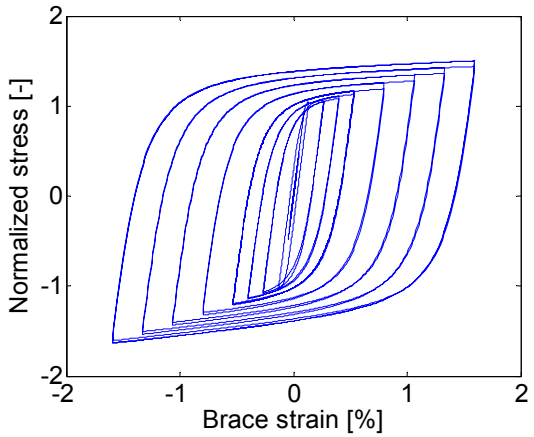

Figure 3.4 Numerical hysteresis of BRB using modified Steel02 material

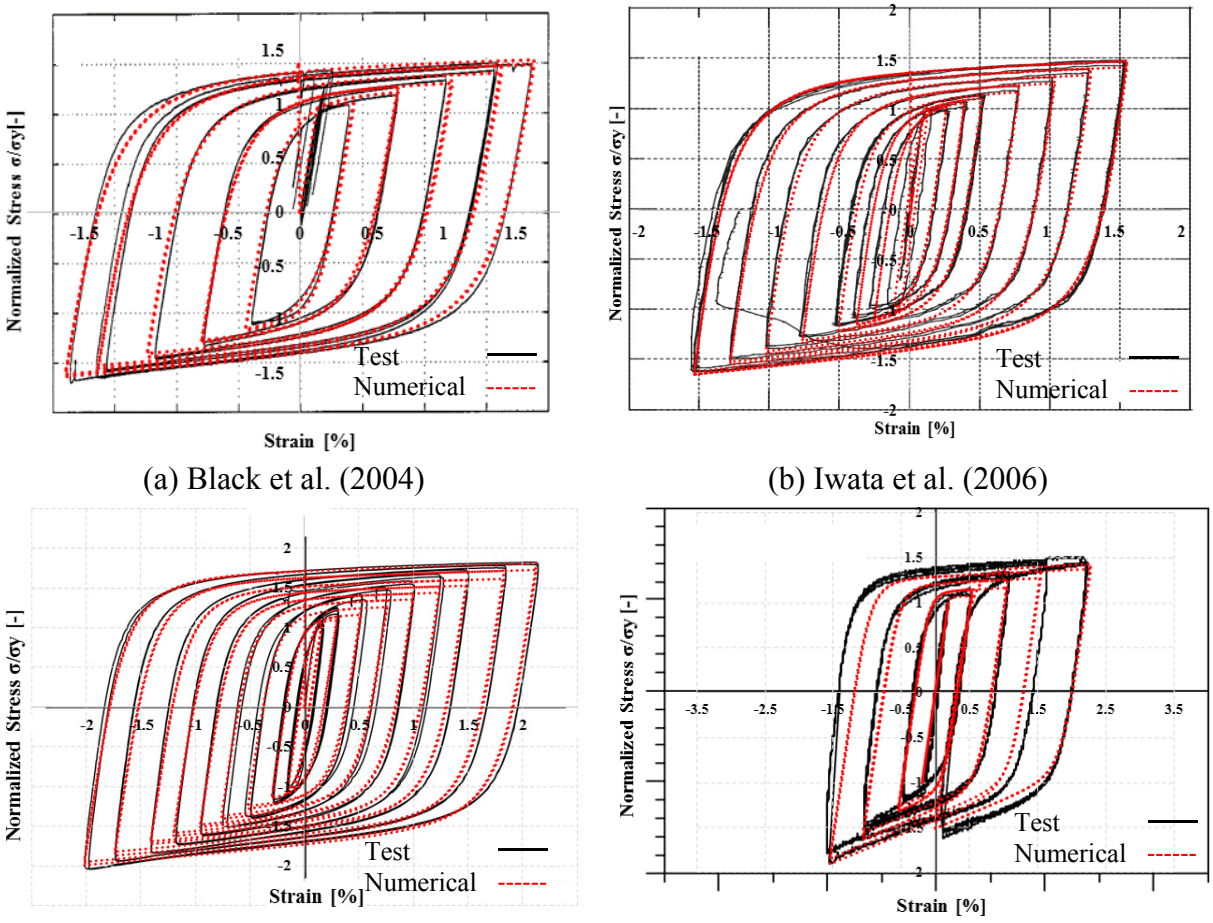

(a) Black et al. (2004)

(b) Iwata et al. (2006)

(c) Merritt et al. (2003)

(d) Tremblay et al. (2006)

Figure 3.5 BRB calibration against reference tests

3.4 Moment Hinge Modeling

On the other hand, the beams of the MF used in Chapter 8 were modeled using elastic beam with lump hinges at the ends. Hysteretic material with degradation in OpenSees was used to model the nonlinear rotational response of the beam hinges. Figure 3.6 shows the moment-rotation response of the beam hinges calibrated using the SAC test data (SAC, 2011). The beam hinges were assumed to have a plastic fracture rotation capacity of 4% and the residual strength was assumed to be 0.4 times the yield strength of the section. This parameter selection was consistent with the modeling approach proposed by Lignos et al. (2013).

Table 3.2 BRB modeling parameters in OpenSees

Reference		Black et al. (2004)	Iwata et al. (2006)	Merritt et al. (2003)	Tremblay et al. (2006)
Material Parameters	*E* (ksi)	33431	40915	34901	27844
	fy (ksi)	41.4	331.8	37.5	53.7
	bt	0.004	0.004	0.004	0.008
	bc	0.0127	0.0127	0.0127	0.06
	R0t	32	23	32	60
	R0c	28	23	28	60
	cR1	0.925	0.925	0.925	0.925
	cR2	0.15	0.15	0.15	0.15
	a1	0.05	0.05	0.073	0.014
	a2	1	1	1	1
	a3	0.05	0.05	0.07	0.055
	a4	1	1	1	1
Element Parameters	*A* (in^2)	11	3.5	27	2.46
	L (in)	177.2	92.6	250.2	169

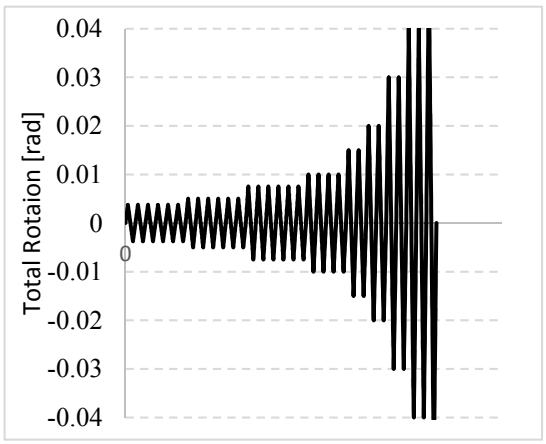

(a) Beam connection loading protocol

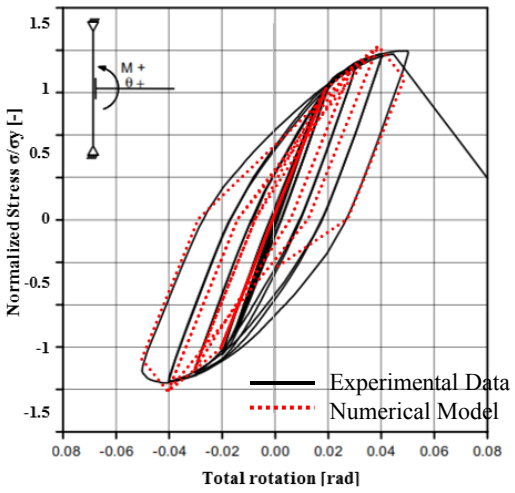

(b) Moment-rotation response

Figure 3.6 Moment hinge calibration against reference test

3.5 Element Removal Modeling Technique

When the axial strain exceeded the strain limit of BRB, the BRB was expected to fracture. This would result to a sudden loss of force in the BRB. To properly model such behavior, a robust modeling technique was implemented in OpenSees. Figure 3.7 shows the general procedure of the element removal technique. The BRB was assumed to have an axial strain capacity with normal distribution with mean of 2.5% and a dispersion of 0.4. At the beginning of the analysis, a strain capacity was selected. Note each BRB element would have a different strain capacity. At each stage of the analysis, the BRB strain was compared with the strain capacity. If the BRB strain was less than the capacity, element removal would not be triggered and the analysis would be carried on as usual. Once BRB strain exceeded the limit, the element removal would be activated and those BRB elements would be removed. Similarly, the associated nodes and recorders would be also removed to avoid software errors. The stiffness matrix would be updated before the next analysis. This modeling technique allowed the model to accurately simulate the force re-distribution, hence captured the progressive collapse sequence of the structure.

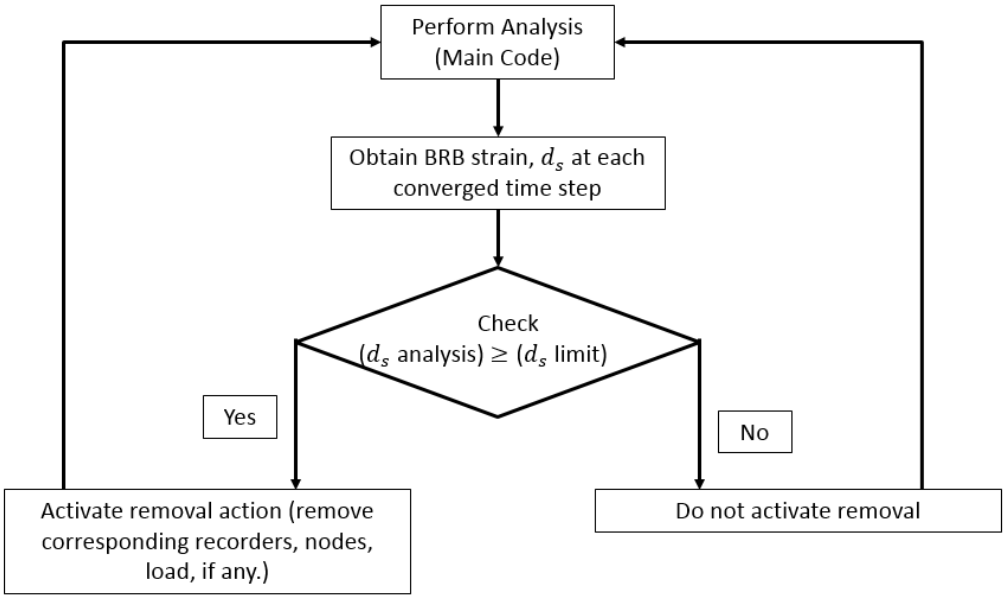

Figure 3.7 Element removal procedure

3.6 Modeling of Building

Two-dimensional finite element models of the prototype building were developed using OpenSees. The columns were modeled using the fiber force-based beam-column element with steel01 material. The base of the columns was modeled as pin. The top and bottom chords of the truss were continuous beams, and were modeled using force-based beam column elements. The elements were pin connected to the column face. The diagonal and vertical chords were modelled as elastic truss elements. The BRBs were modeled using the calibrated nonlinear truss element in OpenSees with the modified Steel02 material shown in Section 3.3. The element removal algorithm was implemented. The P-Δ effect was modeled using the P-Δ transformation. Mass was assigned as lump masses in the nodes based on the tributary area. Rigid diaphragm was assigned at each floor. 2% Rayleigh stiffness and mass proportional damping was assigned in the first and third mode. Figure 3.8 shows the overall view of the building modeling.

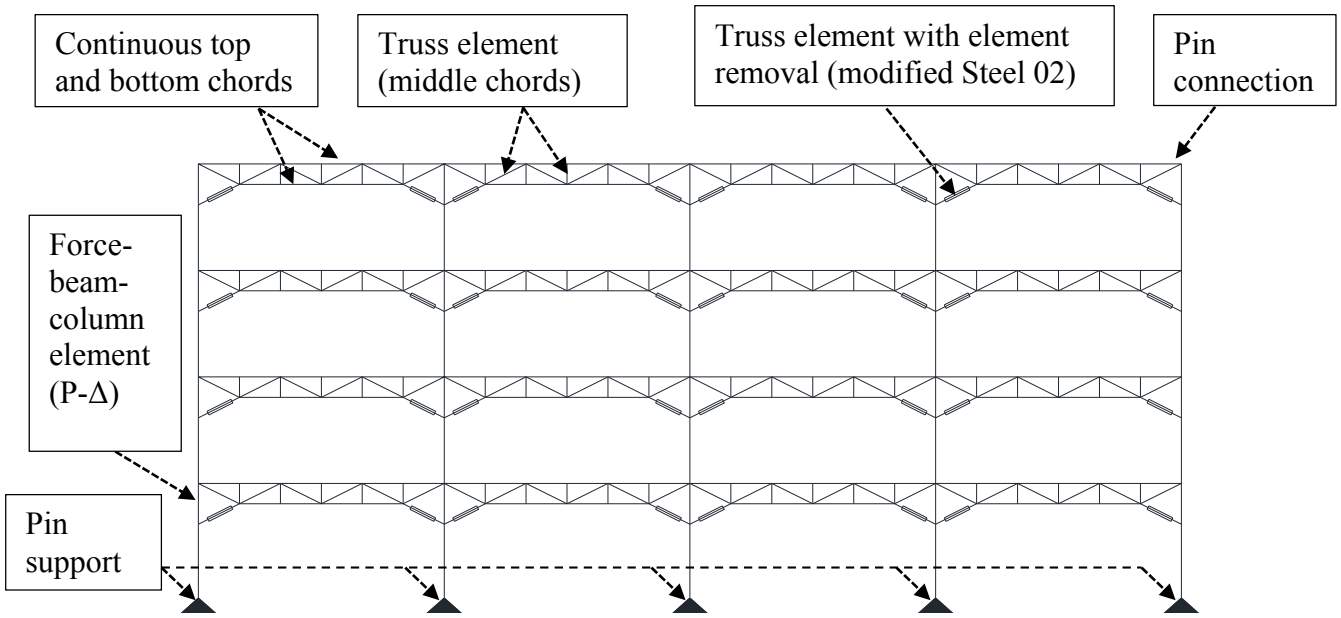

Figure 3.8 Building modeling

Chapter 4 Prototype Building

A prototype office building located in Berkeley, California was designed to confirm the applicability of the BRKBTMF. This chapter summarized the prototype building used in this study, including the seismic hazards, member sizes and some preliminary assessment through nonlinear dynamic time history analysis.

4.1 Seismicity of Building Site

Berkeley, California is located in the "Pacific ring of fire", which is a belt of seismically active zones surrounding the Pacific Ocean. Figure 4.1 shows the location of the prototype building on the "Pacific ring of fire". The site is dominated by potential ground motions generated from the Hayward fault, which is a strike-slip fault that has a potential to generate M_w 7 earthquakes (UCB, 2003). The soil condition on the site can be classified as C according to ASCE (2010).

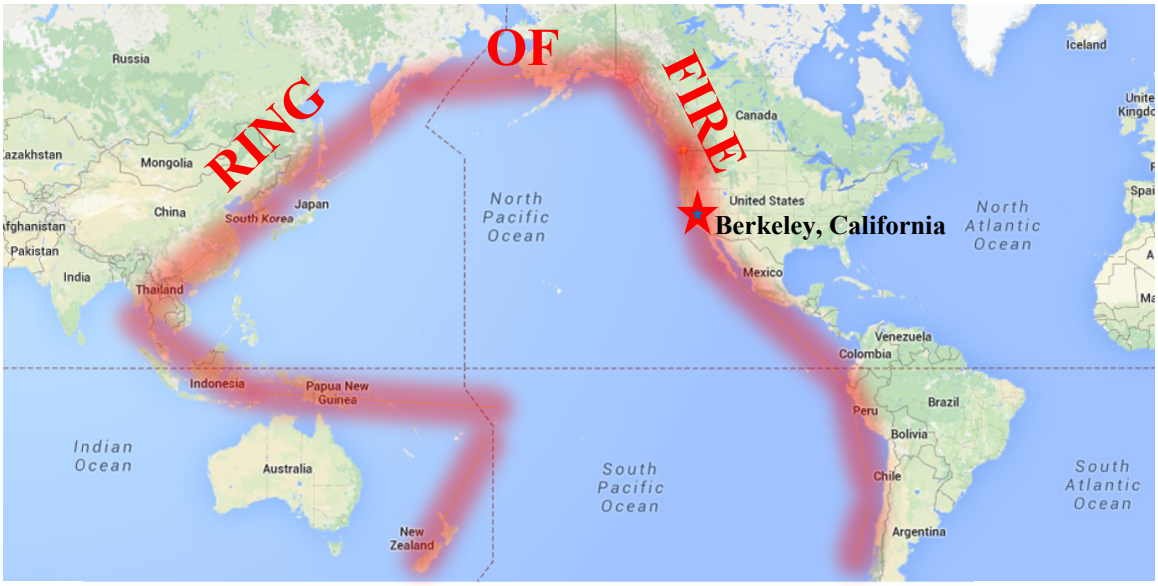

Figure 4.1 Geographical location of "Pacific ring of fire"

4.2 Ground Motion Selection

Ground motions were selected from the PEER NGA database (PEER, 2010). Three hazard levels were included in this study: 1) 2% Probability of Exceedance (POE) in 50 years (2/50); 2) 10% POE in 50 years (10/50), and 3) 50% POE in 50 years (50/50) hazard levels. Based on the deaggragation results (UCB, 2003), the ground motions were selected from earthquakes with magnitude between M_w = 6.5 and M_w = 7.5, closest distance to the fault within 10 miles and soil shear wave velocity at 98.4 ft. (30 meters) below grade (Vs30) between 1200 ft./s to 2500 ft./s. The ground motions were then amplitude scaled using the procedure outlined in ASCE 7 Section 16.1.3.1 (ASCE, 2010), where that the mean spectrum of the set (20 ground motions) did not fall below the target spectrum by 10% within the period range from 0.2T (0.2 sec) to 1.5T (1.5 sec) (T = 1.0 sec which was the fundamental period of the building). The shorter period was selected to account for the higher mode responses, while the longer period was selected to allow for the period

elongation due to yielding in the system. Scale factors were limited to between 0.1 and 5 to avoid over scaling. Table 1 shows the summary of the ground motions selected. Figure 4.2 shows the ground motion scaling to the three hazard levels considered.

Table 4.1 Ground motion details

Year	NGA No.	Event	Station	Moment Magnitude	Vs30	Shortest distance to the fault [Miles]	Scaling factor		
				[M_w]	[ft./sec]		2/50	10/50	50/50
1976	125	Friuli, Italy	Tolmezzo	6.50	1394.0	9.8	3.38	1.91	0.69
1976	126	Gazli, USSR	Karakyr	6.80	2164.0	3.4	2.06	1.16	0.42
1978	139	Tabas, Iran	Dayhook	7.35	2492.1	8.6	3.70	2.08	0.75
1984	451	Morgan Hill	Coyote Lake Dam	6.19	2615.4	0.3	1.68	0.95	0.34
1984	459	Morgan Hill	Gilroy Array	6.19	2176.2	6.2	3.33	1.87	0.68
1985	495	Nahanni, Canada	Site 1	6.76	2164.0	6.0	3.01	1.70	0.61
1985	496	Nahanni, Canada	Site 2	6.76	2164.0	3.0	4.54	2.56	0.92
1989	741	Loma Prieta	BRAN	6.93	1233.9	6.6	1.96	1.11	0.40
1989	753	Loma Prieta	Corralitos	6.93	1516.4	2.4	2.21	1.24	0.45
1989	802	Loma Prieta	Saratoga - Aloha Ave	6.93	1516.4	5.3	4.06	2.29	0.83
1992	825	Cape Mendocino	Cape Mendocino	7.01	1685.3	4.3	1.67	0.94	0.34
1992	879	Landers	Lucerne	7.28	2247.0	1.3	4.27	2.40	0.87
1994	1013	Northridge	LA Dam	6.69	2063.6	3.6	3.62	2.04	0.74
1995	1111	Kobe, Japan	Nishi-Akashi	6.90	1998.0	4.4	3.01	1.70	0.61
1994	1004	Northridge	Sepulveda VA Hospital	6.69	1247.1	5.2	1.86	1.05	0.38
1994	989	Northridge	LA Dam	6.69	2063.7	3.7	3.62	2.04	0.74
1999	1182	Chi-Chi, Taiwan	CHY006	7.62	1437.7	6.1	2.63	1.48	0.53
1994	983	Northridge	Jensen Filter Plant	6.5	1725.0	4.3	2.64	1.49	0.54
1999	1512	Chi-Chi, Taiwan	TCU078	7.62	1453.4	5.1	3.45	1.94	0.70
1999	1787	Hector Mine	Hector	7.13	2247.0	7.3	3.31	1.87	0.67

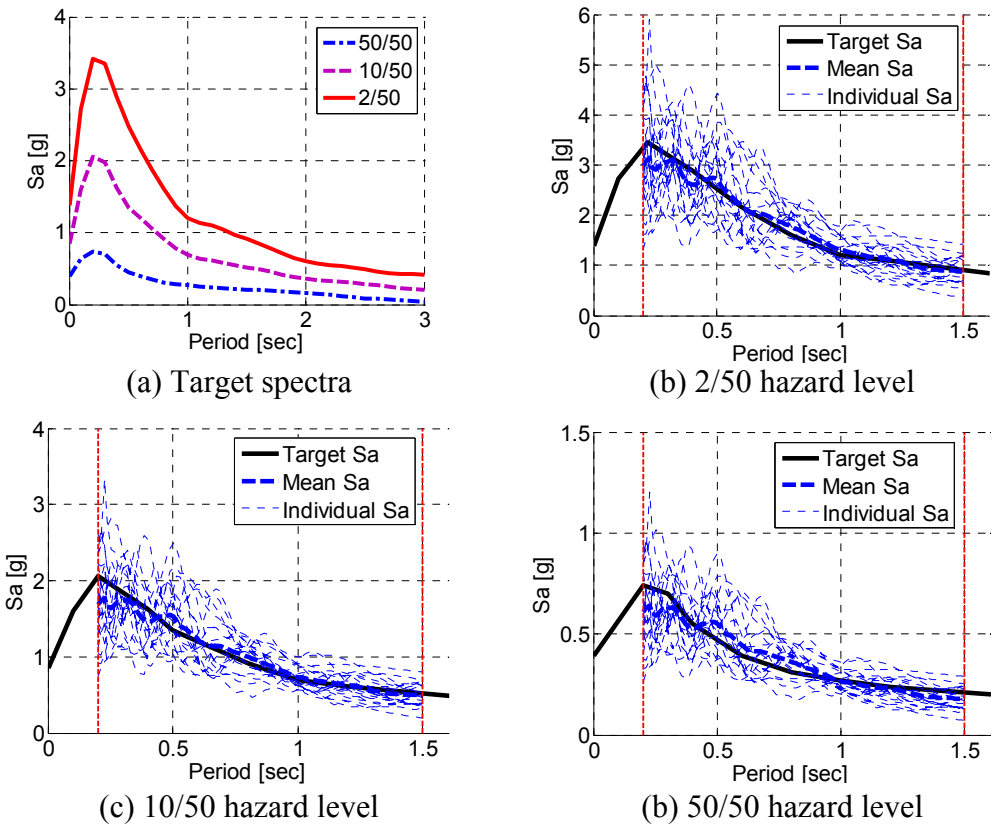

(a) Target spectra (b) 2/50 hazard level

(c) 10/50 hazard level (b) 50/50 hazard level

Figure 4.2 Scaled spectra

4.3 Description of Prototype Building

The archetype structure was a 4-story steel office building without basement. Building dimension were 180 ft. by 120 ft. with an overall height at 53 ft. The story height was 14 ft. for the first story and 13 ft. for the remaining stories. Figure 4.3 shows the plan view and elevation view of the prototype building. For the architectural purpose, the clear heights were kept at 11.5 ft. for the first story, and 10.5 ft. for the remaining stories. The seismic force resisting system (SFRS), in this case the BRKBTMF was located at the perimeters of the building. Each SFRS consisted of 4 bays of frames.

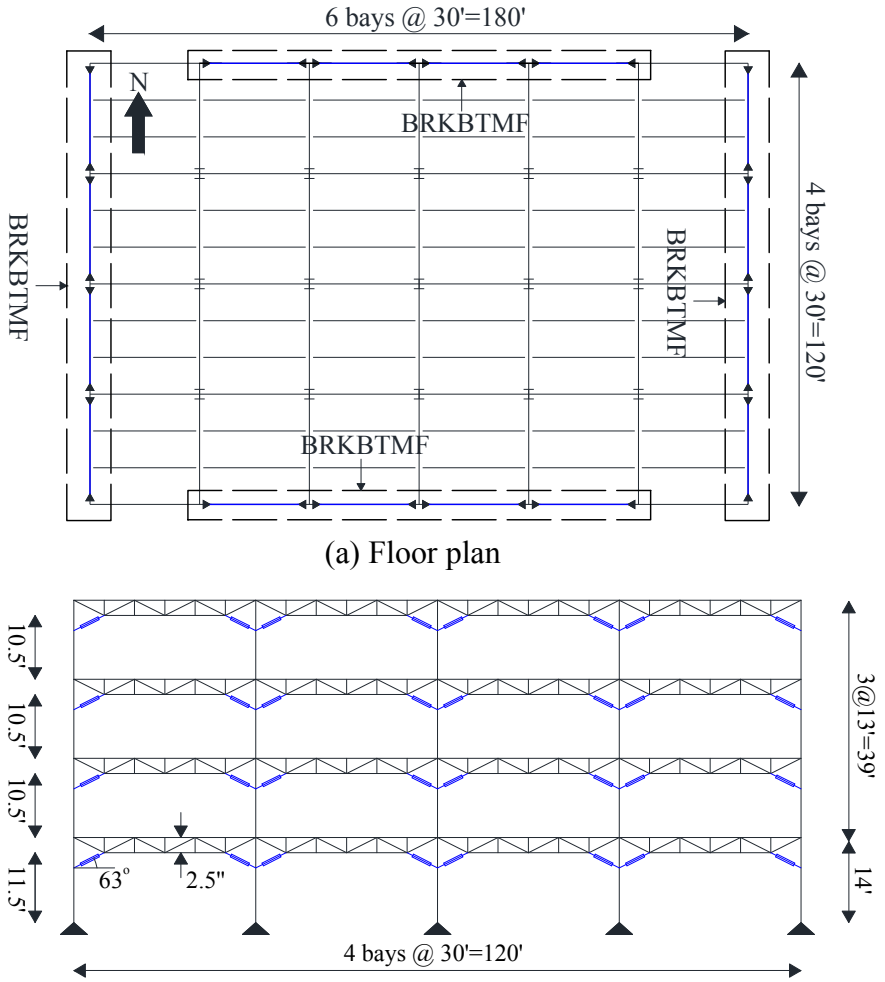

Figure 4.3 Building geometry

4.4 Design Demonstration

A design example of BRKBTMF using PBPD method was shown in this section. As discussed previously, the designer could choose any BRB inclination and span for this system. In this design demonstration, an angle of 63˚ and span of 30 ft. were selected as shown in Figure 4.3(b).

The prototype building was designed for two target objectives: 1) drift ratio less than 3.5% under the 2/50 hazard level; 2) less than 2.5% under 10/50 hazard level. The detailed design calculation can be found in Appendix A. Table 4.2 shows the building design parameters needed in PBPD procedure, and it also shows that the calculated base shear in 2/50 hazard level dominates the design. Table 4.3 shows the final member sizes and Figure 4.4 shows the definition of truss members.

Table 4.2 Design parameters of prototype building

Design Parameters	10/50 hazard level (2/3MCE)	2/50 hazard level (MCE)
S_a	0.78	1.18
T	1.0	1.0
Yield drift ratio, θ_y	0.75	0.75
Target drift ratio, θ_u	2.5	3.5
Design base shear / building weight (V / W)	0.158	0.174

Table 4.3 Sizes of structural component of sample BRKBTMF

Flo-or	BRB Strength [kips]	Column Sizes		Truss			
		Exterior	Interior	Top/Bottom Chord	Diagonal Chord	Vertical Chord	Ext. Vert. Chord
4	172	W24x207	W24x229	2MC8x18.7	2MC6x12	L3.5x3.5x5/16	2L3.5x3.5x5/16
3	259			2MC10x25	2MC6x15.3	L3.5x3.5x5/16	2L3.5x3.5x5/16
2	312	W24x279	W24x306	2MC10x28.5	2MC6x15.3	L3.5x3.5x5/16	2L3.5x3.5x5/16
1	339			2MC10x28.5	2MC8x18.7	L3.5x3.5x5/16	2L3.5x3.5x5/16

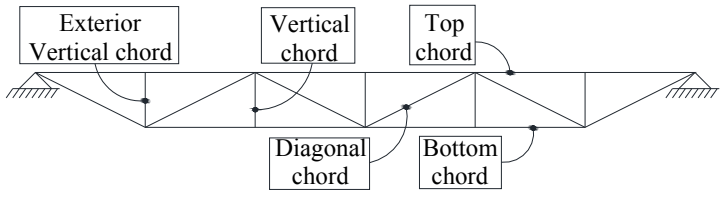

Figure 4.4 Truss member definition

4.5 Structural Response of Prototype Building

The modeling approach as outlined in Chapter 3 was used here to study the nonlinear static and dynamic response of the prototype building. The pushover analysis was conducted by applying monotonic lateral forces as defined by Equation 2.9. Figure 4.5 shows the pushover curve for the prototype building. As shown in the figure, the prototype building had a design base shear coefficient of 0.174. The pushover curve also showed that the yielding and factures of the BRBs at different roof drift ratios. Most of the first-story BRBs yielded when the roof top drift ranged between 0.4% and 0.6%. Similarly, the second-story, third-story and fourth-story yielded when the roof top drift ranged are between 0.5% and 0.75%, 0.6% and 1.1%, 1% to 1.5%, respectively. The first fracture occurred at the first floor when the roof drift ratio reached 2%. Sequential fracture of the rest of the BRBs at the second, third and fourth floor caused the structure to collapse. Note that the fracture limit of the BRB was set to follow lognormal distribution with median of 2.5% and 0.4 dispersion. In overall, the BRKBTMF structure performed well with relatively high stiffness without too much overstrength. The pushover also revealed some important building parameters as following. The overstrength factor, $\Omega = 0.225/0.174 = 1.3$, was defined as ultimate strength over yield strength. The ductility ratio, $\mu = 3.0/0.6 = 5.0$, was defined as the ratio of deformation at 80% of the ultimate strength at the softening range to the yield deformation. The ductility factor, $R_d = 1.18/0.225 = 5.2$, was defined as the ratio of required elastic strength due to pseudo-acceleration at the first mode and ultimate strength of the system.

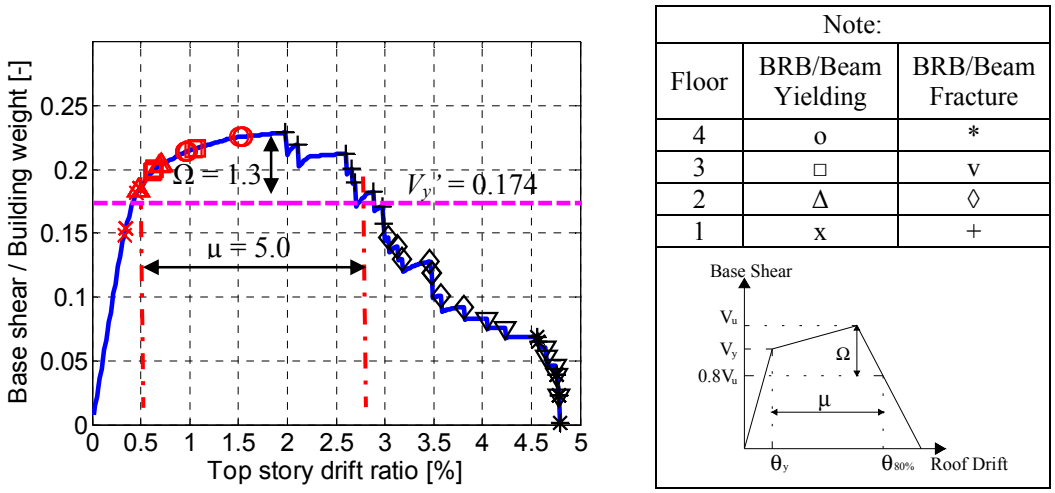

Figure 4.5 Pushover of prototype building

Nonlinear response time history analysis was conducted to simulate the behavior of the BRKBTMF under earthquakes presented in Table 4.1. Figure 4.5 shows the median peak response of the prototype building. The result showed the median peak inter-story drift was less than the target drift, 2.5% and 3.5% for the 10/50 and 2/50 hazard levels, respectively. And BRKBTMF had controlled floor acceleration under three hazard levels.

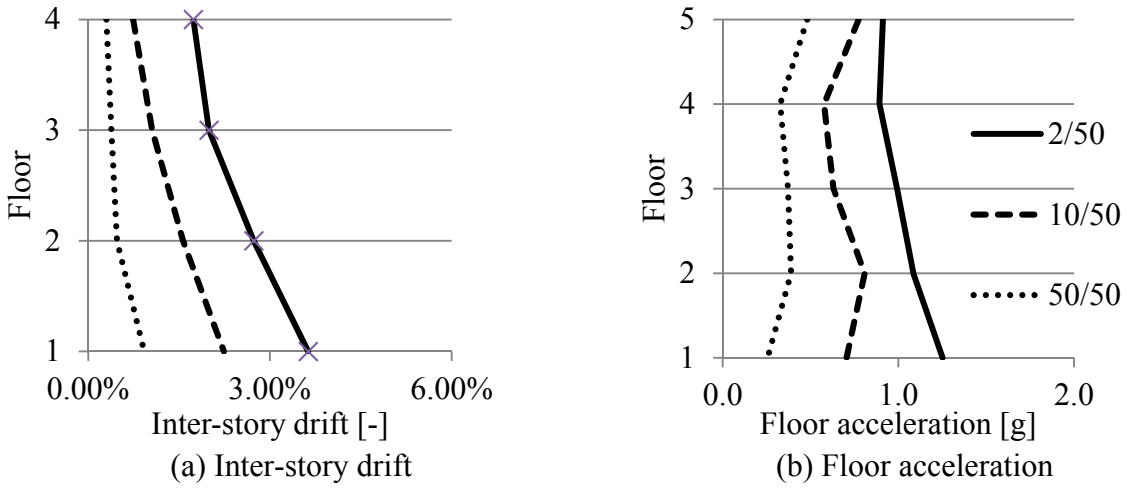

(a) Inter-story drift (b) Floor acceleration

Figure 4.6 Median peak response of prototype building

Incremental dynamic analysis (IDA) was conducted to estimate the structural performance under different earthquake intensities. Figure 4.7 shows the IDA response of the prototype

building. The vertical axis represented the shaking intensity. The horizontal axis represented the maximum inter-story drift ratio. When the IDA curve became flat, it meant the structure started to have large inter-story drift with small increase in shaking intensity. Such intensity was defined as the collapse intensity for the structure under the particular earthquake. Figure 4.8 shows the collapse probability curve obtained from the IDA response shown in Figure 4.7. These collapse probabilities was calculated from the ratio of number of ground motions that caused collapse to the total number of ground motions used in the analysis. It was observed that BRKBTMF had a collapse probability of 10% in the 2/50 hazard level (1.18g). The prototype building had a median collapse spectrum acceleration of 1.9g. This showed the structure had a collapse margin ratio (CMR) of 1.65 (1.95/1.17).

4.6 Summary

This chapter utilized performance-based plastic design (PBPD) procedure to design the prototype BRKBTMF system. The dynamic nonlinear analysis was conducted for the prototype to validate the design procedure and the building performed well as intended, with maximum drift less than target drift and controlled floor accleration. Incremental dynamic analysis was also conducted and the system showed good seismic performance with less than 10% collapse probability under 2/50 hazard level.

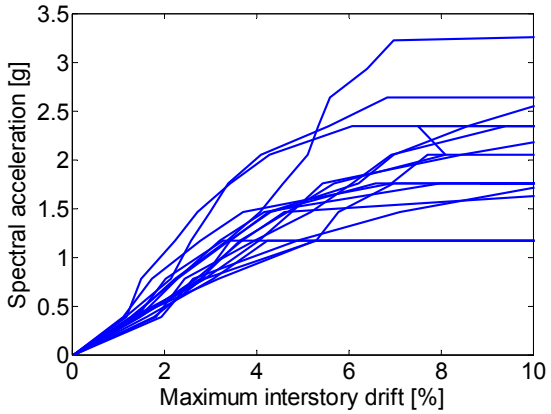

Figure 4.7 Dynamic response of prototype building in incremental dynamic analysis

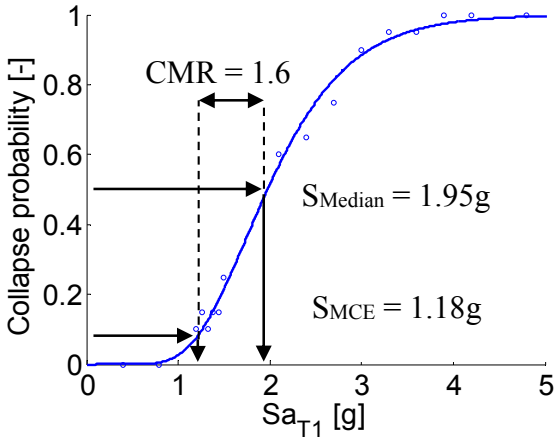

Figure 4.8 Fragility curve of prototype building

Chapter 5 Performance-Based Methodology for Evaluating the Structural Framing System

In order to assess the seismic performance of BRKBTMF system, the performance-based earthquake engineering (PEER) assessment framework established by the Pacific Earthquake Research Center was used. This PEER performance assessment methodology was further developed by Yang et al. (2009b), and later adopted by the ATC – 58 research team, using a Monte Carlo simulation procedure to quantify the performance of different structural facilities. This chapter introduced the state-of-the-art financial loss simulation procedure to evaluate seismic performance of BRKBTMF system.

5.1 Performance-Based Earthquake Engineering (PBEE) Framework

The performance assessment framework consists of four analysis phases, including seismic hazard analysis, response analysis, damage analysis, and loss analysis as shown in Figure 5.1.

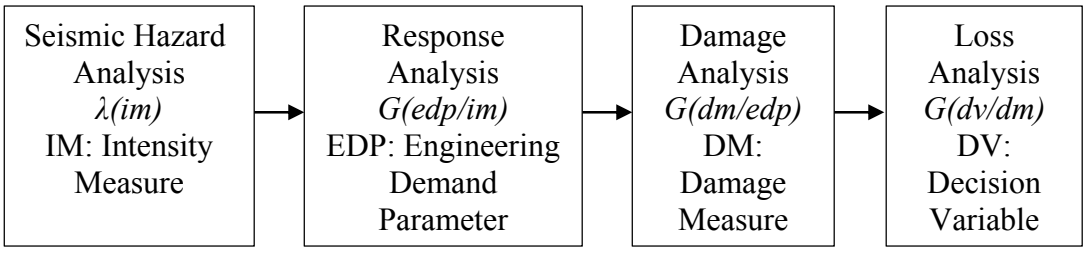

Figure 5.1 Performance-assessment framework (permission from Yang et al., 2009b)

These four analysis phases were explained below.

1. Seismic hazard analysis:

The seismic analysis was adopted from UC Berkley design guide (UCB, 2003), which utilized probabilistic seismic hazard analysis (PSHA) to quantify the seismic hazard for the prototype site. The PSHA was first proposed by Cornell (1968). It took into account the earthquake sources, the distance to the fault, uncertainties in prototype site, location and ground motion intensity and used a total probability theorem to quantify the probabilistically distribution of the shaking intensity of the site. The outcome of PSHA was a seismic hazard curve, $\lambda(IM)$, that quantified the annual rate of exceedance at a given value of seismic intensity measure (IM). This could also be used to select suitable ground motions for analysis.

2. Response analysis:

Response analysis quantified the structural and non-structural response the building experienced during the earthquake excitation. The peak response was obtained through nonlinear dynamic analysis. The outcome of response analysis were statistical distribution of the structural response (such as inter-story drift ratios and peak floor accelerations) at different levels of earthquake shaking intensities.

3. Damage analysis:

Key structural and non-structural components of the building could be identified and grouped into different performance groups (PGs). Each performance group consisted of one or more building components whose performance was similarly affected by a particular engineering demand parameter. A sufficient number of damage states (DS) should be defined for each performance group to describe the range of damage for the

components at different levels of structural response. Such damage states were typically defined using fragility curves. Figure 5.2 shows an example fragility curve. The horizontal axis represented the engineering demand parameter (e.g. inter-story drift) and the vertical axis represented the probability that the performance group in each of the damage states. In this example fragility curve, the component had two damage stages, undamaged (DS1) or damaged (DS2). And the damage stage of the component would depend on the building inter-story drift ratio. If the maximum building inter-story drift ratio reached 4%, there was 62% probability that this component would be damaged and 38% probability that it would be undamaged. These fragility curves were usually derived from past experimental data, expert judgment, and post-earthquake reconnaissance reports.

Using the results for the response analysis (step 2) and the damage analysis mentioned previously, a unique damage state was determined for each performance group. The damage state was obtained by identifying the probability of the performance group experiencing the damage state corresponding to structural response obtained from the response analysis. A uniform random number generator, was used to select the damage state. Once the damage state for a performance group was identified, the repair action and the associated repair cost for that performance group was obtained from a look up table. The process was repeated for all performance groups and the repair cost for the building was determined by summing cost from all performance groups. Because the repair items could be similar among different performance groups. (for example, the repair for the first floor ceiling could be repaired at the same time as the second floor ceiling), the total repair cost was calculated by summing the total repair quantities of similar items and multiplying the total repair quantities by a unit repair cost. The unit repair cost typically reduced as the

quantities increases. The unit repair cost used in this study reduced as a tri-linear function as shown in Figure 5.3. Note the unit repair cost also had uncertainties due to different repair sources if needed.

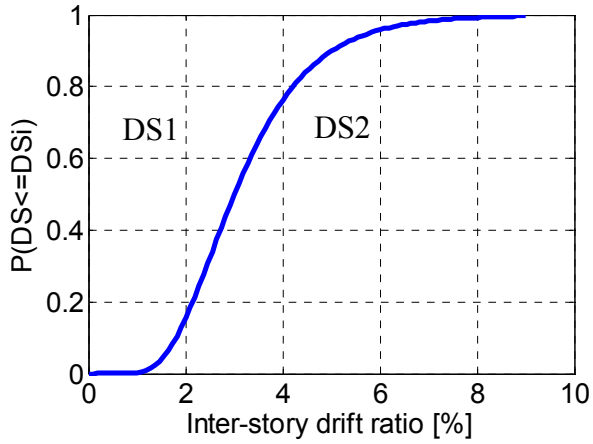

Figure 5.2 Example of component fragility curve

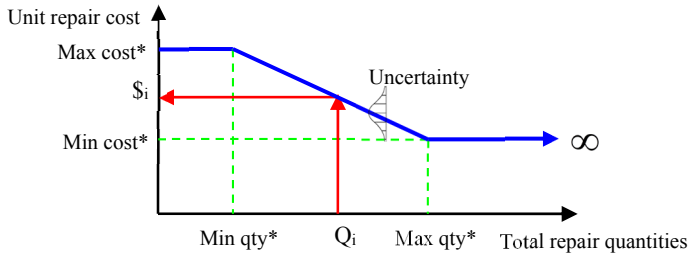

* Min qty = minimum quantities. Max qty = maximum quantities.

Max cost = maximum cost. Min cost = minimum cost.

Figure 5.3 Repair cost function model (permission by Yang et al., 2009b)

4. Loss analysis:

Steps 1 to 3 present a logical and consistent methodology that could be used to obtain a distribution of the total repair cost of the building for one intensity measure. Total

repair cost distribution of different intensities could be further identified by repeating the cost simulation process described in Steps 1 to 3 for a range of earthquakes.

5.2 Performance Groups for the Prototype Building

For the purpose of assessing building performance and repair costs, major structural and nonstructural components of the prototype building were identified and group into 25 performance groups (Table 5.1). These included: one seismic-force-resisting-system PG at each floor (1-4), one exterior non-structural PG at each floor (5-8), one interior displacement sensitive non-structural PG at each floor (9-12), one interior acceleration sensitive non-structural PG at each floor (13-16), one content PG at each floor (17-20), and one equipment PG at roof floor (21), one gravity system PG at each floor (22-25). All the PG data was based on the reports by Yang et al. (2009a) and ATC 58 (2008). Each performance group consisted of a collection of building components whose performance was similarly affected by a particular engineering demand parameter (EDP). For example, the structural components were assigned to performance groups whose performance was associated with inter-story drift in the story where the components were located. The nonstructural components and contents were subdivided into displacement-sensitive and acceleration-sensitive groups. The displacement-sensitive groups used inter-story drift ratios to define the performance, while the acceleration-sensitive groups used absolute floor level accelerations.

Table 5.1 Summary of performance group assignment

PG No.	PG Name	EDP	EDP description	PG description
1	SH12	du_1	Inter-storey drift between levels 1 and 2	Structural: seismic-force-resisting system (displacement sensitive)
2	SH23	du_2	Inter-storey drift between levels 2 and 3	
3	SH34	du_3	Inter-storey drift between levels 3 and 4	
4	SH4R	du_4	Inter-storey drift between levels 4 and roof	
5	EXTD12	du_1	Inter-storey drift between levels 1 and 2	Exterior non-structural (displacement sensitive)
6	EXTD23	du_2	Inter-storey drift between levels 2 and 3	
7	EXTD34	du_3	Inter-storey drift between levels 3 and 4	
8	EXTD4R	du_4	Inter-storey drift between levels 4 and roof	
9	INTD12	du_1	Inter-storey drift between levels 1 and 2	Interior non-structural (displacement sensitive)
10	INTD23	du_2	Inter-storey drift between levels 2 and 3	
11	INTD34	du_3	Inter-storey drift between levels 3 and 4	
12	INTD4R	du_4	Inter-storey drift between levels 3 and roof	
13	INTA2	a_2	Total acceleration at level 2	Interior non-structural (acceleration sensitive)
14	INTA3	a_3	Total acceleration at level 3	
15	INTA4	a_4	Total acceleration at level 4	
16	INTAR	a_R	Total acceleration at roof	
17	CONT1	a_g	Ground acceleration	Contents (acceleration sensitive)
18	CONT2	a_2	Total acceleration at level 2	
19	CONT3	a_3	Total acceleration at level 3	
20	CONT4	a_4	Total acceleration at level 4	
21	EQUIPR	a_R	Total acceleration at roof	Rooftop equipment (acceleration sensitive)
22	GS12	du_1	Inter-storey drift between levels 1 and 2	Gravity System (displacement sensitive)
23	GS23	du_2	Inter-storey drift between levels 2 and 3	
24	GS34	du_3	Inter-storey drift between levels 3 and 4	
25	GS4R	du_4	Inter-storey drift between levels 4 and roof	

Multiple damage states were defined for each performance group. The damage states were established at points along the damage continuum for which significant repair action would likely be triggered. For each damage state, a damage model (fragility relation) defined the conditional probability of damage being less than or equal to the threshold damage given the value of the engineering demand parameter associated with the performance group. The details of fragility curves, repair action, and repair cost of each performance group were described as following.

Seismic-force-resisting-system (SH) performance groups (PG 1-4)

BRKBTMF

The primary SFRS performance groups consisted of BRBs. That was because the rest of the seismic components (including columns and trusses) were designed to be elastic and checked during the dynamic time history analysis. The seismic structural components consisted of BRBs only. Such component had two damage stages: damaged or no damge. From literature review (López & Sabelli, 2004) and ATC58 (2008), BRBs had a median facture strain of 2.5% with dispersion of 0.4. Based on the geometry of the design, Equation 2.12 can be used to translate fracture strain into the global inter-story drift tolerance of the building. Table 5.2 shows the parameters used to define the structural performance group at different BRB configurations.

Table 5.2 BRB fragility parameters in this study

Chapter No.	Cases of parameters studies	Building drift tolerance, μ, DS2 [%]	Dispersion, β	Unit cost [$USD]				Quantity per floor
				Max. cost	Min. cost	Max. Qty.	Min Qty.	
Chapter 6	BRKBTMF w/ different BRB hysteresis	3.1	0.4	15,400	11,000	7	3	16
Chapter 7	30˚ BRKBTMF	4.5	0.4	15,700	11,200	7	3	16
	45˚ BRKBTMF	3.3	0.4	15,700	11,200	7	3	16
	63˚ BRKBTMF	3.1	0.4	15,400	11,000	7	3	16
	80˚ BRKBTMF	3.8	0.4	15,700	11,200	7	3	16
	90˚ BRKBTMF	5.0	0.4	16,000	11,400	7	3	16
Chapter 8	30 ft. BRKBTMF	3.1	0.4	17,100	11,600	7	3	20
	45 ft. BRKBTMF	3.1	0.4	21,400	14,500	7	3	16
	60 ft. BRKBTMF	3.1	0.4	21,700	14,700	7	3	12

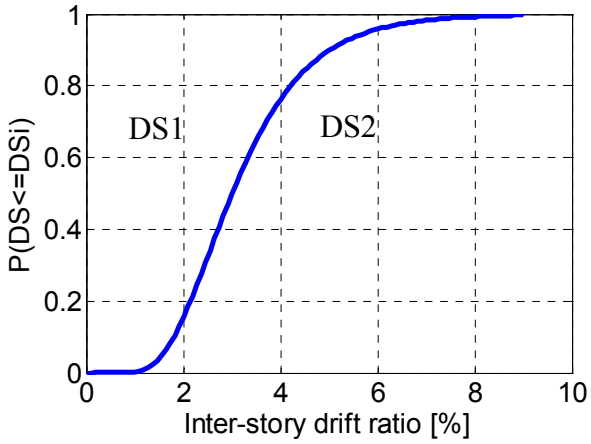

Figure 5.4 63˚ BRKBTMF BRB fragility curve

Table 5.3 Associated repair actions to BRB repairing

Repair items	Units	SH		Unit cost [$USD]			
		DS1	DS2	Max. cost	Min. cost	Max. Qty.	Min Qty.
Demolition / access							
Finish protection	$ft.^2$	0	6000	0.3	0.15	40000	1000
Ceiling system removal	$ft.^2$	0	5000	2	1.25	10000	1000
Drywall assembly removal	$ft.^2$	0	6000	2.5	1.5	20000	1000
Miscellaneous MEP	loc.	0	6	200	150	24	6
Remove exterior skin (salvage)	$ft.^2$	0	4000	30	25	10000	3000
Repair							
Welding protection	$ft.^2$	0	1500	1.5	1	10000	1000
Cut slab at damaged connection	$ft.^2$	0	1600	20	15	100	10
Replace slab	$ft.^2$	0	1600	20	16	100	1000
Put-back							
Misc. MEP and clean-up	loc.	0	6	300	200	24	6
Wall frame (studs and drywall)	$ft.^2$	0	6000	12	8	100	100
Replace exterior skin (salvage)	$ft.^2$	0	5600	35	30	10000	1000
Ceiling system	$ft.^2$	0	5000	8	5	60000	100

Sample BRB fragility curve is shown in Figure 5.4. The repair cost and quantity are tabulated in Table 5.3. In this example, the BRB had 2 DSs, DS1 meant the BRB was not damaged hence no repair required. DS2 meant BRB was fractured and needs to be replaced.

Moment Frame

Parameter study in Chapter 8 included the comparison between BRKTBMF and moment frame (MF) system, therefore, the performance group information for MF was included here. In general, beam-column moment connection was the primary SFRS performance group. The fragility data of beam-column moment connection was available in ATC58 (2008). Table 5.4 shows the fragility data and the associated repair unit price used for the case study in Chapter 8 . Note that μ and β were median and dispersion of damge state EDP, respectively. Figure 5.5 shows the fragility curves of a moment connection based on ATC58 (2008). Similar to BRKBTMF, the associated repair actions as shown in Table 5.3.

Table 5.4 Moment connection fragility parameters

Chapter No.	Cases of parameters studies	DS2 [%]		DS3 [%]		DS4 [%]		Unit cost [$USD]				Quantity per floor
		μ	β	μ	β	μ	β	Max. cost	Min. cost	Max. Qty.	Min Qty.	
Chapter 8	30 ft. MF	3	0.3	4	0.3	5	0.3	16,640	11,100	30	10	24
	45 ft. MF	3	0.3	4	0.3	5	0.3	25,000	16,600	30	10	16
	60 ft. MF	3	0.3	4	0.3	5	0.3	30,000	20,000	30	10	12

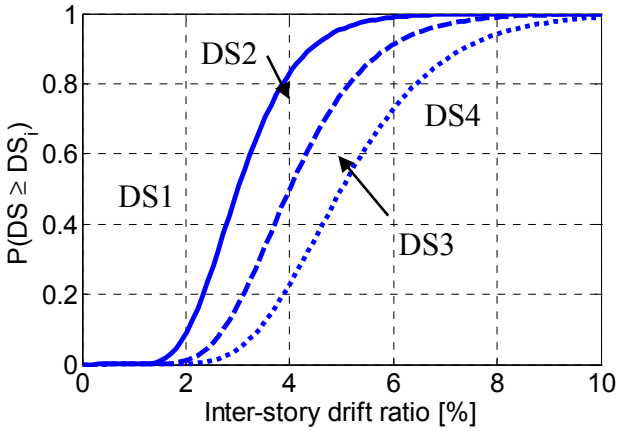

Figure 5.5 Fragility curve for typical moment connection

Exterior nonstructural (EXTD) performance groups (PG 5-8)

The exterior nonstructural performance groups mainly consisted of glass curtain walls at the exterior envelope of the building. The PACT database ATC58 (2008) and Yang et al. (2009a) were adopted for the fragility data and the unit repair cost. The unit repair cost of 5' x 6' curtain wall was around $USD 2055 per piece if order quantity was less than 20 pieces, $USD 1096 per piece for order quantity bigger than 100 pieces. The unit cost of curtain wall per square feet could be calculated as $USD 69 for quantity less than 3000 square feet, and $USD 37 for quantity greater than 6000. In this case, the total area of curtain wall at each floor was equal to (180*120)*2*13 = 7800 square feet. The fragility data is shown in Table 5.5 and the corresponding fragility curve is shown in Figure 5.6. The unit cost, repair quantity, the associated repair action taken into account are shown in shown in Table 5.6.

Table 5.5 EXTD PGs fragility parameters

PGs	DS2 [%]		DS3 [%]	
	μ	β	μ	β
Ext. PGs	3.38	0.4	3.83	0.4

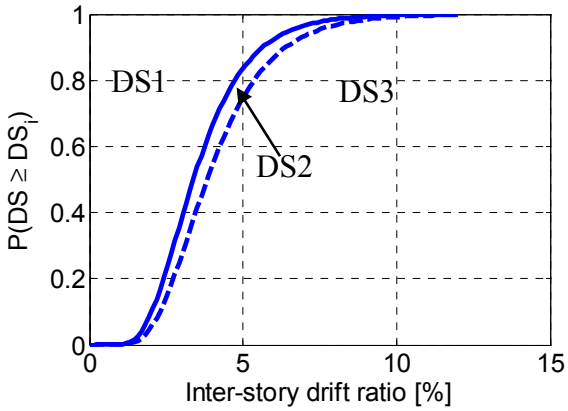

Figure 5.6 Fragility curve for EXTD PGs

Table 5.6 Associated repair actions to EXTD PGs repairing

Repair items	Units	Quantity per floor			Unit cost [$USD]			
		DS1	DS2	DS3	Max. cost	Min. cost	Max. Qty.	Min Qty.
Nonstructural exterior envelope demolition								
Erect scaffolding	$ft.^2$	0	6000	6000	2.5	2	10000	1000
Remove damaged curtained wall	$ft.^2$	0	7800	7800	20	15	1000	100
Miscellaneous access	$ft.^2$	0	8400	8400	20	15	1000	100
Nonstructural exterior envelope put-back								
Install new curtain wall	$ft.^2$	0	7800	7800	69	37	600	3000
Miscellaneous put-back	ea.	0	8400	8400	10	7	10000	1000
Site clean-up	$ft.^2$	0	6000	6000	1.5	0.75	10000	1000

Interior nonstructural displacement sensitive (INTD) performance groups (PG 9-12)

The interior nonstructural displacement sensitive performance groups mainly consisted of partitions, doors and glazing inside the building. The PACT database ATC58 (2008) and Yang et al. (2009a) were adopted for the fragility data and the unit repair cost. The fragility data of INTD is tabulated in Table 5.7 and the corresponding fragility curve is shown in Figure 5.7. The corresponding unit cost, repair quantity and the associated repair action taken into account are shown in Table 5.8.

Table 5.7 INTD PGs fragility parameters

PGs	DS2 [%]		DS3 [%]	
	μ	β	μ	β
Int. nonstructural displacement PGs	0.39	0.17	0.9	0.23

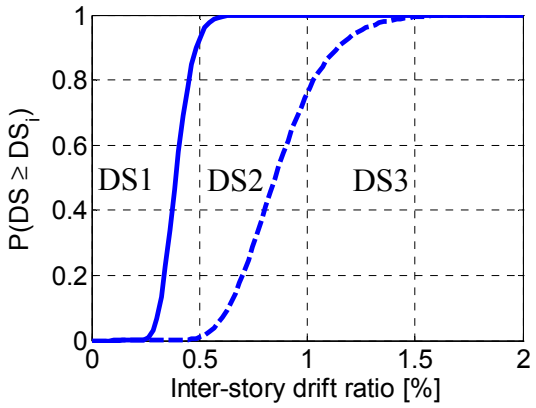

Figure 5.7 Fragility curve for INTD PGs

Table 5.8 Associated repair actions to INTD PGs repairing

Repair items	Units	Quantity per floor for			Unit cost [$USD]			
		DS1	DS2	DS3	Max. cost	Min. cost	Max. Qty.	Min Qty.
Structural demolition / access Finish protection	ft.^{2}	0	5000	10000	0.15	0.13	40000	1000
Nonstructural demolition								
Remove furniture	ft.^{2}	0	5000	10000	2	1.25	1000	100
Carpet removal	ft.^{2}	0	0	10000	1.5	1	20000	1000
Drywall removal	ft.^{2}	0	0	10000	2.5	1.5	20000	200
Door and frame removal	ea.	0	8	8	40	25	48	12
Interior glazing removal	ft.^{2}	0	100	100	2.5	2	5000	500
Ceiling system removal	ft.^{2}	0	0	5000	2	1.25	20000	1000
MEP removal	ft.^{2}	0	0	1000	40	15	10000	100
Remove casework	lf.	0	0	200	20	15	10000	100
Interior construction								
Drywall construction/paint	ft.^{2}	0	0	10000	12	8	25000	500
Doors and frames	ea.	0	8	25	48	12	600	400
Interior glazing	ft.^{2}	0	100	400	45	30	15000	100
Carpet and rubber base	ft.^{2}	0	0	10000	6	4	30000	500
Patch and paint partitions	ft.^{2}	0	5000	5000	2.5	2	10000	1000
Replace ceiling system	ft.^{2}	0	0	5000	2	1.5	20000	1000
MEP replacement	ft.^{2}	0	0	1000	80	60	1000	100
Replace casework	lf.	0	0	200	70	50	1000	100

Table 5.9 INTA PGs fragility parameters

PGs	DS2 [g]		DS3 [g]		DS4 [g]	
	μ	β	μ	β	μ	β
Int. nonstructural acceleration PGs	1.0	0.15	1.5	0.20	2	0.20

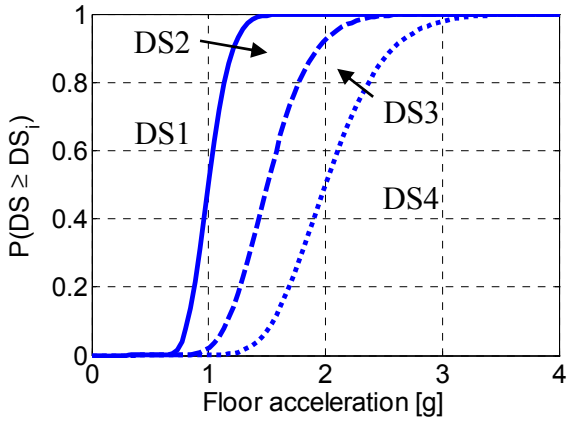

Figure 5.8 Fragility curve for INTA PGs

Table 5.10 Associated repair actions to INTA PGs repairing

Repair items	Units	Quantity per floor for				Unit cost [$USD]			
		DS1	DS2	DS3	DS4	Max. cost	Min. cost	Max. Qty.	Min Qty.
General clean up									
Water damage	ft.^{2}	0	0	10000	20000	0.15	0.1	20000	1000
Structural demolition/access									
Finish protection	ft.^{2}	0	4000	10000	20000	0.3	0.15	40000	1000
Nonstructural demolition									
Remove furniture	ft.^{2}	0	4000	10000	20000	2	1.25	1000	100
Ceiling system removal	ft.^{2}	0	0	0	20000	2	1.25	20000	1000
MEP removal	ft.^{2}	0	0	500	2000	40	15	10000	100
Interior construction									
Replace ceiling tiles	ft.^{2}	0	2500	8000	8000	2	1.5	20000	1000
Replace ceiling system	ft.^{2}	0	0	0	20000	3	2.5	20000	1000
MEP replacement	ft.^{2}	0	0	500	2000	80	60	1000	100

Interior nonstructural acceleration sensitive (INTA) performance groups (PG 13-16)

The interior nonstructural acceleration sensitive performance groups mainly consisted of ceilings, lights, sprinkler heads, etc. The PACT database ATC58 (2008) and Yang et al. (2009b) were adopted for the fragility data and the unit repair cost. The fragility data of INTA is tabulated in

Table 5.9 and the corresponding fragility curve is shown in Figure 5.8. The corresponding unit cost, repair quantity and the associated repair action taken into account are shown in Table 5.10.

Content (CONT) performance groups (PG 17-20)

The content performance groups mainly consisted of office equipment, computer, books or paper. The content performance groups in the office building could be costly when more valuable equipment was placed in the office. The PACT database ATC58 (2008) and Yang et al. (2009b) were adopted for the fragility data and the unit repair cost. The fragility data of CONT is tabulated in Table 5.11 and the corresponding fragility curve is shown in Figure 5.9. The corresponding unit cost, repair quantity and the associated repair action taken into account are shown in Table 5.12.

Table 5.11 CONT PGs fragility parameters

PGs	DS2 [g]		DS3 [g]		DS4 [g]	
	μ	β	μ	B	μ	β
Int. nonstructural acceleration PGs	0.3	0.20	0.7	0.22	3.5	0.25

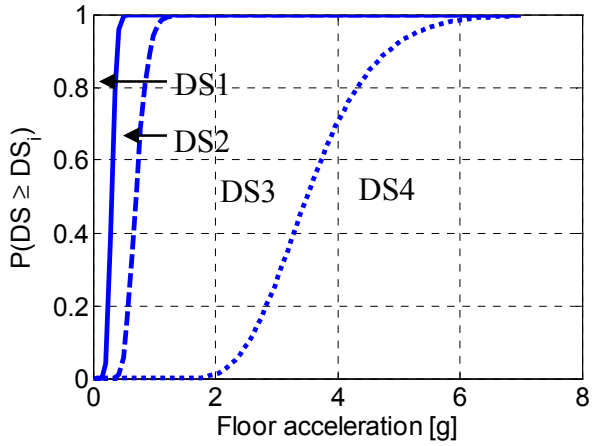

Figure 5.9 Fragility curve for CONT PGs

Table 5.12 Associated repair actions CONT PGs repairing

Repair items	Units	Quantity per floor				Unit cost [$USD]			
		DS1	DS2	DS3	DS4	Max. cost	Min. cost	Max. Qty.	Min Qty.
General clean-up									
Office papers & books	$ft.^2$	0	0	10000	10000	0.1	0.06	10000	1000
Office equipment	$ft.^2$	0	5000	10000	10000	0.06	0.04	10000	10000
Loose furniture / file drawers	$ft.^2$	0	10000	20000	20000	0.05	0.03	20000	20000
Contents									
Conventional office	$ft.^2$	0	0	0	20000	25	21	0	10000

Roof equipment (EQUIPR) performance groups (PG 21)

The roof equipment groups mainly consisted of elevator equipment which was usually on the top of the building and governed by the roof acceleration. The PACT database ATC58 (2008) and Yang et al. (2009b) were adopted for the fragility data and the unit repair cost. The fragility data of EQUIPR is tabulated in Table 5.13 and the corresponding fragility curve is shown in Figure 5.10. The corresponding unit cost, repair quantity and the associated repair action taken into account are shown in Table 5.14.

Table 5.13 EQUIPR PGs fragility parameters

PGs	DS2 [g]		DS3 [g]	
	μ	β	μ	β
Roof equipment acceleration PGs	1.0	0.15	2.0	0.20

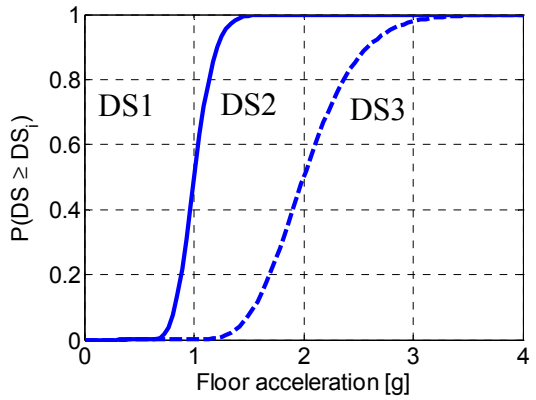

Figure 5.10 Fragility curve for EQUIPR PGs

Table 5.14 Associated repair actions EQUIPR PGs repairing

Repair items	Units	Quantity per floor			Unit cost [$USD]			
		DS1	DS2	DS3	Max. cost	Min. cost	Max. qty.	Min qty.
General clean-up Loose furniture / file drawers	ft.^{2}	0	0	50000	0.05	0.03	20000	20000
Roof-top MEP								
Repair in place	ft.^{2}	0	1	1	200,000	200,000	2	1
Remove and replace	ft.^{2}	0	0	1	10,000	10,000	2	1

Gravity system (GS) performance groups (PG 22-25)

Shear tab connection was the primary gravity system performance groups. The fragility data of shear tab connection was available in ATC58 (2008) and it is tabulated in Table 5.15 and shown in the format of fragility curve in Figure 5.5. Table 5.15 also shows the unit cost, repair quantities of the gravity connections. The associated repair actions as shown in Table 5.3 should be included in the simulation.

Table 5.15 GS PGs fragility parameters

Chapter No.	Cases of parameters studies	DS2 [%]		DS3 [%]		DS4 [%]		Unit cost [$USD]				Quant-ity per floor
		μ	β	μ	β	μ	β	Max. cost	Min. cost	Max. Qty.	Min Qty.	
Chapter 6	30 ft. Blg.	4	0.4	8	0.4	11	0.4	15,300	10,200	30	10	40
Chapter 7	30 ft. Blg.	4	0.4	8	0.4	11	0.4	15,300	10,200	30	10	40
Chapter 8	30 ft. Blg.	4	0.4	8	0.4	11	0.4	15,300	10,200	30	10	40
	45 ft. Blg.	4	0.4	8	0.4	11	0.4	21,400	14,300	30	10	24
	60 ft. Blg.	4	0.4	8	0.4	11	0.4	34,200	22,800	30	10	17

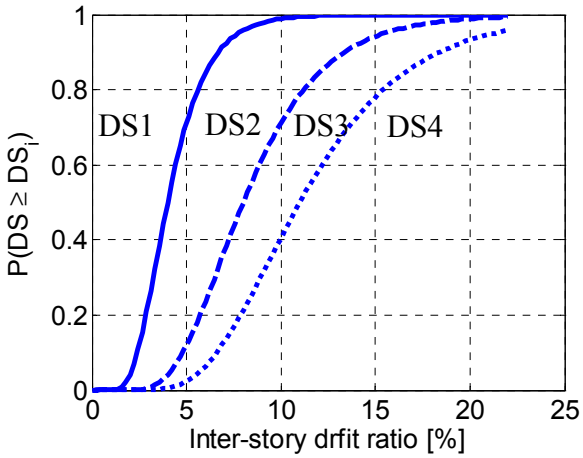

Figure 5.11 Fragility curve for GS PGs

5.3 PBEE Assessment on the Prototype Building

In this section, seismic performance of prototype BRKBTMF under the three hazard levels (2/50, 10/50, 50/50) was conducted using the state-of-the-art seismic performance assessment procedure outlined in this chapter.

Figure 5.12 shows the deaggregation of the total repair cost of the prototype building under three hazard levels considered. In the 2/50 hazard level, most of the interior nonstructural component PGs (PGs 9 - 12) were damaged. This was because the building has high inter-story drift ratio which was much higher than the tolerable deformation from these components as shown in Figure 5.7. The exterior nonstructural components (PGs 4 - 8) and structural components (PGs

1 - 4) had less damage probability than the interior nonstructural component PGs (PGs 9-12), but their repair cost was higher due to higher unit repair cost. This revealed that the structural components and non-structural exterior components (PGs 1-8) were more costly than interior non-structural components (PGs 9-12). Gravity system (PG 22-25) were also sensitive to the displacement. They also experienced partial damages, but less repair cost was required compared to PGs 1-8. The acceleration sensitive components (PGs 13 - 21) had much less repair probability because the building had controlled acceleration and these components were not severely damaged. As the shaking intensity decreased, the damage decreased. Figure 5.13 shows the cumulative distribution function (CDF) of the total repair cost for the three hazard levels considered. Note that the cost simulation also considered the collapse of the building. If the collapse was detected, the building replacement cost was used in the total repair costs. The result showed that the repair cost became higher as the earthquake intensity increased. The information presented here could be used to make risk management decisions. For example, the prototype building had a median (50% probability of exceedance) repair cost of $USD 3.7 million dollars under 2/50 hazard level. Because each hazard had different annual return rate, the loss curves could also be combined using the total probability theory to calculate the annualized loss. Figure 5.14 shows the annualized curve of the prototype building. The result showed the prototype building had an annual rate of 0.5% where the total repair cost would exceed $USD 1 million dollars, which was low annual probability of cost exceedance. If one used the area under the annualized loss curve, one could quantify the mean annualized loss (MAL) of the prototype building under different range of earthquakes. The prototype building had mean annualized repair loss, MAL of the building, $USD 21,000. The owner could then use this information to decide if risk was tolerable for the prototype building.

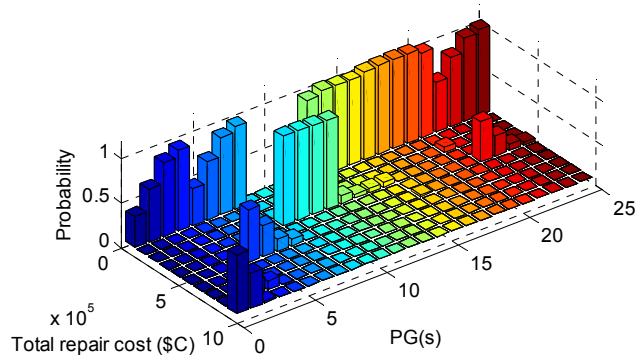

(a) 2/50 hazard level

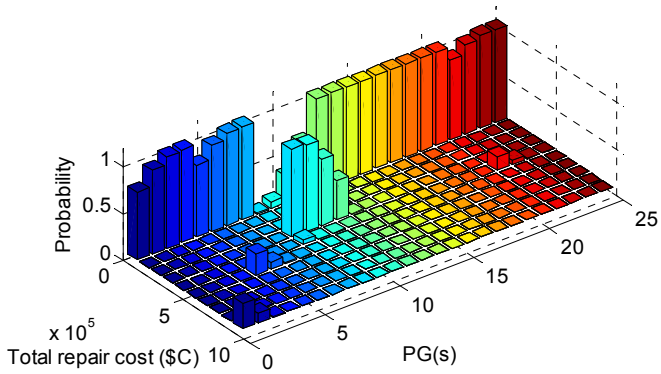

(b) 10/50 hazard level

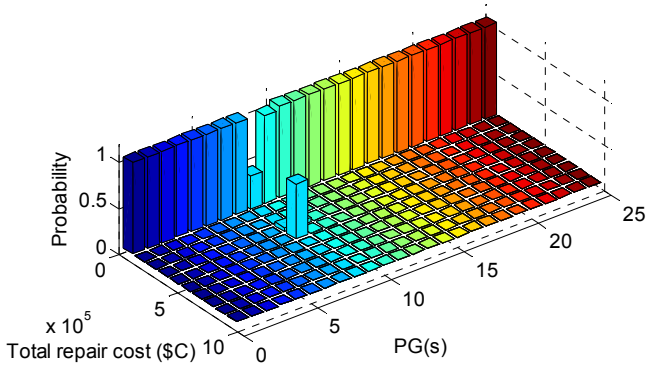

(c) 50/50 hazard level

Figure 5.12 Repair cost distribution for prototype building

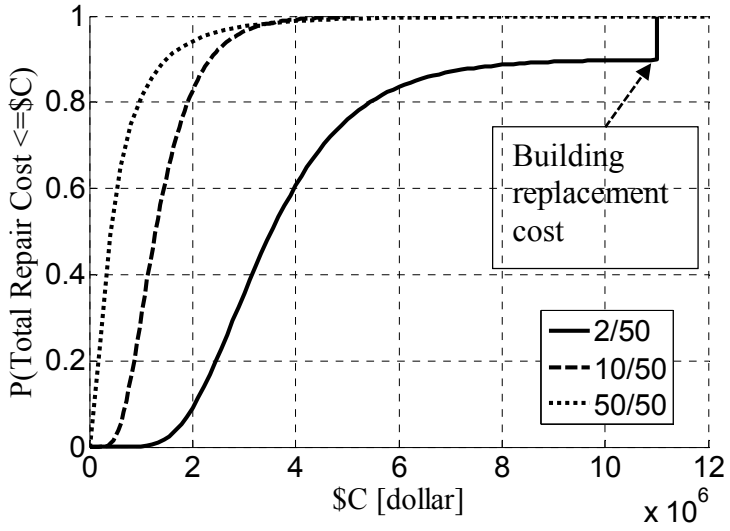

Figure 5.13 Total repair cost CDF under three hazards for prototype building

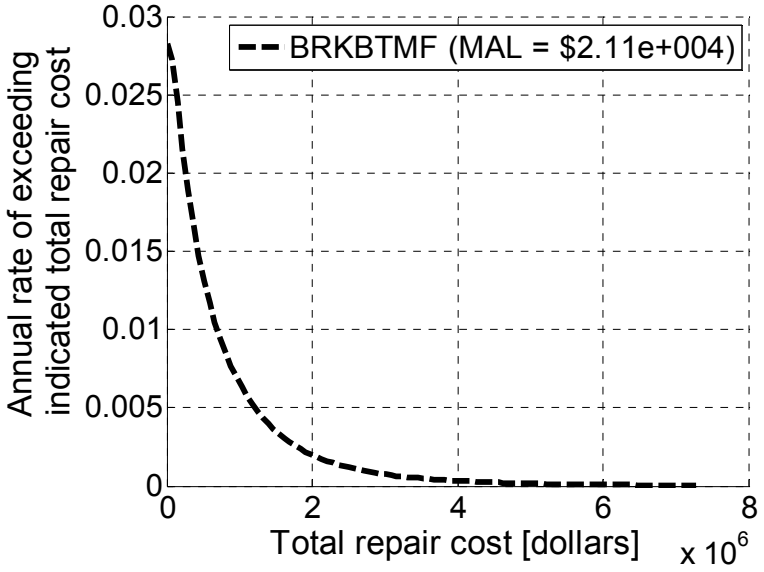

Figure 5.14 Life cycle cost for prototype building

5.4 Summary

This chapter utilized performance-based earthquake engineering (PEER) assessment framework to assess the seismic performance of the prototype BRKBTMF system. The result included the cumulative distribution function and deaggregation of total repair cost under three

hazard levels and the life cycle cost of the prototype BRKBTMF system. These results could be used immediately by the designers and owner to make risk management decisions of the building. The PBEE assessment framework was also used in Chapter 6, 7 and 8 to compare the financial impact from different important parameters to the BRKBTMF system.

Chapter 6 Parametric Study of BRB Hysteresis

Literature review showed that different BRBs had different strength hardening rules. This created many design challenges to engineers as they were required to capacity design the non-yielding components (such as the connections and columns). AISC 341 (2010) permitted the designer to use $P^{-}_{BRB,\max} = \omega\beta R_y P_y$ and $P^{+}_{BRB,\max} = \omega R_y P_y$ to calculate the maximum expected compression and tension forces for the BRBs. The definition of symbols were described in Chapter 2 . The BRB overstrength was highly dependent on the ω and β factors, which may affect the seismic performance of the system. Those two factors (ω and β) were usually provided by manufacturers and sometimes could vary significantly among different manufacturers. For example, Figure 3.5 shows very different overstrength among different BRBs. In order to study the influence of the BRB hysteresis on the BRKBTMF, the prototype office building described in Chapter 4 was used to compare the system performance with different BRB hardening rules.

6.1 Description of Parametric Study

To study the influence of the BRB overstrength on the system performance, the component test conducted by Iwata & Murai (2006) was chosen as the benchmark model in this study and denoted as “Original”.

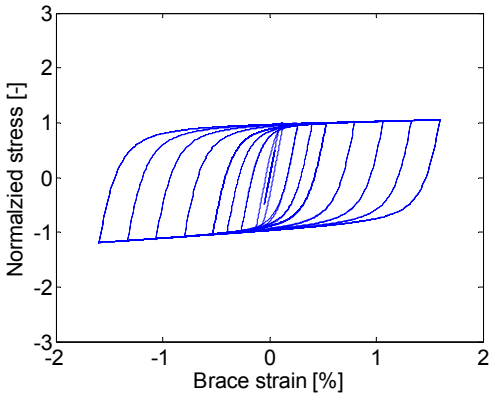

(a) Non. S.H.

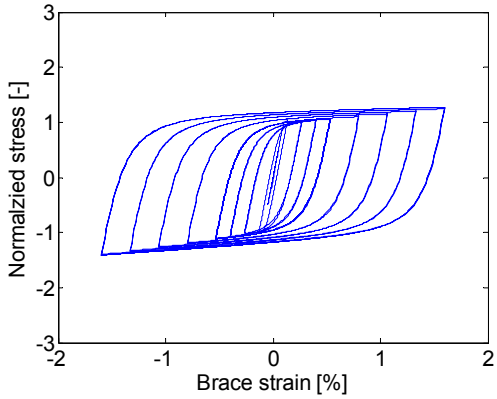

(b) 15% Less

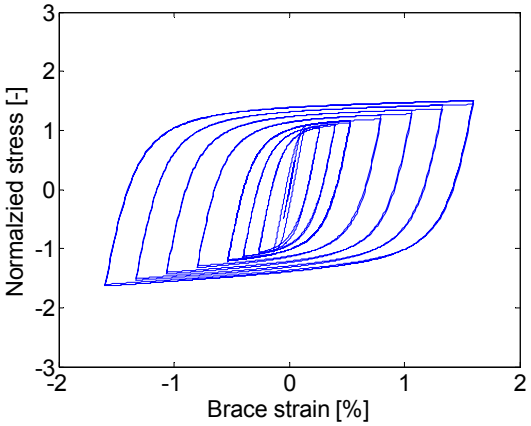

(c) Original

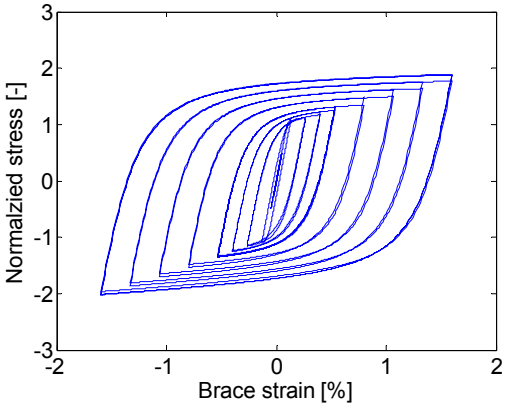

(d) 25% More

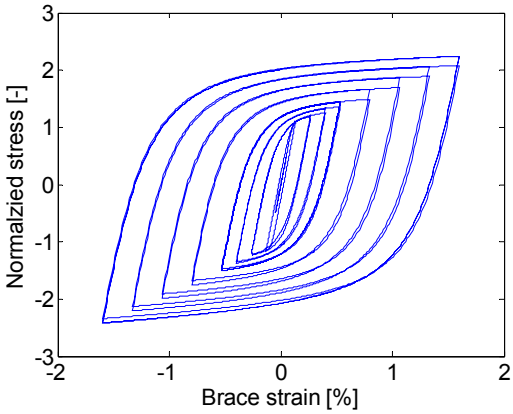

(e) 50% More

Note:

Type	ω	β
50% More	2.25	1.10
25% More	1.88	1.10
Original	1.50	1.10
15% Less	1.28	1.10
Non. S.H.	1.00	1.10

Figure 6.1 BRB hysteresis with different isotropic strain hardening

Five ω factors were used. The bench mark model had a ω factor of 1.5. If ω was scaled up 25% from the benchmark model, such model was denoted as "25% more". Similarly, ω factor

was scaled up 50% and down 15%. In addition, a model with no strain hardening was also included. Figure 6.1 shows the hysteresis of BRBs with different isotropic strain hardening with their corresponding overstrength factors. Two approaches were used to study the impact from BRB overstrength to the building. The first approach was to redesign the building including capacity design of the non-yielding elements based on the different hysteresis rules. The second approach was to design building only once but apply different BRB hysteresis to the building. The study would show the cost impact for the building from these two aspects. In order to study the repair cost for the truss and columns in the non-capacity design approach, additional seismic trusses and columns PGs were added into Table 5.1.

Table 6.1 Additional PGs for seismic truss and column

PG No.	PG Name	EDP	EDP description	PG description
26	TR12	du_1	Inter-storey drift between levels 1 and 2	Structural: seismic truss system (displacement sensitive)
27	TR23	du_2	Inter-storey drift between levels 2 and 3	
28	TR34	du_3	Inter-storey drift between levels 3 and 4	
29	TR4R	du_4	Inter-storey drift between levels 4 and roof	
30	COL12	du_1	Inter-storey drift between levels 1 and 2	Structural: seismic column system (displacement sensitive)
31	COL23	du_2	Inter-storey drift between levels 2 and 3	
32	COL34	du_3	Inter-storey drift between levels 3 and 4	
33	COL4R	du_4	Inter-storey drift between levels 4 and roof	

6.2 Capacity Design Approach

6.2.1 Structural Design

Following the capacity design approach as outlined in Chapter 2 , the building was redesigned based on different BRB hysteresis such that the component can remain elastic under earthquake shaking. Table 6.2 summarized the updated structural element sizes for the prototype building with different BRBs. Figure 6.2 shows the comparison to the initial structural costs for the five different configurations considered. The result was normalized with respect to the initial

cost for the default case, denoted as “Original”. The figure showed that as overstrength increased, the sizes for the none-yielding elements increased and this increased the initial cost of the structure. The result showed the BRB with 50% more overstrength would result in an 11% increase in initial cost. Similarly, there was about an 8% reduction to the initial structural cost if the BRB had no strain hardening.

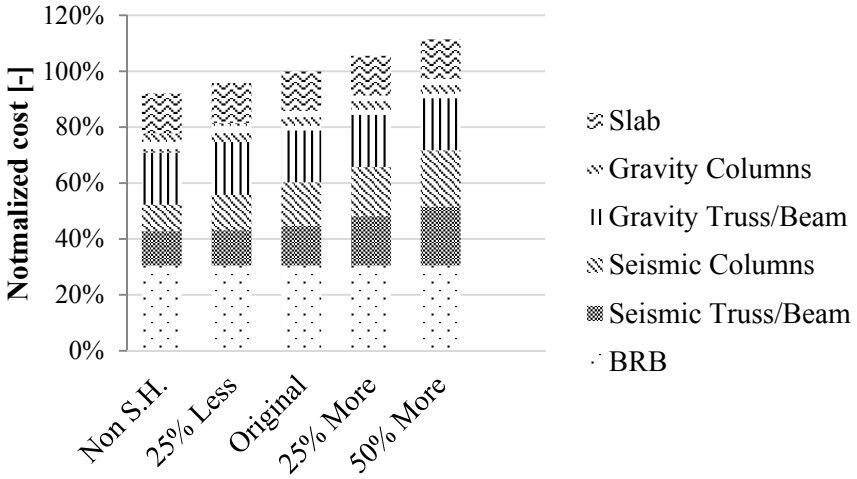

Figure 6.2 Cost breakdown for initial structural cost

6.2.2 Structural Response and Repair Cost

Figure 6.3 shows the median peak structural responses of buildings under the earthquakes shown in Table 4.1 with different BRB hysteresis. The result showed that the peak response was very comparable among these cases. In general, the trend showed that as BRB overstrength increased, this resulted to less inter-story drift ratio, but higher floor acceleration. Figure 6.4 shows the CDF of the repair cost for these five cases considered. The result showed that the structure with higher overstrength, BRB had less repair cost during a MCE level earthquake.

Table 6.2 Building sections

	Seismic Column		Seismic Truss		
Type	Non Strain Hardening				
Floor	Exterior	Interior	Chord	Diagonal	Vertical
4	W24X104	W30X116	2MC6x12	2MC6x6.5	L3.3x3.5x5/16
3	W24X104	W30X116	2MC6x15.1	2MC6x12	L3.3x3.5x5/17
2	W30X148	W36X160	2MC6x15.1	2MC6x12	L3.3x3.5x5/18
1	W30X148	W36X160	2MC6x16.3	2MC6x12	L3.3x3.5x5/19
Type	25% Less				
Floor	Exterior	Interior	Chord	Diagonal	Vertical
4	W33X118	W33X130	2MC6x12	2MC6x6.5	L3.3x3.5x5/16
3	W33X118	W33X130	2MC6x15.1	2MC6x12	L3.3x3.5x5/17
2	W33X169	W36X170	2MC6x16.3	2MC6x12	L3.3x3.5x5/18
1	W33X169	W36X170	2MC6x18	2MC6x12	L3.3x3.5x5/19
Type	Original				
Floor	Exterior	Interior	Chord	Diagonal	Vertical
4	W40X149	W36X160	2MC6x12	2MC6x7	L3.3x3.5x5/16
3	W40X149	W36X160	2MC6x18	2MC6x12	L3.3x3.5x5/17
2	W40X199	W40X199	2MC8x20	2MC6x12	L3.3x3.5x5/18
1	W40X199	W40X199	2MC10x22	2MC4x13.8	L3.3x3.5x5/19
Type	25% More				
Floor	Exterior	Interior	Chord	Diagonal	Vertical
4	W30X173	W36X182	2MC6x15.1	2MC4x13.8	L3.3x3.5x5/16
3	W30X173	W36X182	2MC8x21.4	2MC6x12	L3.3x3.5x5/17
2	W40X215	W36X230	2MC9x25.4	2MC6x15.1	L3.3x3.5x5/18
1	W40X215	W36X230	2MC10x28.5	2MC6x15.3	L3.3x3.5x5/19
Type	50% More				
Floor	Exterior	Interior	Chord	Diagonal	Vertical
4	W30X173	W36X182	2MC6x18	2MC6x12	L3.3x3.5x5/16
3	W30X173	W36X182	2MC9x25.4	2MC6x15.3	L3.3x3.5x5/17
2	W40X215	W36X230	2MC10x33.6	2MC6x18	L3.3x3.5x5/18
1	W40X215	W36X230	2MC10x33.6	2MC8x18.7	L3.3x3.5x5/19
BRB	Floor	1	2	3	4
Required Strength (kips)		311	286	237	157
Type	Gravity System				
Floor	Column	Truss			
4	W12X40	Direct.	Chord	Diagonal	Vertical
3	W12X40	E-W	2L2.5X2.5X1/4	2L2X2X3/16	L2X2X1/8
2	W12X65	N-S	2L5X5X3/8X3/4	2L3.5X3.5X5/16X3/4	L2X2X3/16
1	W12X65	Note: Fy(Beam/Truss/BRB) = 50 ksi; Fy(Column) = 55 ksi			

However, the repair cost difference was not large. That is because building with more overstrength had less damage in drift sensitive components and more damage in acceleration

sensitive components, which ended up with the same in the total repair cost as the building with less overstrength. This could be observed by the repair cost distribution shown in Figure 6.5.

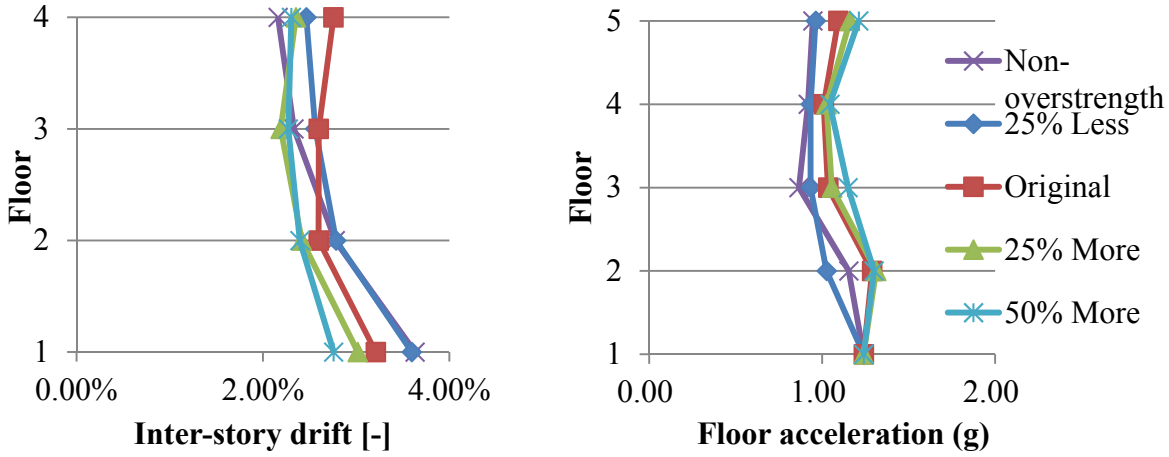

(a) Inter-story drift (b) Floor acceleration

Figure 6.3 Structural response 2/50 hazard level in capacity design approach

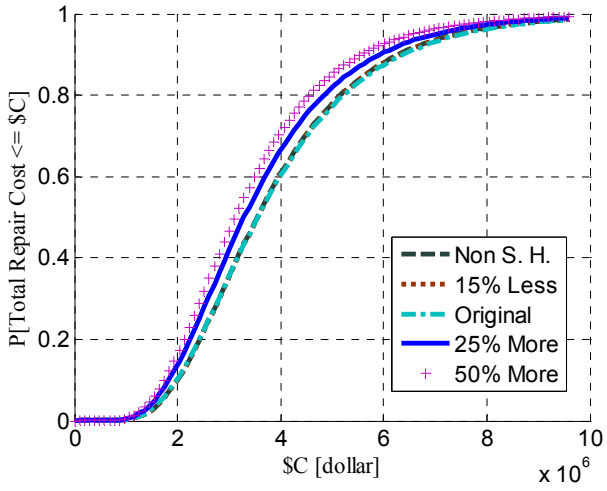

Figure 6.4 Cost CDF under 2/50 hazard level in capacity design approach

(a) None S. H.

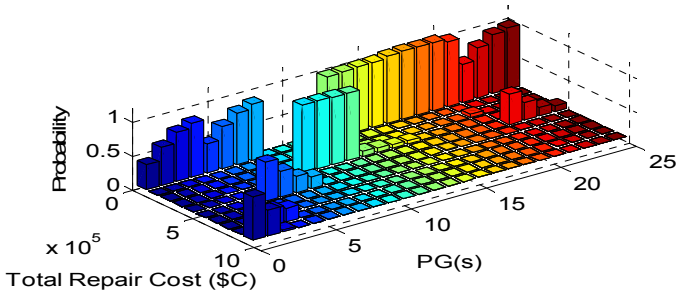

(b) 15% Less

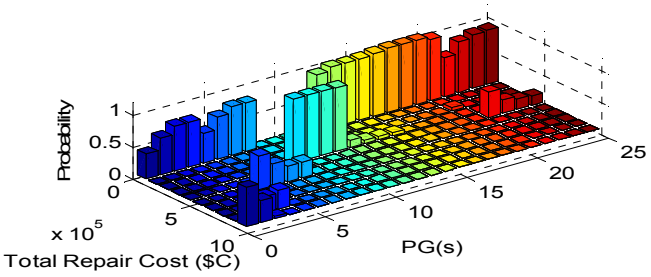

(c) Original

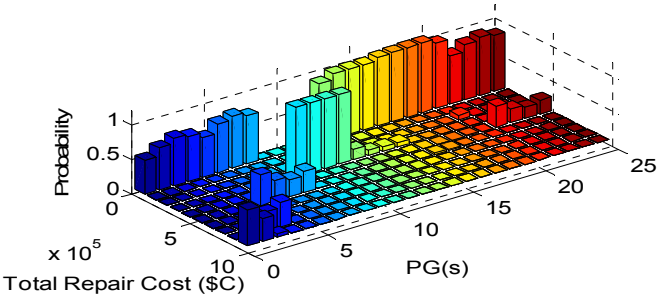

(d) 25% More

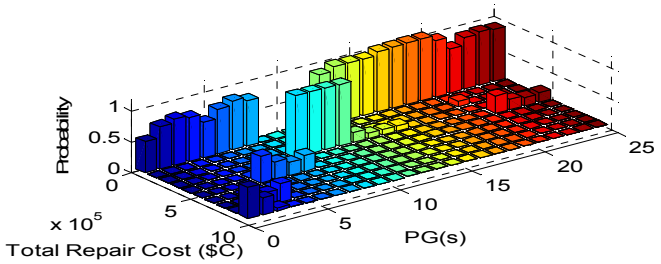

(e) 50% More

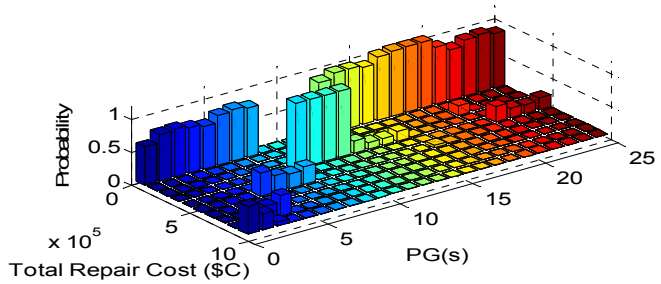

* Refer to Table 5.1 for definition of PGs

Figure 6.5 Cost distribution in capacity design approach

6.3 Non-capacity Design Approach

6.3.1 Structural Design

The non-capacity design approach as to study how sensitive the structure was, when the BRB installed into the building unexpectedly had more overstrength than the design. In this case, the existing system may not have enough capacity to take the full forces from BRBs and remain elastic. The structural design used here was the same as the one of "Original" in Table 6.2.

6.3.2 Structural Response and Repair Cost

Figure 6.6 shows the structural response of the five cases included in the non-capacity design study. It was found that the response was very close, while the 50% more overstrength case had less inter-story drift. However, when the performance based evaluation was conducted, the results in Figure 6.7 and Figure 6.8 show that the increasing in overstrength of BRBs results in significant damage to the rest of the components (seismic column and truss). Note that the "15% Less" and "Original" cases still had small amount of column and truss damages, and this was because the cost simulation analysis was probability based. Due to the dispersion of truss and column component fragility curve, the cost simulation predicts some damage would occur even though the structural model showed the components were still in the elastic range.

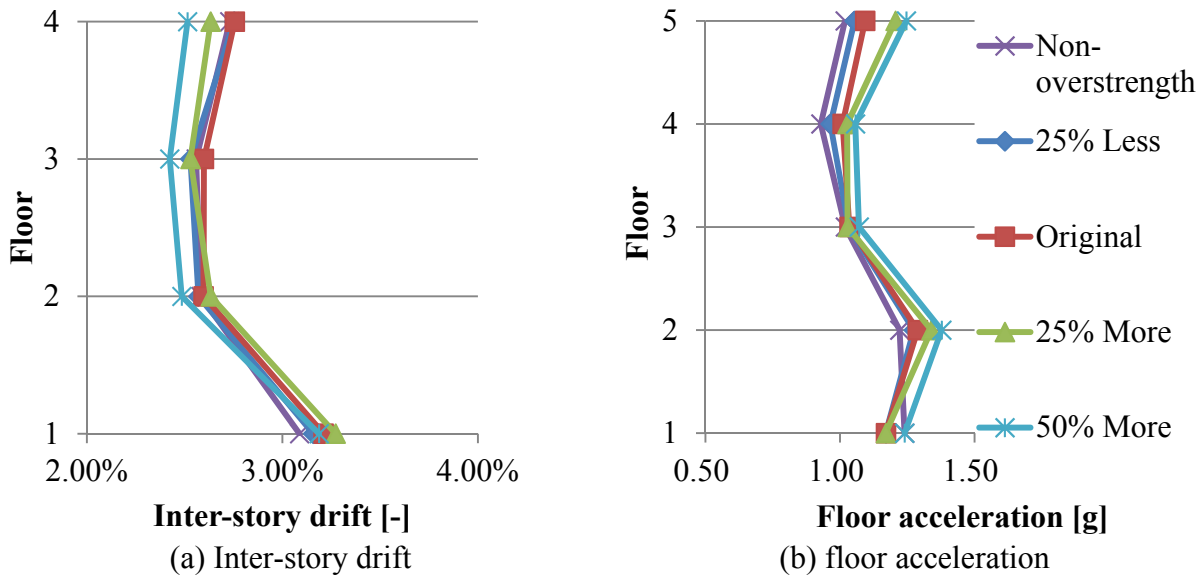

(a) Inter-story drift (b) floor acceleration

Figure 6.6 Structural response 2/50 hazard level in non-capacity design approach

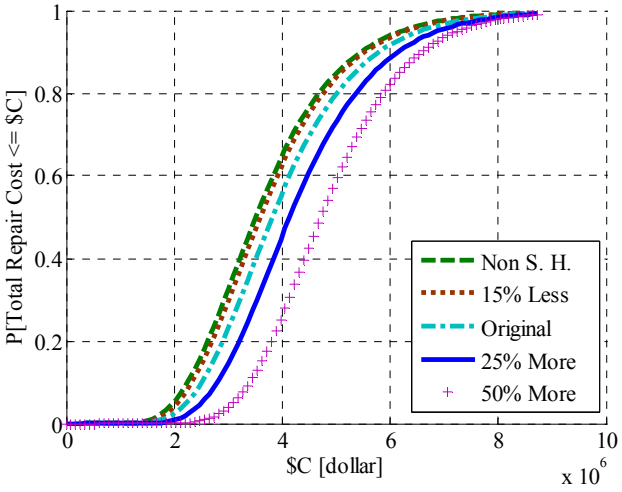

Figure 6.7 Cost CDF under 2/50 hazard in non-capacity design approach

(a) None S. H.

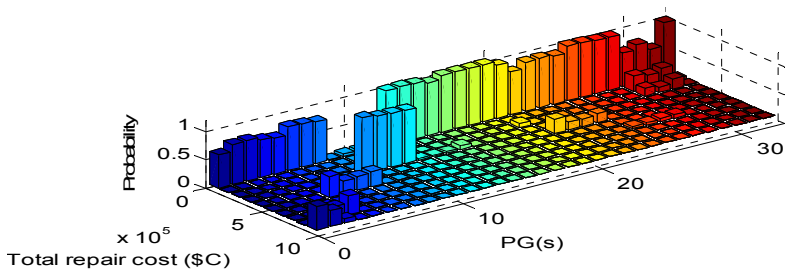

(b) 15% Less

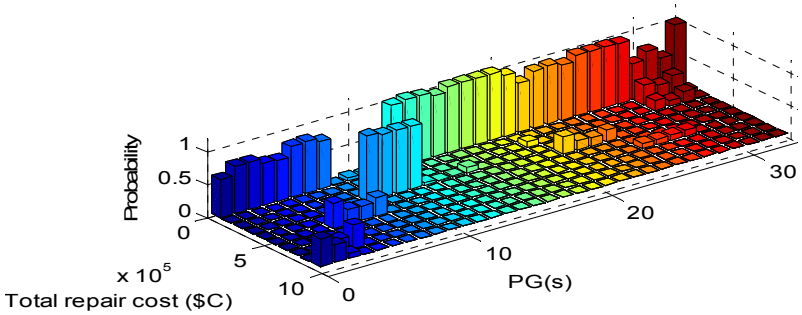

(c) Original

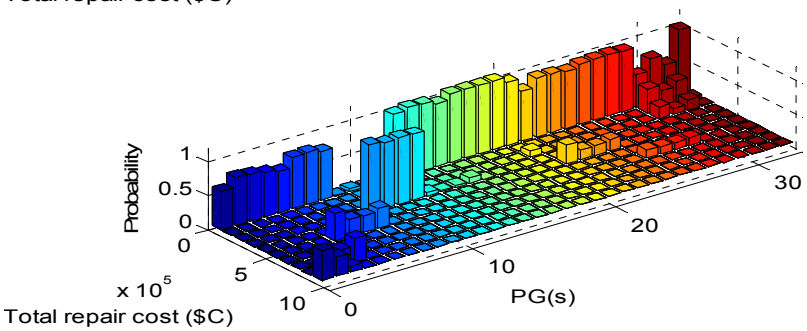

(d) 25% More

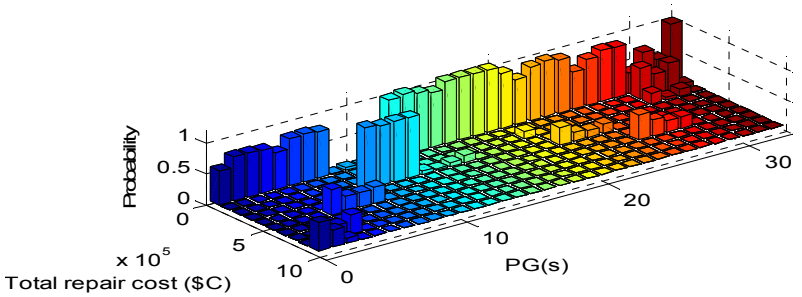

(e) 50% More

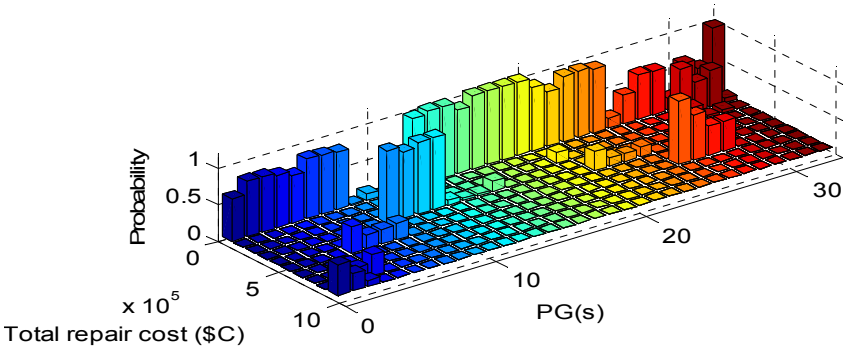

* Refer to Table 5.1 for definition of PGs

Figure 6.8 Cost distribution in non-capacity design approach

6.4 Conclusion and Design Guidelines

In this chapter, the effect of BRB overstrength to the building was studied using two approaches. The following results were observed and design guidelines were provided.

1. From the first approach, if BRBs with lower overstrength were chosen and then the non-yielding elements went through capacity design, this structure could save more initial cost than the one with higher overstrength BRBs. However, this structure had more repair cost under the MCE level earthquake than the one with higher overstrength BRBs. At the end, the sum of initial cost and repair cost became similar between structures with BRBs of higher or lower overstrength. It was suggested that the designer can use BRBs with lower overstrength to reduce the initial cost.
2. From the second approach, it was observed the impact from BRB overstrength to the inter-story drift and floor acceleration was small. However, BRBs with higher overstrength could damage more structural components which were not capacity designed. Therefore, it was suggested that capacity design in BRB structures was extremely important.

Chapter 7 Parametric Study of BRB Inclination

BRB inclination as an important parameters in the design of BRKBTMF system. Parameter study was conducted in this chapter to study the effect of BRB inclinations on the seismic performance of the BRKBTMF. The prototype building as presented in Chapter 4 was used. Dynamic analysis was conducted for the three hazard levels as presented in Chapter 4 . Detailed repair cost analysis was also conducted for the building with different BRB inclination using the performance-based evaluation framework as described in Chapter 5 .

7.1 BRB Inclination

As shown in Figure 7.1, engineer can choose any BRB inclination. In this study, the BRB inclination varied between 30˚ (most steep) to 90˚ (most horizontal). In this figure, α is the angle between BRB and column.

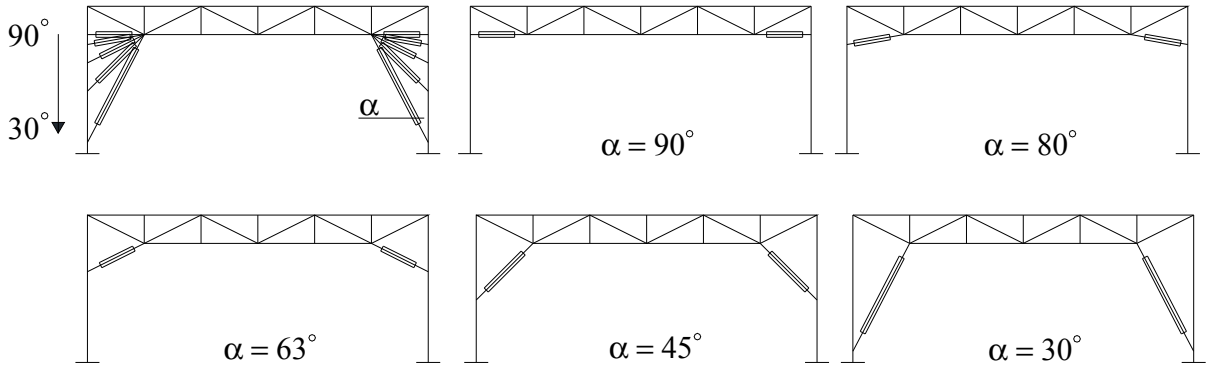

Figure 7.1 Types of BRB inclination

7.2 Design Result of Systems with Different BRB Inclinations

Table 7.1 and Table 7.2 show the comparison of the structural period and the member sizes for the different BRB inclinations considered. As shown in Table 7.1, the column and the BRB sizes increase as the angle α increases from 30˚ to 90˚. For comparison purpose, the columns of the BRKBTMF were around 135% heavier in the 90˚ inclination as compared to the 30˚ inclination. This was due to the increase in the moment demand in the columns as the angle α increased. Similarly, the demand in the BRBs increased around 120% as the angle α increased from 30˚ to 90˚. However, it should be noted that even the cross sectional area of the BRB increased as α increased, the total length reduced. This resulted to an almost neutral difference in the total use of steel material, hence resulted to no significant price difference in the BRBs. The steel truss were capacity designed, the variation in the BRB inclination did not affect the truss design. Figure 7.2 shows the initial cost breakdown for the five buildings considered. The cost increased as the BRB angle increased and it could be clearly noticed that the increasing in cost was mainly due to the increasing in the seismic columns.

Table 7.1 Summary of structural period, BRB and column sizes

BRB Angles	Period(s)	Floor	BRB Strength (kips)	Columns	
				Exterior	Interior
90˚	1.1	4	308	W24x279	W24x335
		3	463		
		2	559	W24x370	W36x328
		1	606		
80˚	1.1	4	232	W24x250	W24x306
		3	348		
		2	420	W24x335	W27x368
		1	455		
63˚	1.0	4	172	W24x207	W24x229
		3	259		
		2	312	W24x279	W24x306
		1	339		
45˚	1.1	4	145	W24x192	W24x117
		3	218		
		2	263	W24x250	W24x207
		1	285		
30˚	1.0	4	138	W24x146	W24x117
		3	208		
		2	250	W24x176	W24x131
		1	272		

Table 7.2 Summary of the truss sizes

Truss Member Sizes				
Floor	Chord	Diagonal	Vertical	Ext. Vertical
4	2MC8x18.7	2MC6x12	L3.5x3.5x5/16	2L3.5x3.5x5/16
3	2MC10x25	2MC6x15.3	L3.5x3.5x5/16	2L3.5x3.5x5/16
2	2MC10x28.5	2MC6x15.3	L3.5x3.5x5/16	2L3.5x3.5x5/16
1	2MC10x28.5	2MC8x18.7	L3.5x3.5x5/16	2L3.5x3.5x5/16

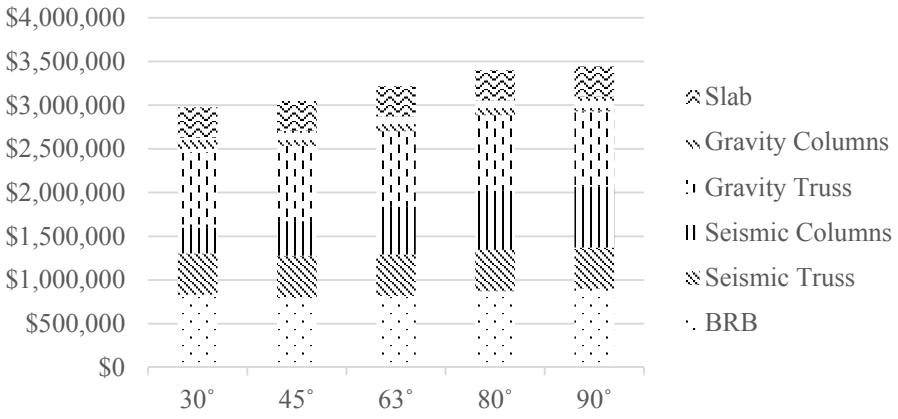

Figure 7.2 Initial cost breakdown

7.3 Nonlinear Response of the Prototype Building

Pushover analyses were conducted to determine the nonlinear response of the BRKBTMF with different BRB inclinations using the lateral forces profile shown in Chapter 2 (Equation 2.9). In order to simulate the fracture behaviors of BRBs, element removal technique presented in Chapter 3 was used.

Figure 7.3 shows the pushover analysis results. The horizontal axis represented the roof drift and the vertical axis represented base shear. The markers represented the instances when the BRBs yielded. The result showed the BRBs at the first floor yielded first followed by the BRBs at the second, third and fourth floor. It was noted that BRB yielding strain was assumed to be 0.2% in this case. The first BRB yielding occurred when the roof drift was about 0.4% for all BRB inclinations considered. The result showed that the equivalent yield drift for the BRKBTMF using bilinear behavior approximation was about 0.75% for all BRB inclinations considered, which was consistent with the yield drift reported by Wongpakdee (2011) and used in the PBPD design process. The fracture behavior of BRBs was also recorded in the pushover analysis. The distribution of BRBs fracture spread out because the lognormal distribution was used. However, the BRB fracture trend was still consistent with that the first floor BRB fractured first, followed with the second, third, and fourth floor. However, since the 45˚ and 30˚ inclinations had long braces, the strain demand was much less, and therefore, the upper floor BRBs were not fractured before 5% drift ratio. The design based shear was also shown in dash line.

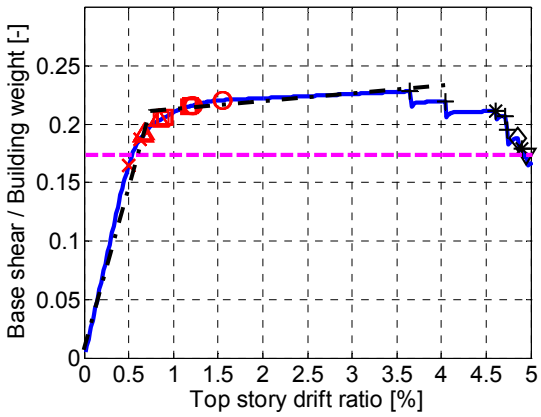

(a) 90 ˚ (θ_y = 0.75%)*

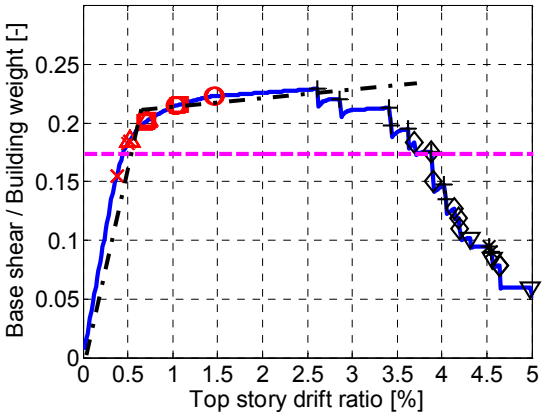

(b) 80 ˚ (θ_y = 0.70%)

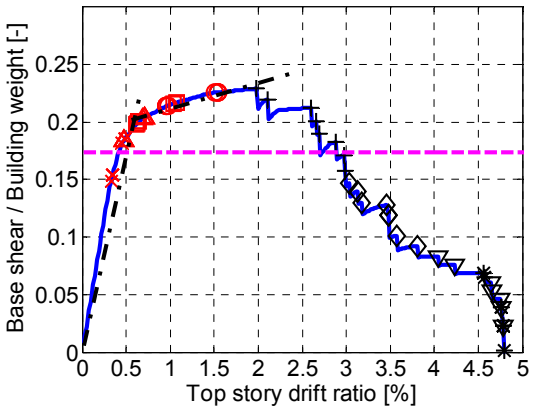

(c) 63 ˚ (θ_y = 0.65%)

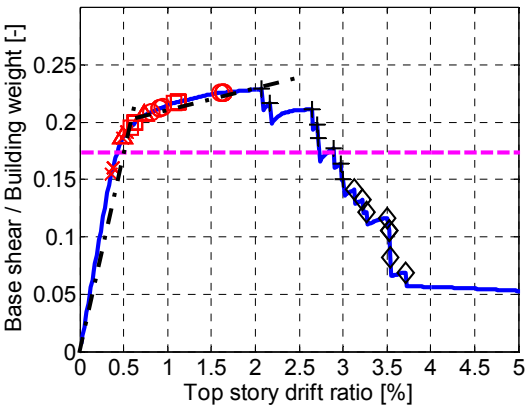

(d) 45 ˚ (θ_y = 0.63%)

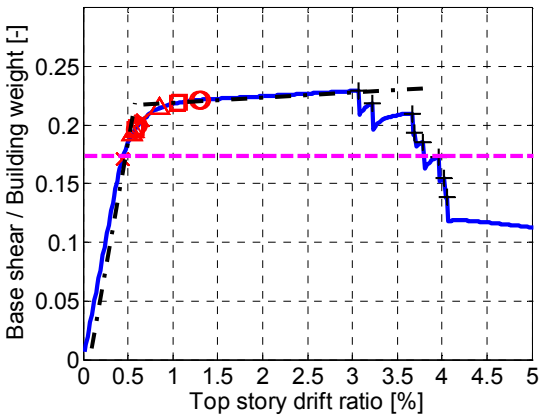

(e) 30 ˚ (θ_y = 0.60%)

*Note:
θ_y = approximate yield drift ratio;
o = yielding of the 1st story BRB;
□ = yielding of the 2nd story BRB;
Δ = yielding of the 3rd story BRB;
x = yielding of the 4th story BRB;
+ = fracture of the 1st story BRB;
◊ = fracture of the 2nd story BRB;
v = fracture of the 3rd story BRB;
***** = fracture of the 4th story BRB;
—— = the pushover curve;
- - - - = the design base shear
-·-·- = the bilinear approximation;

Figure 7.3 Pushover results of different BRB inclination

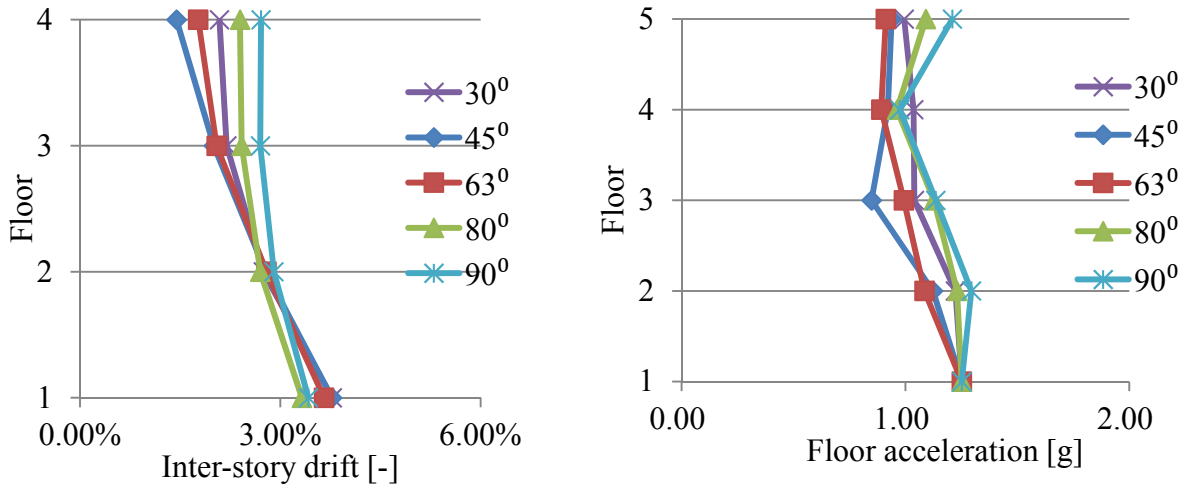

(a) 2/50 hazard level

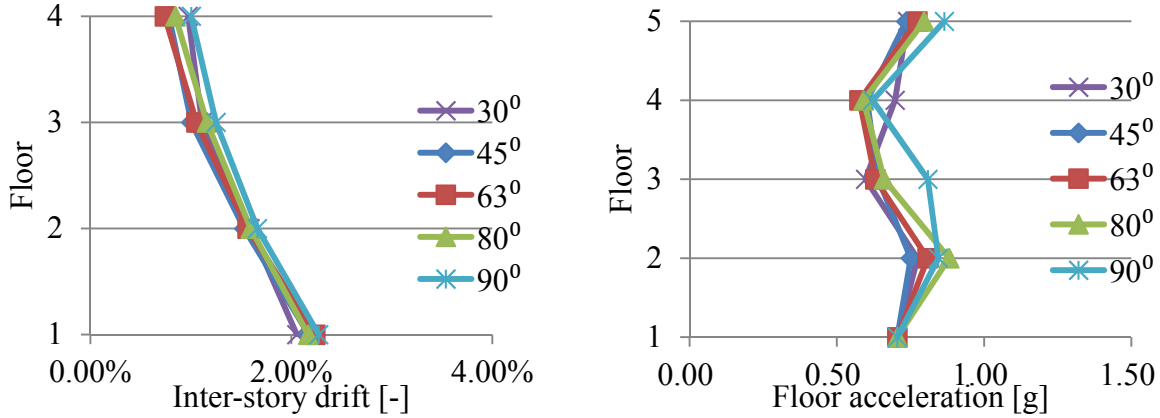

(b) 10/50 hazard level

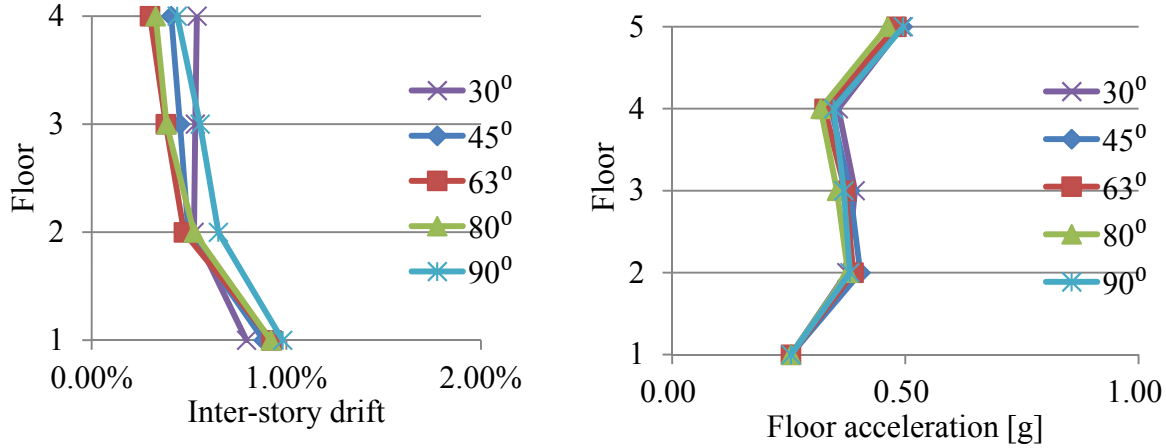

(c) 50/50 hazard level

Figure 7.4 Structural response of three hazard levels

Figure 7.4 shows the median of the peak inter-story drift ratio and peak floor acceleration for different BRB inclinations at different hazard levels. The result showed the inter-story drift ratio and peak floor acceleration were very similar among different BRB inclinations. In general, it was observed that the pin-based BRKBTMF had the highest drift and acceleration in the first floor. The peak floor acceleration and inter-story drift ratios decreased at the higher floors.

Both 63˚ and 90˚ BRKBTMF were selected to conduct incremental dynamic analysis. That was because they were the best and worst cases indicated from static and dynamic analysis. The analysis were conducted by incrementally scaling up the ground motions until the structure collapsed due to all BRBs fractured.

Figure 7.5 shows the result of the IDA response. As shown in Figure 7.5, the 63˚ BRKBTMF had more plateau than 90˚ BRKBTMF, which indicated that the 63˚ BRKBTMF was more fragile than the 90˚ BRKBTMF. Figure 7.6 shows the collapse probability curves. The result showed that the 63˚ BRKBTMF had a higher collapse probability than the 90˚ BRKBTMF. This result was consistent with the finding that 63˚ BRKBTMF has less drift tolerance.

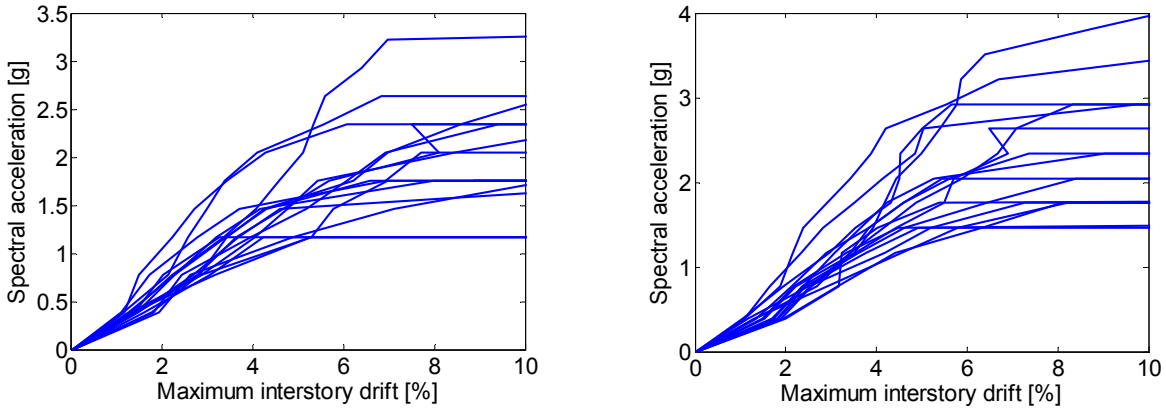

(a) 63˚ BRKBTMF (b) 90˚ BRKBTMF

Figure 7.5 IDA structural response

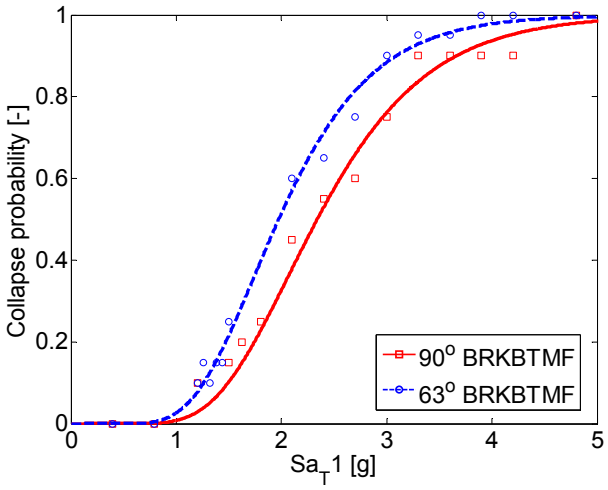

Figure 7.6 Building fragility curve for 63˚ and 90˚ BRKBTMF

7.4 Performance Evaluation with Different BRB Inclinations

Performance-based evaluation was conducted for the five BRB inclinations using the procedure outlined in Chapter 5 . Figure 7.7 show the cumulative distribution function (CDF) of the total repair cost and the repair cost breakdown for different BRB inclinations at different hazard levels. Figure 7.7 shows that both 30˚ and 90˚ BRB configuration have the least repair cost, while 45˚, 63˚ and 80˚ have higher repair cost, which is from the damage of BRB in the 2/50 hazard level. This result was consistent to the plot in Figure 2.5, in which the middle part of α angles had less drift tolerance in BRBs. Under both 10/50 and 50/50 hazard levels, only interior drift sensitive components experienced damages and required repair, and other components did not have any damage. The 30˚ and 90˚ BRB configuration behaved a little worse than the other three buildings, because they had relatively larger inter-story drift under 10/50 hazard level.

The CDF for BRKBTMF system under 2/50 hazard level showed that the maximum median (50% probability) of total repair cost was about $USD 2.8 million dollars, $USD 2.9 million dollars and $USD 3.8 million dollars for the 30˚, 90˚ and 63˚ inclinations, respectively.

This showed changing the BRB inclination made a significant difference in the median repair cost which should definitely be considered in the design process. The information presented in CDF of Figure 7.7(a) could also be used to make risk management decisions. For example, the prototype building had 60%, 58% and 25% probability that the repair cost would be less than 3 million dollars for the 30˚, 90˚ and 63˚ inclinations, respectively. This showed the 30˚ and 90˚ inclination was a more robust design as compared to the 63˚ inclination. Life cycle cost for all buildings were also computed and it is shown in Figure 7.8. The annual cost of buildings with 30˚ and 90˚ BRB inclination still had the least annual repair cost through the life cycle cost analysis.

Event	Repair cost CDF	Repair cost contribution
(a) 2/50	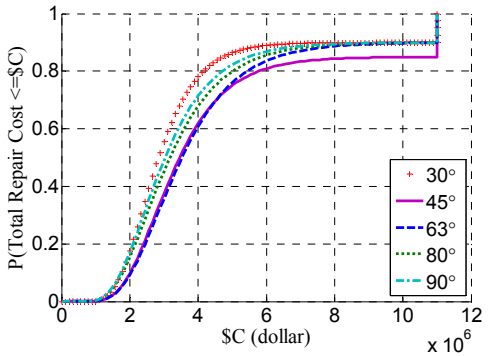	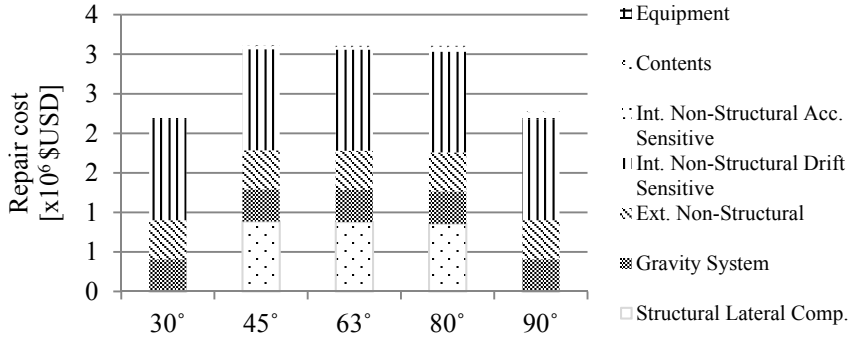
(b) 10/50	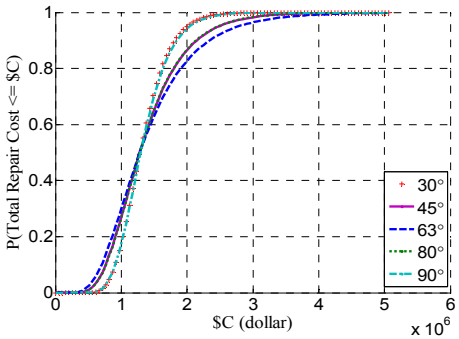	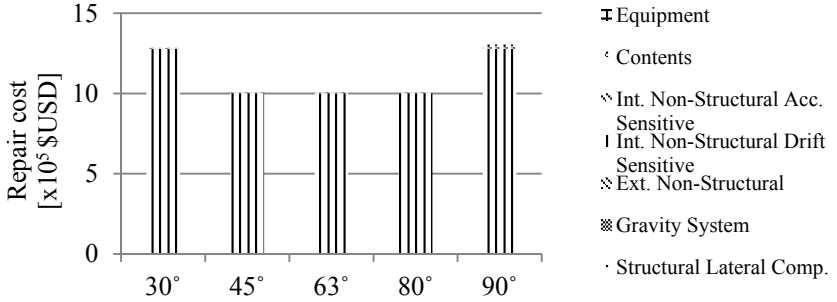
(c) 50/50	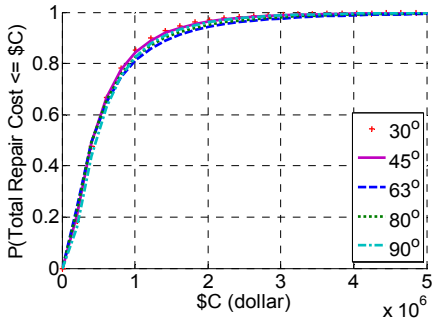	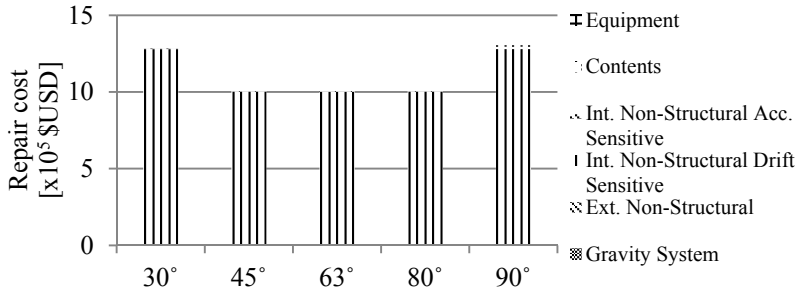

Figure 7.7 Result of repair cost simulation

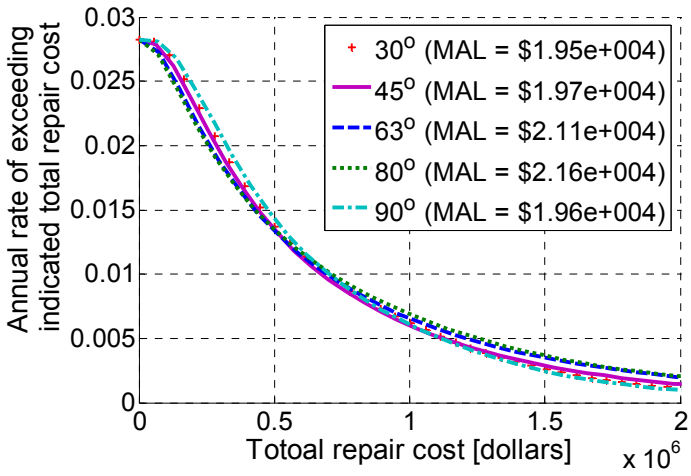

Figure 7.8 Life cycle cost for different angle configuration

The result from incremental dynamic analysis shown in Figure 7.5 and Figure 7.6 can also be used for repair cost analysis. Figure 7.9 shows the CDF of the repair costs for 63˚ and 90˚ configurations under different shaking intensities. It should be note that the total repair cost was capped at the building replacement value. Figure 7.10(a) shows the plot of normalized median repair cost of the building against spectrum acceleration. Figure 7.10(b) shows the normalized repair cost at different earthquakes return period. The results showed that the repair cost was more on the 63˚ than 90˚ BRKBTMF under the earthquake shaking with the same return period.

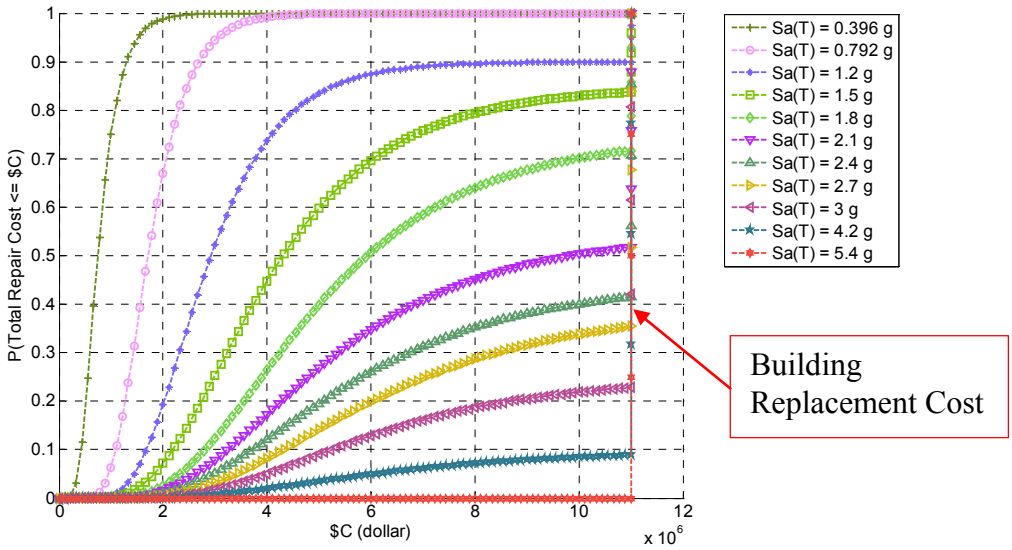

(a) 63˚ BRKBTMF

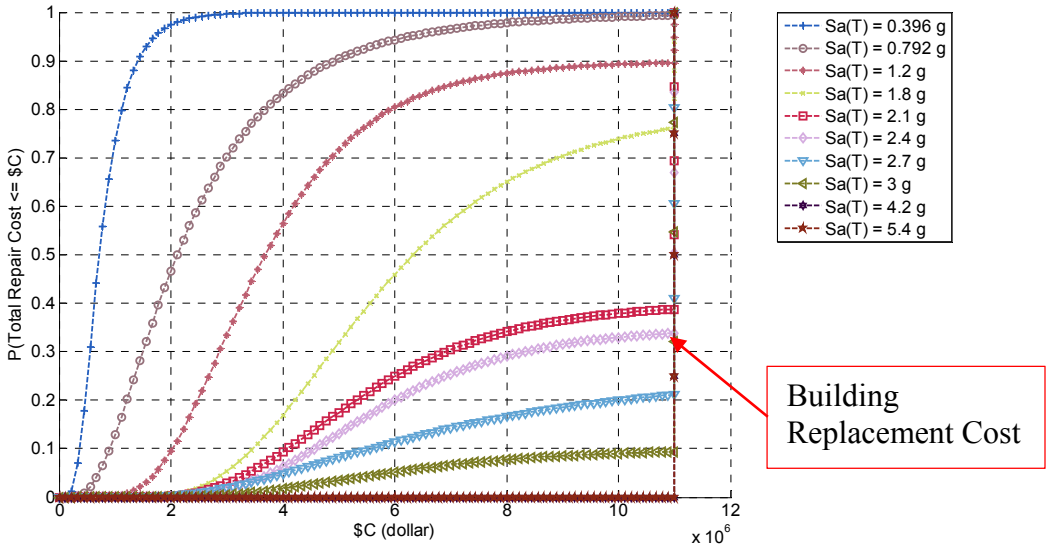

(b) 90˚ BRKBTMF

Figure 7.9 Cost CDF of incremental dynamic analysis for 63˚ and 90˚ BRKBTMF

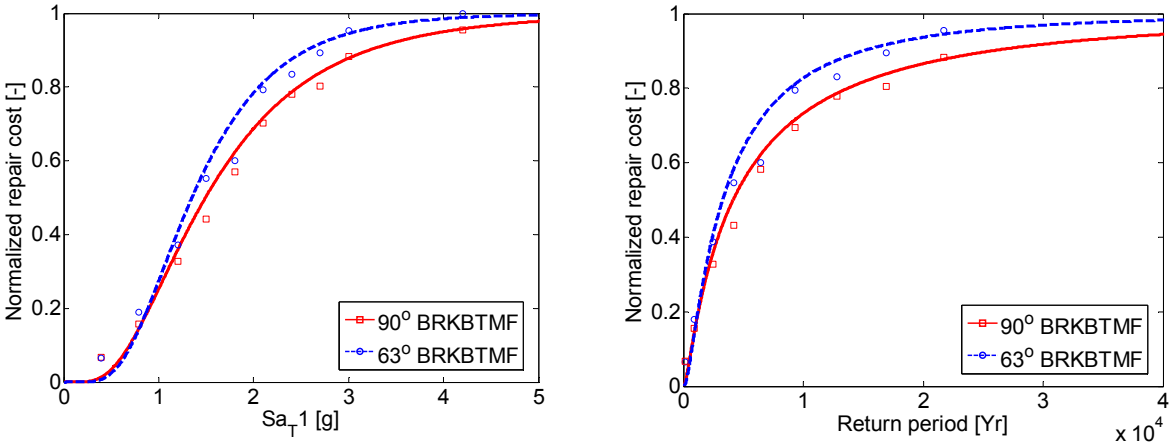

(a) Spectral acceleration to repair cost (b) Return period to repair cost

Figure 7.10 Building cost fragility curve

7.5 Conclusion and Design Guidelines

The following findings were observed from the detailed parameter study for BRB inclination. The suggestion for practicing engineers to design BRKBTMF system was also included.

1. The peak structural drift and acceleration was not significantly affected by the selection of the BRB inclination. The designers should expect that the BRKBTMF building with different BRB inclinations designed by PBPD method can reach similar performance objectives.
2. As the BRB inclination became more horizontal, the force demand to the structural columns and BRBs increased, which resulted to larger structural members, hence higher initial construction costs. On the other hand, the BRBs were able to tolerate higher drift as the BRB inclination deviated away from the 60˚ inclination, hence when the BRB inclination reached 90˚, the structure had one of the lowest repair costs. Depending on the

drift tolerance that building needs, the designer can choose the best BRB inclination to make the structural damage be the lowest. If architectural restriction was applied, the designers can follow Figure 2.5 to select BRB inclination so that the BRB would not fracture before the building reached the target performance.

3. The results showed that optimal choices of BRB inclination were either horizontal (which produced the lowest repair cost) or connecting directly to the end of the columns (which had the lowest initial cost). The designers can utilize such trends for choosing a better design for the building.

Chapter 8 Parametric Study of Truss Spans

The BRKBTMF system utilizes the advantage of steel truss to create large interior opening for the building. This is difficult to achieve by other SFRS. To compare the advantage of using BRKBTMF over conventional SFRS, the seismic performance of BRKBTMF system was compared with the traditional moment frame (MF) system with different spans.

8.1 Description of Long Span Prototype Building

The prototype building has been described in Chapter 4 . In this chapter, the seismic system of East-West direction was designed. As shown in Figure 8.1(a), the E-W direction can be divided into three different bays with bay width of 30 ft., 45 ft., and 60 ft. The 30 ft. span was typical for office building, and 60 ft. span was suitable for lecture hall or meeting room. The building height was modified for the structures with different spans in order to keep the same clear height among different systems as shown in Figure 8.1(a). Other geometric parameters of buildings were summarized in Table 8.1 and the definition of these parameter can be referred to Chapter 2 .

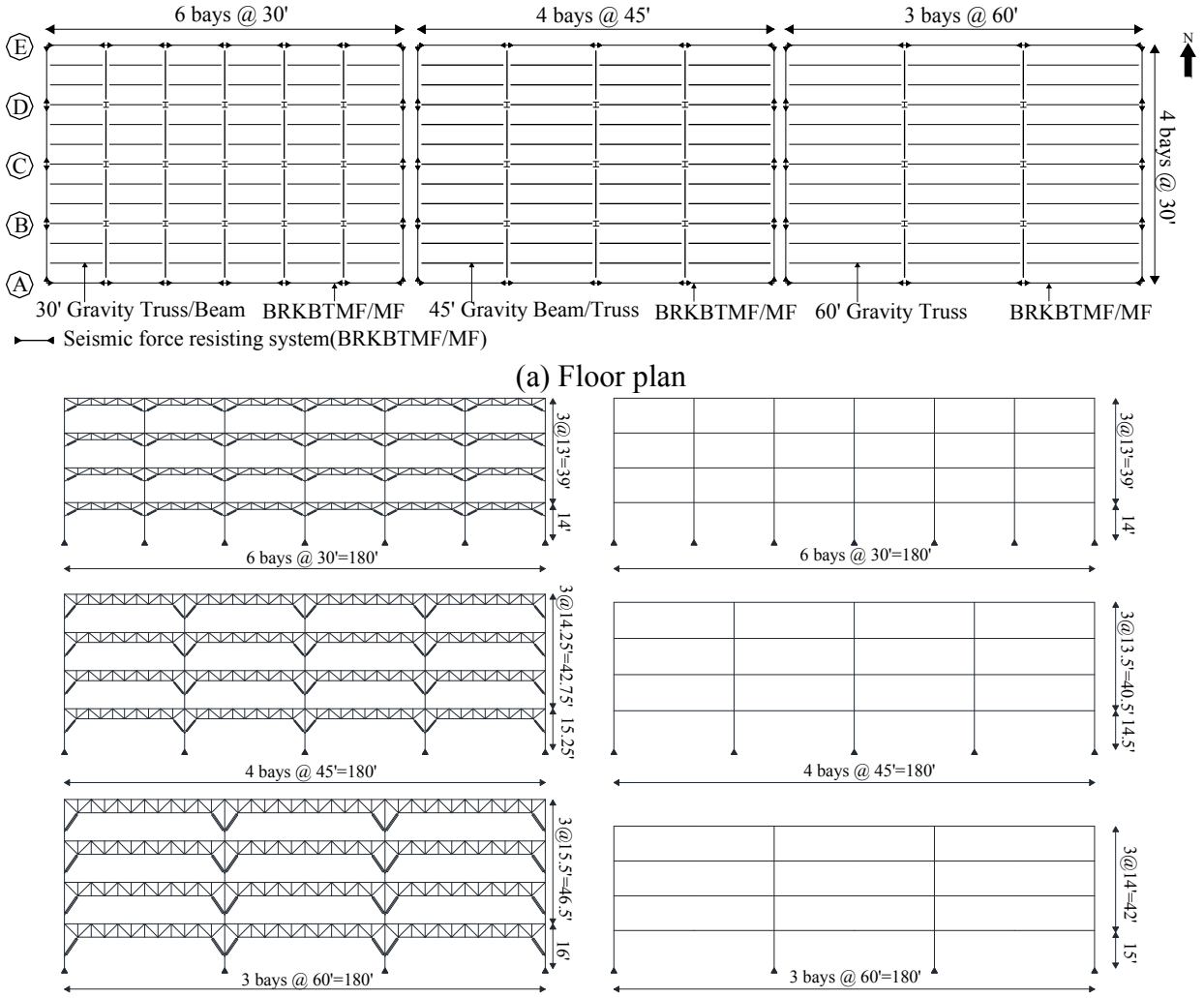

Figure 8.1 Building dimensions for BRKBTMF and MF

Table 8.1 Design geometrical parameters for the buildings

Configuration	Span No.	Bay Width	Max Truss/Beam Depth, D_0	BRB Depth, D	Dist. Btw. Vertical Chord, l_1
30 ft. BRKBTMF	6	30 ft.	2.50 ft.	5.00 ft.	5.00 ft.
45ft. BRKBTMF	4	45 ft.	3.75 ft.	9.10 ft	4.50 ft.
60 ft. BRKBTMF	3	60 ft.	5.00 ft.	10.00 ft	5.00 ft.
30 ft. MF	6	30 ft.	2.50 ft.	-	-
45ft. MF	4	45 ft.	3.00 ft.	-	-
60 ft. MF	3	60 ft.	3.50 ft.	-	-

8.2 Structural Design

Following the PBPD design procedure as outlined in Chapter 2 , the member sizes of BRKBTMF were designed. Similarly the member sizes of MF system were designed following similar PBPD approach outlined in Goel and Chao (2008). During the design, the gravity system for 30 ft. MF and 45 ft. MF used regular beam section except 60 ft. MF, while all BRKBTMF used truss system. The 60 ft. MF used truss system to reduce the material cost for long span. The member sizes are shown in Table 8.2. Figure 8.2 shows the comparison of initial construction between BRKBTMF and MF with different spans. It was observed the cost of gravity system occupied one half of the building total initial cost in MF system, while BRKBTMF could take advantage of the light weight truss and save more cost. The cost of seismic system of BRKBTMF did not vary too much with changing span, while the cost of seismic system of MF system was very sensitive to span. As the building spanned longer and longer, the advantages of BRKBTMF could be easily observed.

Table 8.2 Summary of member sizes

Type	Seismic Columns						Gravity Columns (BRKBTMF / MF)		
	30 ft. BRKBTMF		45 ft. BRKBTMF		60 ft. BRKBTMF		30 ft.	45 ft.	60 ft.
Floor	Exterior	Interior	Exterior	Interior	Exterior	Interior			
4	W33X141	W36X160	W40X149	W40X167	W30X191	W40X199	W12X40	W12X53	W12X65
3	W33X141	W36X160	W40X149	W40X167	W30X191	W40X199	W12X40	W12X53	W12X65
2	W30X191	W40X199	W40X199	W40X199	W36X230	W40X277	W12X65	W14X90	W14X132
1	W30X191	W40X199	W40X199	W40X199	W36X230	W40X277	W12X65	W14X90	W14X132
Type	Seismic Columns						Seismic Beams		
	30 ft. MF		45 ft. MF		60 ft. MF		30 ft. MF	45 ft. MF	60 ft. MF
Floor	Exterior	Interior	Exterior	Interior	Exterior	Interior			
4	W33X130	W40X183	W40X167	W40X249	W40X199	W44X335	W24X68	W27X94	W30X116
3	W33X130	W40X183	W40X167	W40X249	W40X199	W44X335	W27X84	W33X118	W40X149
2	W30X191	W44X230	W36X230	W44X335	W40X277	W40X503	W30X99	W36X135	W40X167
1	W30X191	W44X230	W36X230	W44X335	W40X277	W40X503	W30X108	W36X135	W40X183
Type	30 ft. BRKBTMF Seismic Truss			45 ft. BRKBTMF Seismic Truss			60 ft. BRKBTMF Seismic Truss		
Floor	Chord	Diagonal	Vertical	Chord	Diagonal	Vertical	Chord	Diagonal	Vertical
4	2MC6X12	2MC6X6.5	L3.5X3.5X 5/16	2MC6x12	2MC6x6.5	L3.5X3.5X5 /16	2MC6x15.1	2MC6x12	L3.5X3.5X 5/16
3	2MC6X16.3	2MC8X8.5		2MC6x18	2MC8x8.5		2MC7x19.1	2MC6x12	
2	2MC7X19.1	2MC6X12		2MC7x22.7	2MC6x12		2MC8x22.8	2MC6x15.1	
1	2MC8X22.8	2MC6X12		2MC9x25.4	2MC6x12		2MC10x28.5	2MC6x15.3	
Type	30 ft. BRKBTMF Gravity Truss			45 ft. BRKBTMF Gravity Truss			60 ft. BRKBTMF Gravity Truss		
Dir.	Chord	Diagonal	Vertical	Chord	Diagonal	Vertical	Chord	Diagonal	Vertical
E-W	2L2.5X2.5X1/ 4	2L2X2X3/1 6	L2X2X1/8	2L3X3X7/16X 3/4	2L2.5X2.5X1/ 4X3/4	L2X2X1/8	2L3X3X7/16X 3/4	2L2.5X2.5X 1/4X3/4	L2X2X1/8
N-S	2L5X5X3/8X 3/4	2L3.5X3.5 X5/16X3/4	L2X2X3/16	2L6X6X5/8	2L6X6X3/8	L2X2X3/16	2L6X6X5/8	2L6X6X3/8	L2X2X3/16
Type	Gravity Beam		60 ft. MF Gravity Truss			BRB Sizes/ Floor.	30 ft. BRKBTMF	45 ft. BRKBTMF	60 ft. BRKBTMF
Dir.	30 ft. MF	45 ft. MF	Chord	Diagonal	Vertical	4	123	154	188
E-W	W21X44	W24X84	2L2.5X2.5 X1/4	2L2X2X3/16	L2X2X1/8	3	188	235	287
N-S	W27X84	W30X99	2L5X5X3/8 X3/4	2L3.5X3.5X5/ 16X3/4	L2X2X3/16	2	229	286	349
Note	Fy(Beam/Truss/BRB) = 50 ksi; Fy(Column) = 55 ksi					1	249	312	380

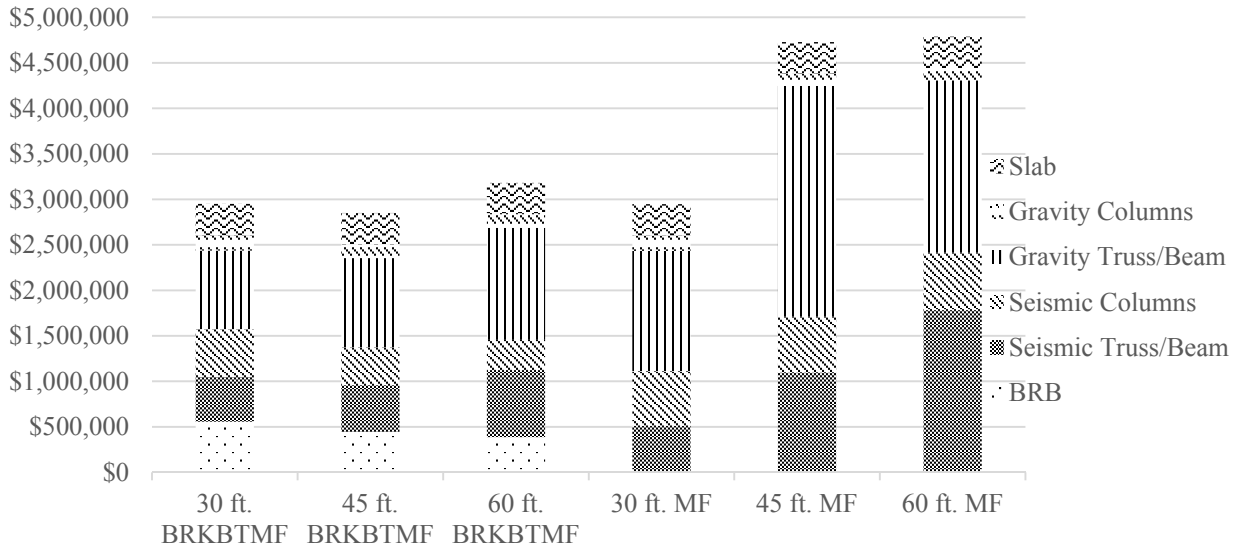

Figure 8.2 Cost breakdown for initial structural cost

8.3 Structural Response of Systems with Different Spans

Pushover analyses were conducted to determine the nonlinear response of the BRKBTMF and MF with different spans using the lateral force profile proposed by Chao et al. (2007). Figure 8.3 shows the pushover analysis results. The horizontal axis represented the roof drift ratio and the vertical axis represented the normalized base shear with respect to the building weight (8631 kips). The different markers represented the instances when the BRBs and moment connections yielded or fractured. In general, the yielding for both systems started at the first floor then progresses to the higher floors. It should be noted that because the stiffness between the bays was different, the BRBs and moment connections at the same level did not all yield at the same time, though they were very close. The pushover curve can be approximated using a tri-linear curve: 1) Elastic, where the force-deformation response increased linearly from origin to the yield strength; 2) Strength hardening, where the force-deformation response increased linearly from yield strength to ultimate strength; 3) Softening, where force-deformation response decreased linearly from ultimate strength

to zero capacity. Yield drift was defined when the deformation reached the yield strength. In this study, the yield roof drift ranged from 0.60% to 0.65% and 1.0 % to 1.25% for the BRKBTMF and MF, respectively. This finding was very comparable to the results reported by Wongpakdee et al. (2012, 2014) and Goel and Chao (2008). The strength hardening factor, Ω was defined as the ratio of ultimate strength over the yield strength. In this study, BRKBTMF had the strength hardening factor around 1.2 and MF had strength hardening factors varying from 1.2 to 1.6. Ductility was defined as the ratio of deformation at 80% of the ultimate strength at the softening range of the structure to the yield deformation. The results showed that the ductility ranged from 4.0 to 5.4 and 3.0 to 3.3 for the BRKBTMF and MF, respectively. Overall, the BRKBTMF had higher stiffness in the elastic range, but lower stiffness in the strength hardening range as compared to the MF. Both systems had similar stiffness in the softening range.

Nonlinear dynamic responses were obtained using the ground motions described in Chapter 4 . Figure 8.4 and Figure 8.5 show the median peak floor acceleration and inter-story drift ratios, respectively, under the three hazard levels considered. It can be seen that the BRKBTMF had lower inter-story drift ratios as compared to MF for all hazards and span ratios considered. The peak floor acceleration was very similar between the MF and the BRKBTMF. At the lower shaking intensities (50/50), the MF had slightly lower peak floor acceleration than the BRKBTMF. That was because the BRKBTMF had higher initial stiffness as compared to the MF. At the higher shaking intensities (2/50), the BRKBTMF had lower peak floor acceleration than the MF, particularly at the roof level.

Incremental dynamic analyses (IDA) were conducted to identify the median shaking intensity at incipience of collapse. Figure 8.6 shows the results of IDA response. Each curve represented the relationship between the spectral acceleration of an individual ground motion at

the fundamental period of the structure and the maximum inter-story drifts. The results showed that the median IDA curves for the MF and BRKBTMF were very similar for the three span lengths. In general, the median IDA curve of BRKBTMF had higher probability against collapse compared to the MF system.

Figure 8.7 shows collapse probability vs. the spectral acceleration at the fundamental period of the structure. The result showed BRKBTMF had lower probability of collapse as compared to the MF. For example, when the spectral acceleration at the fundamental period of the structure equaled to 2.0 g, the 60 ft. MF had a collapse probability of 0.8, while the 60 ft. BRKBTMF had a collapse probability of 0.4. One can also use the collapse margin ratio (CMR), which was defined as the ratio of the spectral acceleration at the 50% collapse probability to the spectral acceleration of the MCE shaking at the fundamental period of the structure, to quantify the capacity of the structure against collapse. Both BRKBTMF and MF had CMR ranging from 1.4 to 1.7. In general, BRKBTMF had higher or equal CMR than the MF for all span lengths considered.

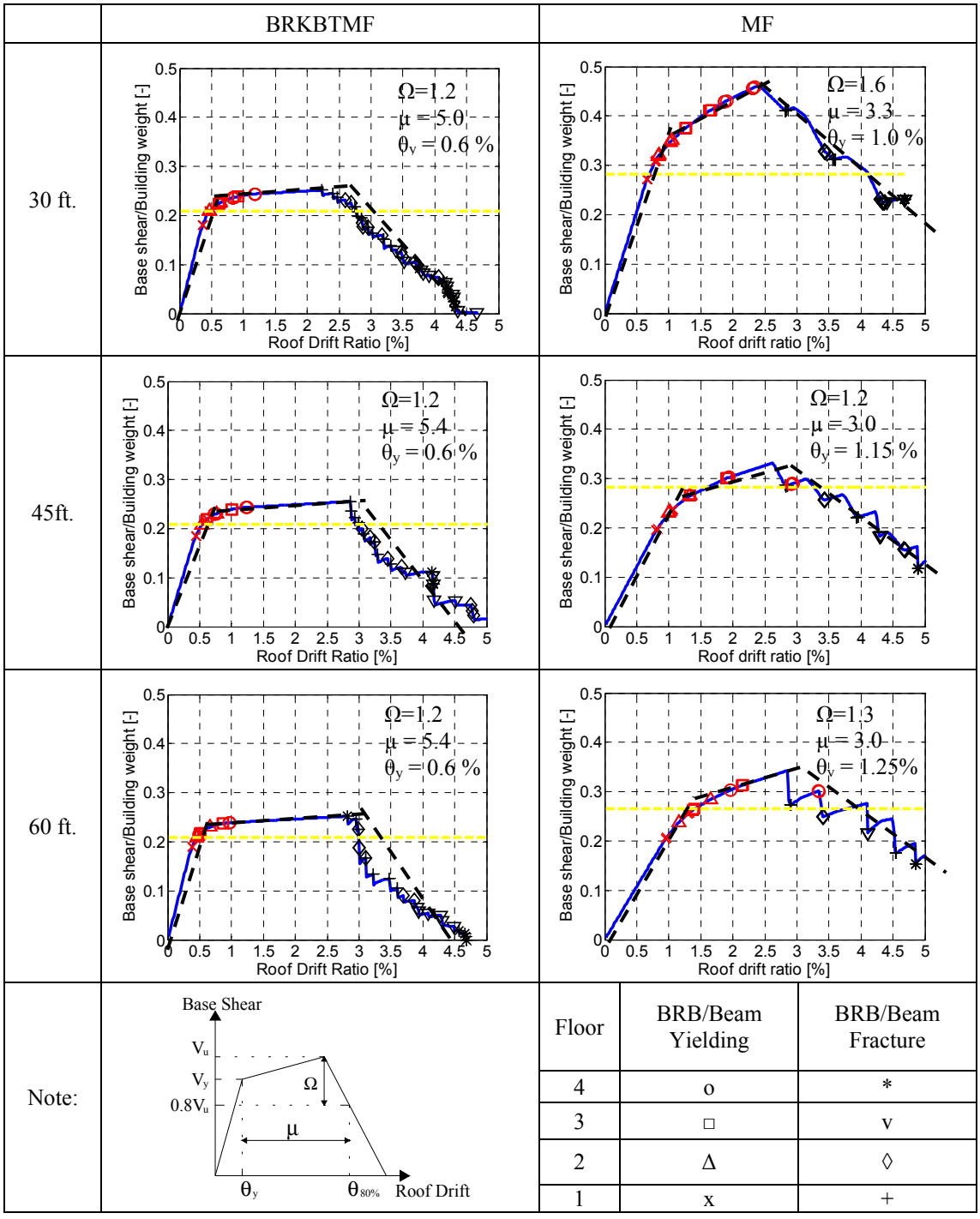

Figure 8.3 Summary of pushover analyses

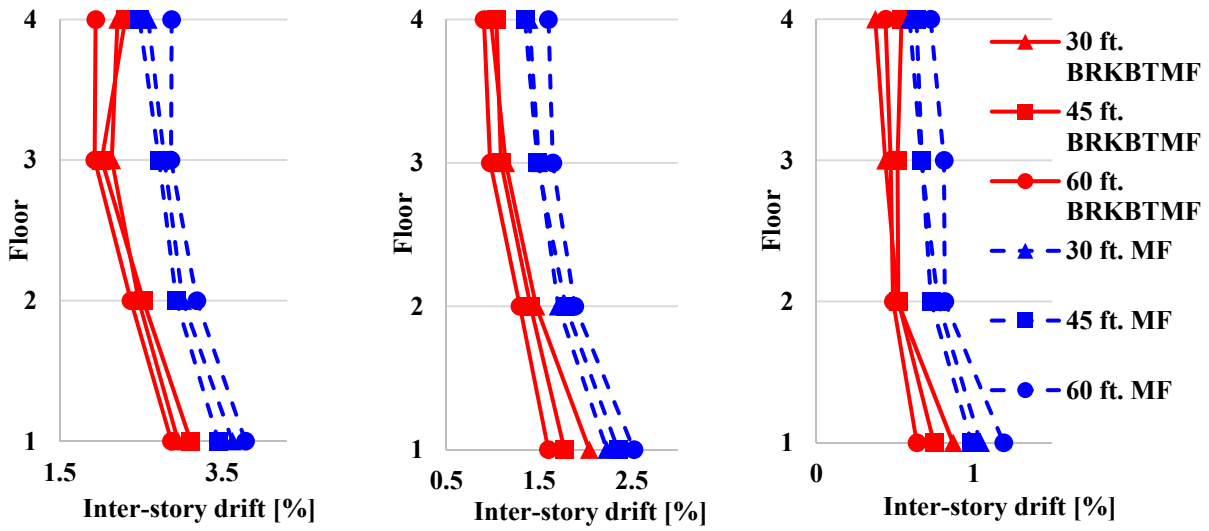

(a) 2/50 hazard level (b) 10/50 hazard level (c) 50/50 hazard level

Figure 8.4 Median of the peak inter-story drift ratio for three hazards

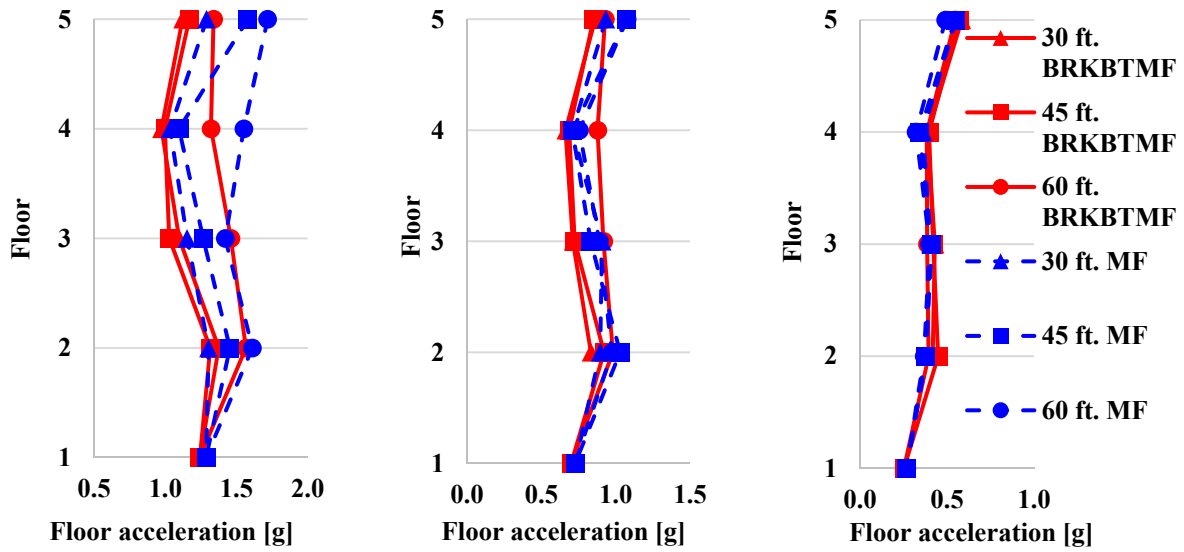

(a) 2/ 50 hazard level (b) 10/50 hazard level (c) 50/50 hazard level

Figure 8.5 Median of the peak floor acceleration

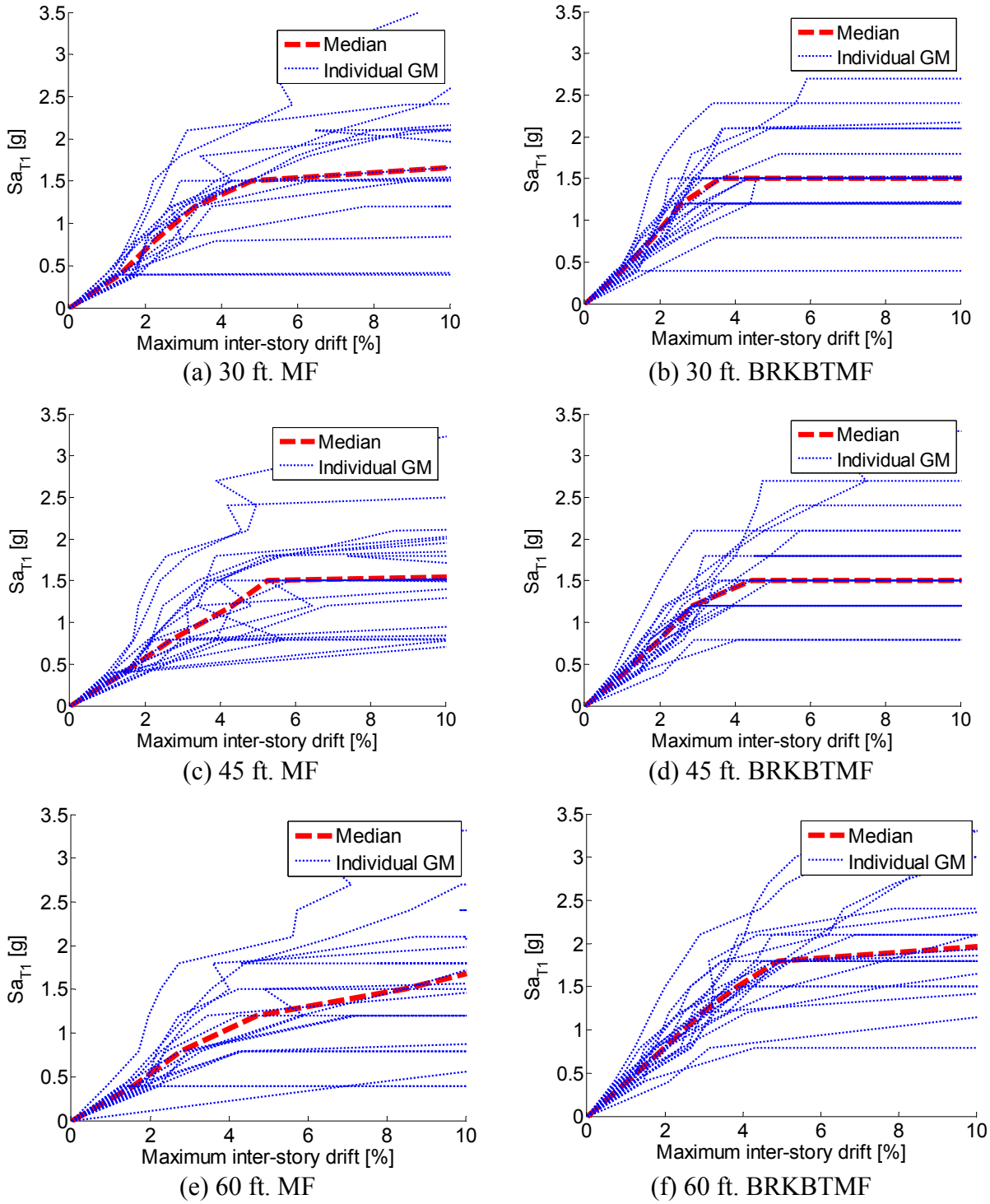

Figure 8.6 IDA response of both BRKBTMF and MF

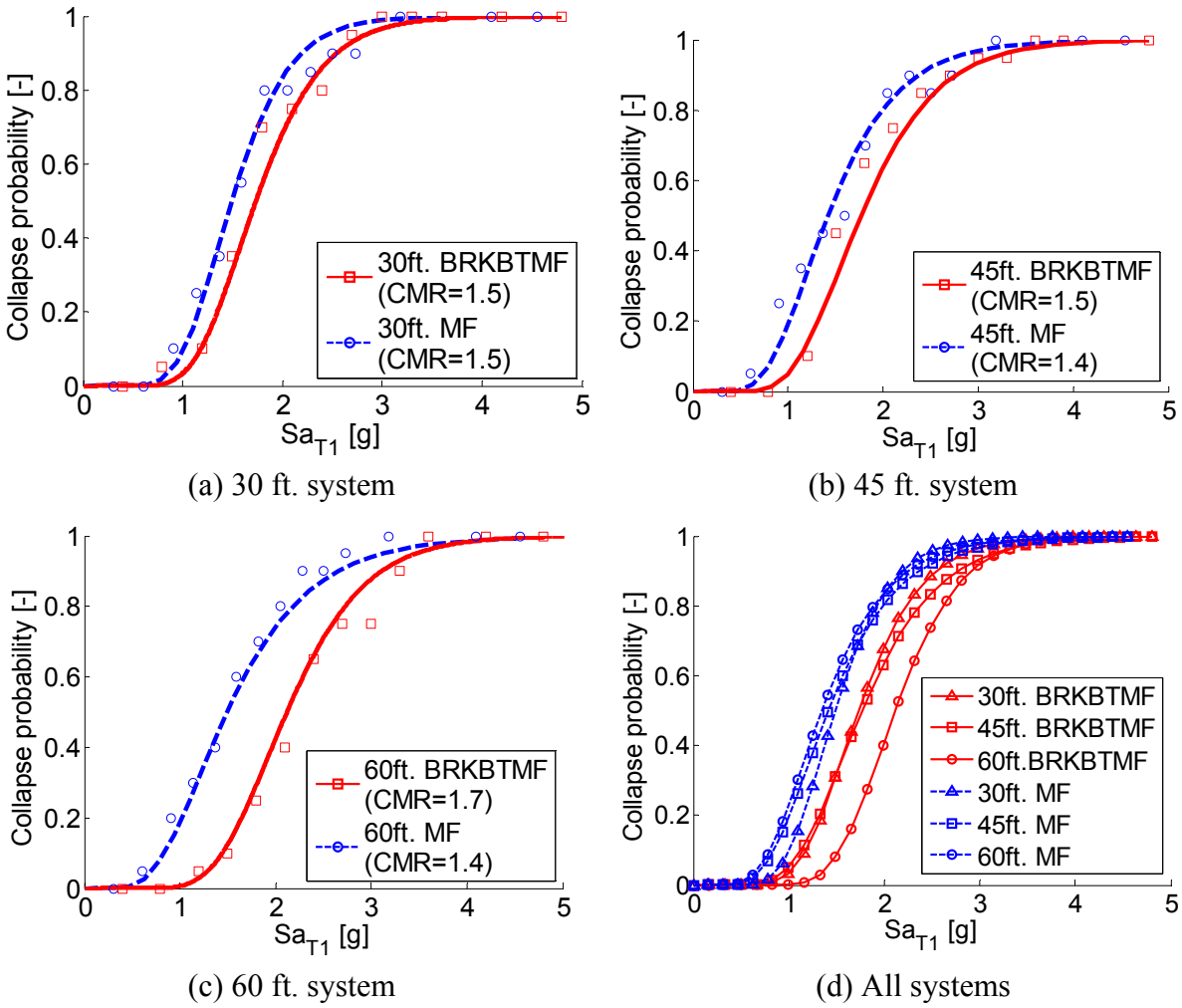

(a) 30 ft. system (b) 45 ft. system

(c) 60 ft. system (d) All systems

Figure 8.7 Collapse fragility curves

8.4 Performance-Based Evaluation for BRKBTMF and MF System

Figure 8.8 to Figure 8.10 show cost distribution of the total repair cost and Figure 8.11(a), (b) and (c) show the cumulative distribution function (CDF) under the 2/50, 10/50, 50/50 hazard levels for the 6 different structural configurations included in this study, respectively. The vertical axis represented the probability of repair cost exceeding the threshold value shown in the horizontal axis. For example, by comparing the 45 ft. MF and 45 ft. BRKBTMF (Figure 8.11(a)), the structure had 50% and 80% probability that the total repair cost was less than $USD 6 million

dollars for the MF and BRKBTMF system, respectively. This showed that BRKBTMF was more robust to limit the total repair costs. It should be noted that the total repair cost presented in Figure 8.11(a) also includes the probability of collapse. When structural collapse occurred, the repair cost was calculated by summing the replacement cost for all components in the building. The vertical lines at the end of CDF represent the probability of structural collapse. For example, at 2/50 hazard level (Figure 8.11(a)), the 60 ft. BRKBTMF had 10% probability of collapse. Different structural systems had different replacement values, hence the cutoff replacement value may not be the same for all systems. At the 2/50 hazard level, the 60 ft. BRKBTMF had the least repair cost, while the 60 ft. MF had the largest repair cost. The 45 ft. and 30 ft. MF had the second and third largest repair cost, followed by 30 ft., 45 ft. and 60 ft. BRKBTMF. Figure 8.8 shows a summary of the cost breakdown for both systems at 2/50 hazard level. The results showed that the MF and BRKBTMF experienced similar damages in the interior drift sensitive (PG 9 -12) PG. However, the MF experienced higher damages in the structural (PG 1- 4), exterior drift sensitive (PG 5-8), acceleration sensitive (PG 13-21) and gravity (PG 22-25) PGs. More comparison of repair cost between BRKBTMF and MF is shown in Figure 8.9 and Figure 8.10 for 10/50 and 50/50 hazard levels, respectively. In general, the MF had higher repair cost compared to the BRKBTMF. In addition, the repair cost for the MF increased as the span increased, while such trend was not observed in the BRKBTMF. Following the similar approach, the repair time for different structures can be calculated and the results in Figure 8.12 shows that BRKBTMF required less time to recover from the earthquake of 2/50 hazard level.

The repair cost information can be further represented by computing the annual rate of total repair cost exceeding a threshold value. Such annualized loss was obtained by multiplying the slope of the hazard curve with the complementary cumulative distribution function (CDF) of the

repair cost, and then integrated across the range of shaking intensities included in this study. Figure 8.11(d) shows the annualized loss curves for the six different structural configurations included in this study. The vertical axis represented annual rate that the repair cost exceeded the threshold value presented in the horizontal axis. The result showed that the MF has higher annual probability of exceeding a fix amount of repair cost as compared to the BRKBTMF. For example, the MF had 1% annual probability of exceeding $USD1 million dollars, while the BRKBTMF only had 0.25% annual probability of exceeding the same amount.

The area under the loss curve in Figure 8.11(d) shows the mean annualized total repair loss (MAL). Owners can use this information to quantify the mean annual repair costs for each structural system. In this study, the owner would need to pay $USD 9,000 annually for the 60 ft. BRKBTMF, while the need for the 60 ft. MF configuration was $USD 20,000 annually. This again showed that the BRKBTMF was superior to the MF in terms of life cycle repair costs.

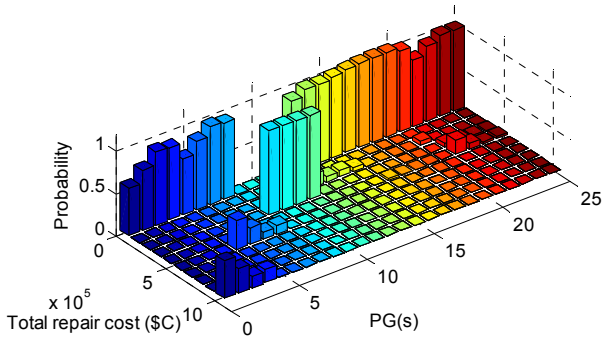

(a) 60 ft. BRKBTMF

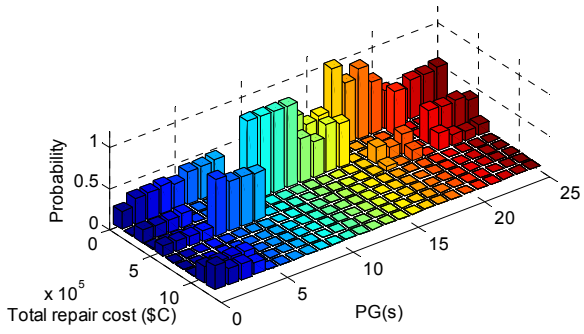

(b) 60 ft. MF

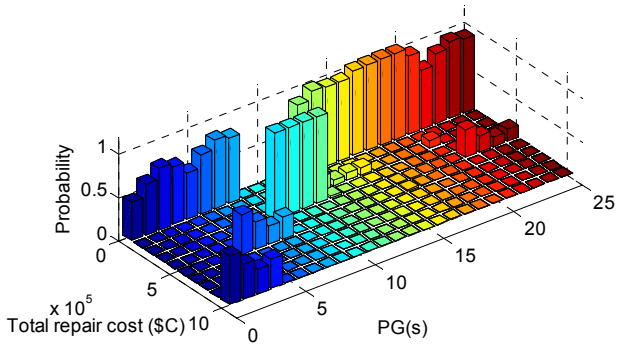

(c) 45 ft. BRKBTMF

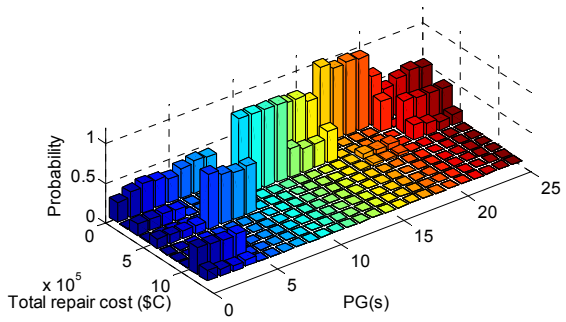

(d) 45 ft. MF

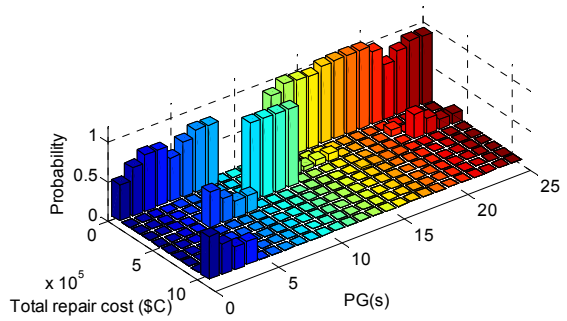

(e) 30 ft. BRKBTMF

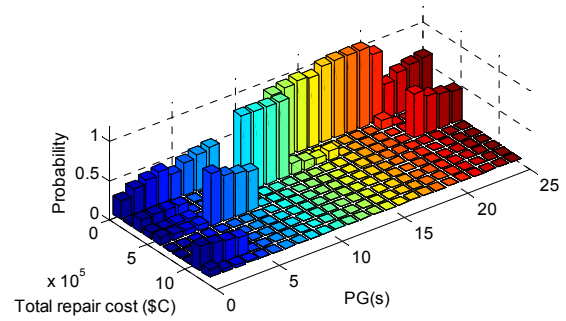

(f) 30 ft. MF

Figure 8.8 Cost distribution under 2/50 hazard level

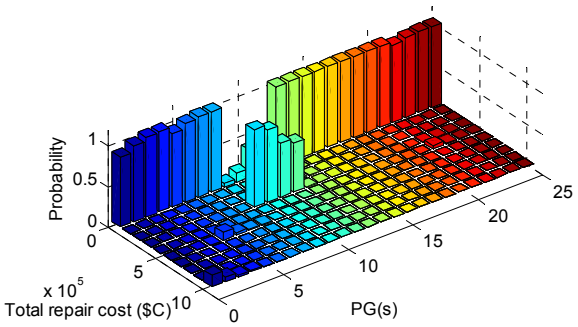

(a) 60ft. BRKBTMF

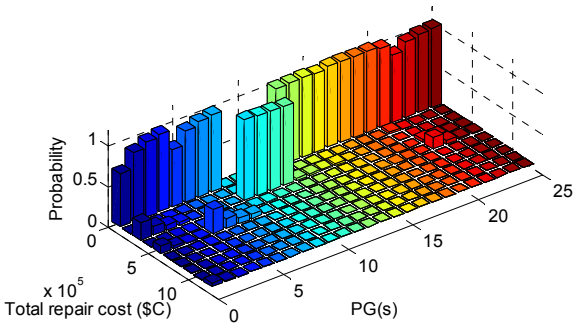

(b) 60ft. MF

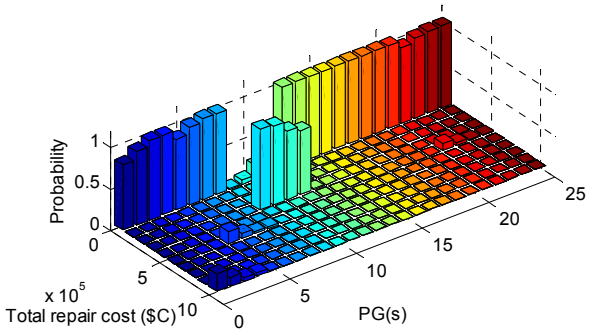

(c) 45 ft. BRKBTMF

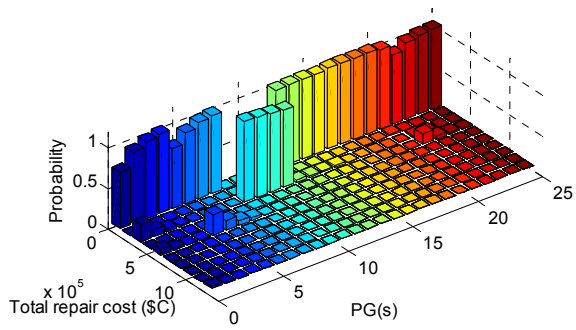

(d) 45 ft. MF

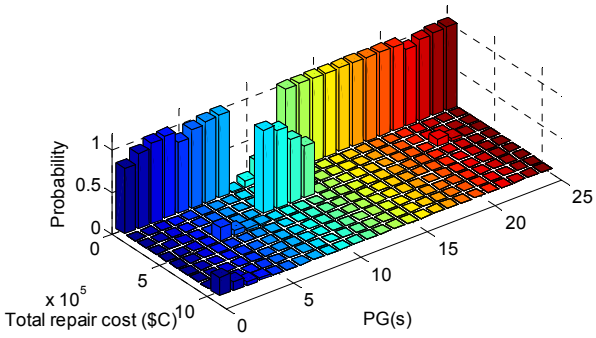

(e) 30 ft. BRKBTMF

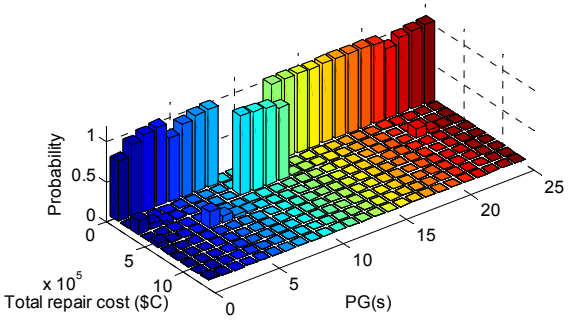

(f) 30 ft. MF

Figure 8.9 Cost distribution under 10/50 hazard level

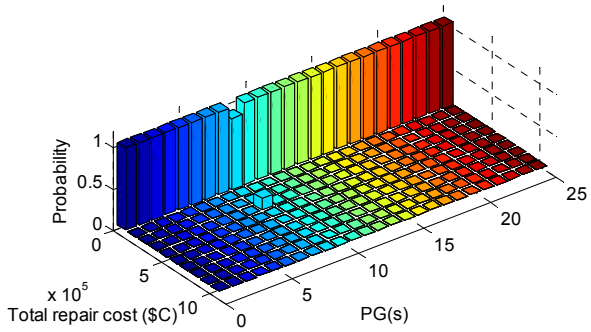

(a) 60 ft. BRKBTMF

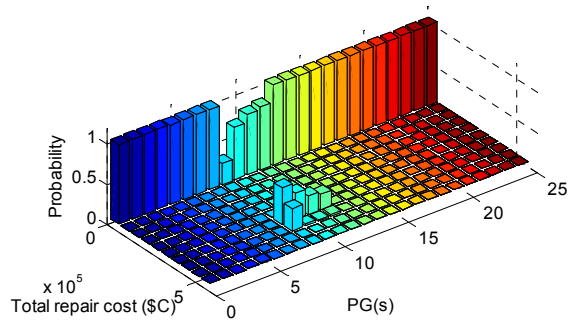

(b) 60 ft. MF

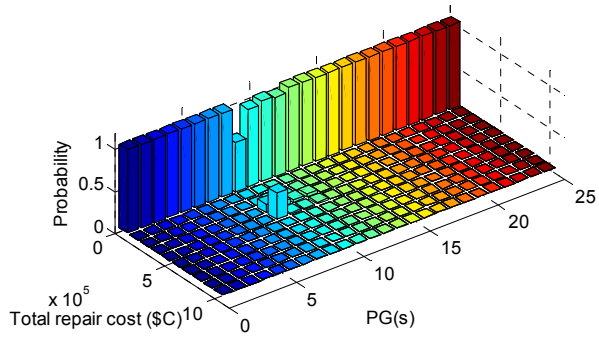

(c) 45 ft. BRKBTMF

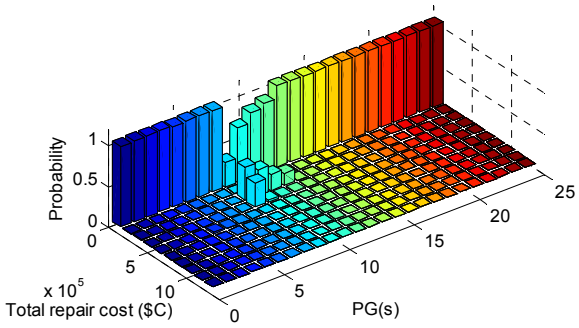

(d) 45 ft. MF

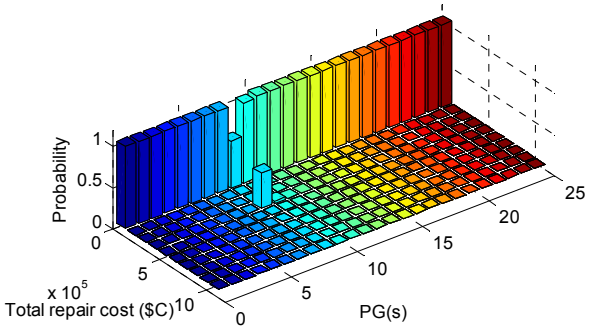

(e) 30 ft. BRKBTMF

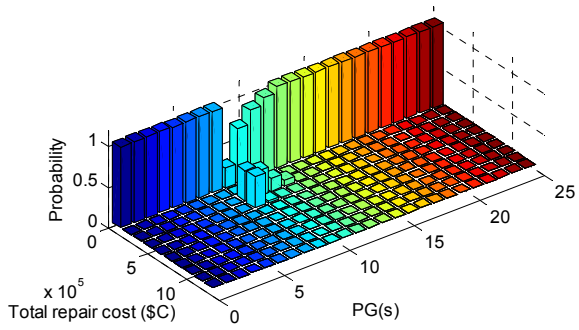

(f) 30 ft. MF

Figure 8.10 Cost distribution under 50/50 hazard level

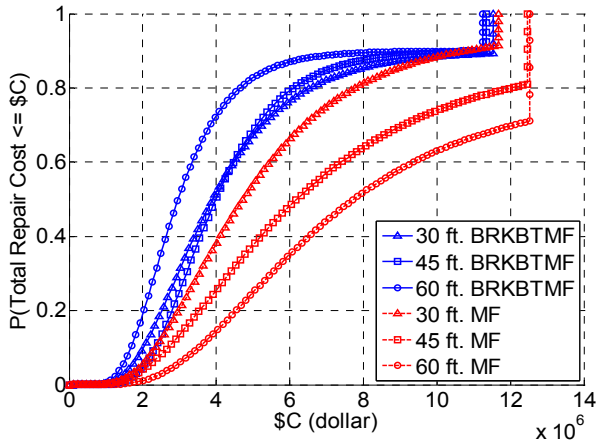

(a) 2/50 hazard level

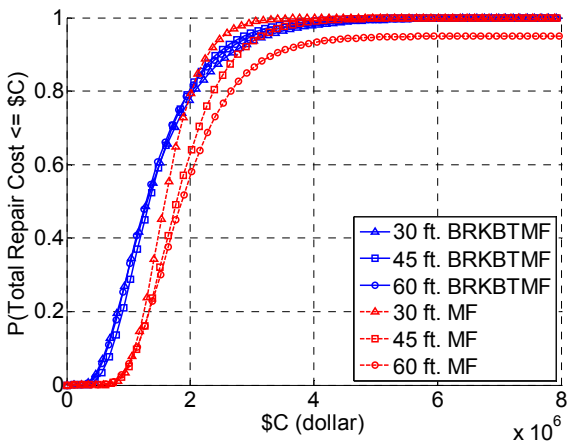

(b) 10/50 hazard level

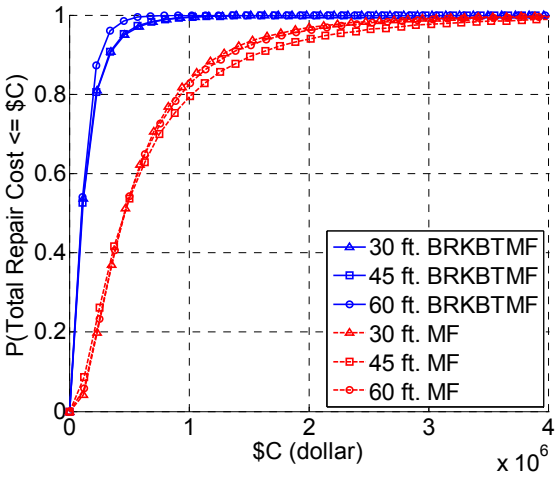

(c) 50/50 hazard level

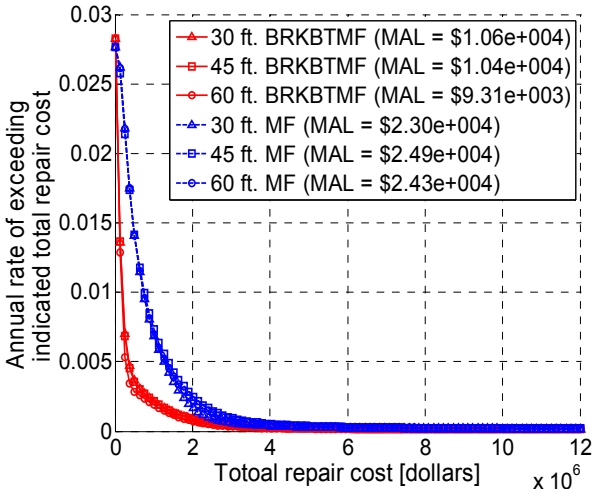

(d) Annual loss

Figure 8.11 Cumulative distribution function at all hazards and annual loss of repair cost

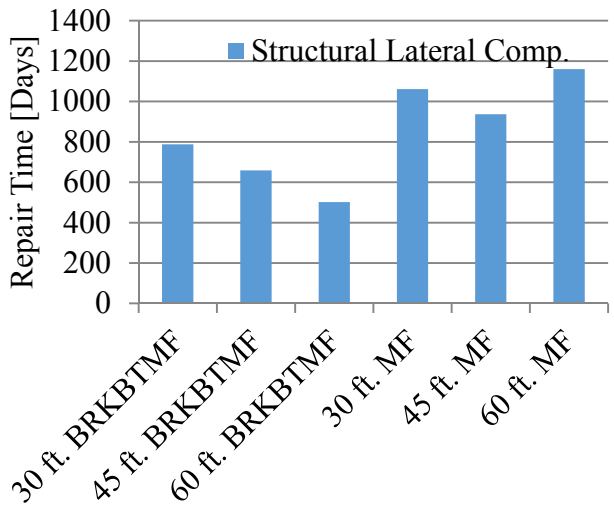

Figure 8.12 Repair time of structural components for 2/50 hazard level

8.5 Conclusion and Design Guidelines

Buckling restrained knee braced truss moment frame (BRKBTMF) is a newly developed steel structural system that utilizes open web truss girders and buckling restrained knee braces to create structural configuration with large interior spacing. The use of the designated energy dissipation devices allows the system to be used efficiently and effectively for seismic applications. In this paper, a prototype building located in Berkeley, California, was designed using both the BRKBTMF and conventional MF with solid web beams. The seismic performance of the BRKBTMF and MF, in terms of initial construction costs, life cycle repair costs, and probability of collapse was systematically studied using the state-of-the-art research tools. The results showed that BRKBTMF used less structural material, especially for long span lengths, yet it can achieve higher seismic performance by limiting the structural damage, repair cost and probability of collapse. The following specific observations were derived from the study of analysis results.

1. The initial costs and repair cost of MF with conventional solid web beams increased significantly as span lengths became larger. On other hand, the initial cost and performance of the BRKBTMF were not affected by the span lengths. Hence, it was recommended to use BRKBTMF for long span frames.
2. The BRKBTMF required lighter gravity load carrying system as compared MF. Therefore, utilization of light weight trusses was an efficient and cost effective way to span larger bay lengths.
3. Structural fuses such as BRBs can be more easily replaced after severe earthquake, which allowed the structure to recover from earthquake more efficiently. This made BRKBTMF system more attractive for seismic application.

Chapter 9 Summary and Conclusion

9.1 Conclusion

Buckling restrained knee braced truss moment frame (BRKBTMF) is a novel steel structural system that utilizes advantage of steel trusses and buckling restrained braces to create large interior spacing with designated energy dissipation devices for seismic applications. This thesis utilized OpenSees to develop a finite element model for BRKBTMF system. In order to model the system realistically, the original Steel02 material was improved to include the behavior of tension and compression strength asymmetry. The numerical result was calibrated against available experimental data and good matching was observed. In addition, a new modeling technique involving element removal was implemented to model the sudden fractures of the BRBs and the force redistribution within the systems. Since BRKBTMF system was a newly proposed system, no code design procedure was available. Therefore, this thesis utilized the performance-based plastic design procedure to design this novel structural system. A prototype office building located at Berkley, California was redesigned using the BRKBTMF system. The building had a floor plan of 120 ft. by 180 ft. and height of 53 ft. (14 ft. on the first floor and 13 ft. for the rest of the floors). A clear floor height was kept at least 10.5 ft. A site specific hazard analysis was conducted for the prototype building. Ground motions were selected from the PEER NGA database (PEER, 2010) and amplitude scaled to match target spectrum. A state-of-the-art performance-based earthquake engineering (PBEE) procedure was used to quantify the performance of the BRKBTMF. Major findings were outlined below:

1. PBPD was an efficient and effective way to design BRKBTMF.
2. BRKBTMF performed as intended, where the BRBs were the elements expected to yield during the strong earthquake shaking, while the rest of the structural were capacity protected. This made the system very robust and resilient towards future earthquakes.
3. Overstrength factors of BRBs did not significantly affect the global structural performance of the building. Selecting the BRB with lower overstrength factor resulted to lower initial construction cost. Hence, it was suggested that BRBs with lower overstrength factor shall be used.
4. Designers shall make sure that the non-yielding elements were capacity designed based on the BRB overstrength to limit unexpected structural damage and post-earthquake financial losses.
5. Peak structural drift and acceleration were not significantly affected by the selection of the BRB inclination. However, as the BRB inclination became more horizontal, the force demand to the structural columns and BRBs increased. This resulted in larger structural members, hence higher initial construction cost. On the other hand, the BRBs were able to tolerate higher drift as the BRB inclination deviated away from the 60˚ inclination. Hence when the BRB inclination reached 90˚ or 30˚, the structure had one of the lowest repair costs. Designer can utilize Figure 2.5 to select the most optimal BRB inclination.
6. BRKBTMF was very efficient to span long distance yet still maintained excellent seismic performance. The study found that the seismic performance of BRKBTMF system were not affected significantly by the span.

9.2 Future Work

Although this thesis has studied BRKBTMF system thoroughly through advanced finite element modelling, further experimental tests are required to validate the system. The remaining questions on BRKBTMF is summarized herein.

1. The top chord is usually welded to the column which creates semi-rigid connection, the effect from the semi-rigid connections compared to pin connection needs to be studied experimentally.
2. The top chord of the steel truss is expected to form plastic hinge at the connection to the column. Typically such elements are required to be compact. However, it is unclear if the requirement for the top chord of the steel truss to be compact is necessary. This effect will be studied experimentally.
3. The hysteresis behavior of BRB largely depends on the loading history. Whether it will affect the component design and the building performance should be validated through experiment.

Currently, large-scale subassemblage tests are being planned at University of British Columbia, Vancouver (UBC) as part of an international collaborative research project. The findings form these studies will provide more in-depth understanding of the seismic design and system behavior of BRKBTMF.

Bibliography

AISC. (2010a). *Seismic Provisions for Structural Steel Buildings, American Institute of Steel Construction, ANSI/AISC 341-10*. Chicago, IL, USA.

AISC. (2010b). *Specification for Structural Steel Building*. American Institute of Steel Construction. ANSI/AISC 360-10, Chicago.

Applied Technology Council 58. (2008). *Development of Next-Generation Performance-Based Seismic Design Procedures for New and Existing Buildings*. Applied Technology Council, https://www.atcouncil.org/projects-sp-1235934887/project-atc58 (10/09/2013) .

ASCE. (2010). *Minimum Design Loads for Buildings and Other Structures. SEI/ASCE 7-10*. Reston, Va.

Black, C. J., Asce, M., Makris, N., & Aiken, I. D. (2004). Component Testing , Seismic Evaluation and Characterization of Buckling-Restrained Braces. *Journal of Structural Engineering*, (June), 880–894.

Chao, S. H., & Goel, S. C. (2006a). A Seismic Design Method for Steel Concentric Braced Frames for Enhanced Performance. In *Proceedings, 4th International Conference on Earthquake Engineering*. Taipei, Taiwan.

Chao, S. H., & Goel, S. C. (2006b). Performance-Based Seismic Design of Eccentrically Braced Frames Using Target Drift and Yield Mechanism as Performance Criteria. *AISC Engineering Journal*, *43*(3), 173–200.

Chao, S. H., & Goel, S. C. (2008). Performance-Based Plastic Design of Special Truss Moment Frames. *AISC - Engineering Journal*, *45*(2), 127–150.

Chao, S. H., Goel, S. C., & Lee, S. S. (2007). A Seismic Design Lateral Force Distribution Based on Inelastic State of Structures. *Earthquake Spectra*, *23*(3), 547–569. Retrieved from http://earthquakespectra.org/doi/abs/10.1193/1.2753549

Clark, P., Aiken, I., & Ko, E. (1999). Design Procedures for Buildings Incorporating Hysteretic Damping Devices.

Cornell, C. (1968). Engineering Seismic Risk Analysis. *Bulletin of the Seismological Society of America*, *58*(5), 1583–1606.

Eguchi, R., Elwood, K., & Lee, E. K. et. al. (2012). *The 2010 Canterbury and The 2011 Christchurch New Zealand Earthquake and The 2011 Tohoku Japan Earthquake: Emerging Reasearch Needs and Opportunities Workshop Report*.

FEMA-355C. (2000). *State of the Art Report on Systems Performance of Steel Moment Frames Subject to Earthquake Ground Shaking*. Federal Emergency Management Agency, Washington:, D.C.

Filippou, F. C., Popov, E. P., & Bertero, V. V. (1983). *Effects of Bond Deterioration on Hysteretic Behavior of Reinforced Concrete Joints*. Report EERC 83-19, Earthquake Engineering Research Center, University of California, Berkeley.

Giuffre, A., & Pinto, P. (1970). Reinforced Concrete Behavior under Strong Repeated Loadings. *Giornale Del Genio Civile*, *5*, 391–408.

Goel, S. C., & Chao, S. H. (2008). *Performance-Based Plastic Design: Earthquake-Resistant Steel Structures*. International Code Council, USA.

Goel, S. C., & Itani, A. M. (1994). Seismic-Resistant Special Truss Moment Frames. *Journal of Structural Engineering*, *120*(6), 1781–1797.

Goel, S. C., & Leelataviwat, S. (1998). Seismic Design by Plastic Method. *Engineering Structures*, *20*(4-6), 465–471. Retrieved from http://linkinghub.elsevier.com/retrieve/pii/S0141029697001478

Iwata, M., & Murai, M. (2006). Buckling-Restrained Brace Using Steel Mortar Planks ; Performance Evaluation as A Hysteretic Damper. *Earthquake Engineering and Structural Dynamics*, (July), 1807–1826.

Kim, J., & Choi, H. (2005). Response Modification Factors of Dhevron-Braced Frames. *Engineering Structures*, *27*(2), 285–300. Retrieved from http://linkinghub.elsevier.com/retrieve/pii/S0141029604003402

Lee, C. H., Jung, J. H., Oh, M. H., & Koo, E. S. (2003). Cyclic Seismic Testing of Steel Moment Connections Reinforced with Welded Straight Haunch. *Engineering Structures*, *25*(14), 1743–1753. Retrieved from http://linkinghub.elsevier.com/retrieve/pii/S0141029603001767

Lee, S. S. (2002). *Performance-Based Design of Steel Moment Frames Using Target Drift and Yield Mechanism*. Ph.D. Thesis, Dept. of Civil Engineering, University of Michigan.

Leelataviwat, S., Goel, S. C., Rai, D., & Yang, T. Y. et al. (2012). A Collaborative Research Program on Performance-Based Eesign of Innovative Structural Systems for Earthquake

Resistance: An Overview. In *15th World Conference of Earthquake Engineering*. Lisbon, Portugal.

Leelataviwat, S., Goel, S. C., & Stojadinovic´, B. (1999). Toward Performance-Based Seismic Design of Structures. *Earthquake Spectra*, *15*(3), 435–461.

Lignos, D. G., Asce, A. M., Krawinkler, H., & Asce, M. (2013). Development and Utilization of Structural Component Databases for Performance-Based Earthquake Engineering. *Journal of Structural Engineering*, (August), 1382–1394.

López, W. A., & Sabelli, R. (2004). *Seismic Design of Buckling-restrained Braced Frames*. *Steel Tips, Structural Steel Educational Council*. Moraga, CA, U.S.A.

Macrae, G. A., Kimura, Y., & Roeder, C. (2004). Effect of Column Stiffness on Braced Frame Seismic Behavior. *Journal of Structural Engineering*, (March), 381–391.

Merritt, S., Uang, C. M., & Benzoni, G. (2003a). *Subassemblage Testing of CoreBrace Buckling Resitrained Brace*. in Report No. TR-2003/01, University of California, San Diego, La Jolla.

Merritt, S., Uang, C. M., & Benzoni, G. (2003b). *Subassemblage testing of star seismic bucklingrestrained braces*. Report No. TR-2003/04, University of California, San Diego, La Jolla, CA.

Miranda, E., & Bertero, V. V. (1994). Evaluation of Strength Reduction Factors for Earthquake-Resistant Design. *Earthquake Spectra*, *10*(2), 357–379.

NBCC. (2010). *National Building Code of Canada, 12th ed., 2005 Nationa National Research Council of Canada (NRCC)*. Ottawa.

Newmark, N. M., & Hall, W. J. (1982). *Earthquake Spectra and Design*. EI Cerrito, CA: Earthquake Engineering Research Institute.

PEER. (2000). Open System for Earthquake Engineering Simulation (OpenSees). Pacific Earthquake Engineering Research Center, University of California, Berkeley, CA.

PEER. (2010). PEER Strong Motion Database. *University of California at Berkeley*. Retrieved from http://peer.berkeley.edu/peer_ground_motion_database

Popov, E. P., & Engelhart, M. D. (1988). Seismic Eccentrically Braced Frames. *Journal of Constructional Steel Research*, *10*, 321–354.

Structural Engineers Association of California (SEAOC), Applied Technology Council (ATC), C. of U. for R. in E. E. (CUREE). (2011). *SAC Steel Project Database*. Network for Earthquake Engineering Simulation (database).

Tremblay, R., & Robert, N. (2006). Seismic Performance of Low- and Medium- Rise Chevron Braced Steel Frames. *Canadian Journal of Civil Engineering*, *28*(4), 699–714. Retrieved from http://www.nrc.ca/cgi-bin/cisti/journals/rp/rp2_abst_e?cjce_l01-038_28_ns_nf_cjce28-01

Tsai, K. C., & Popov, E. P. (1991). Cyclic Behavior of End-Plate Moment Connections. *Journal of Structural Engineering*, *116*(11), 2917–2930.

Uang, B. C., Yu, Q. K., Member, S., Noel, S., & Gross, J. (2000). Cyclic Tesing of Steel Moment Connections with RBS or Weled Haunch. *Journal of Structural Engineering*, (January), 57–68.

UCB. (2003). *U.C. Berkeley Seismic Guideline*. University of California, Berkeley.

Wongpakdee, N. (2011). *Performance-Based Seismic Design and Evaluation of Buckling Restrained Knee Braced Truss Moment Frames*. King Mongkut's University of Technology Thonburi, Bangkok, Thailand.

Wongpakdee, N., Leelataviwat, S., Goel, S. C., & Liao, W.-C. (2014). Performance-Based Design and Collapse Evaluation of Buckling Restrained Knee Braced Truss Moment Frames. *Engineering Structures*, *60*, 23–31. Retrieved from http://www.sciencedirect.com/science/article/pii/S0141029613006019

Yang, T. Y., Li, Y., & Leelataviwat, S. (2013). Performance-Based Design and Optimization of Buckling Restrained Knee Brace Truss Moment Frame. *Journal of Performance of Constructed Facilities*. Retrieved from http://ascelibrary.org/doi/abs/10.1061/(ASCE)CF.1943-5509.0000558

Yang, T. Y., Moehle, J. P., & Stojadinovic, B. (2009). *Performance Evaluation of Innovative Steel Braced Frames – PEER Report 2009/103*. Pacific Earthquake Engineering Research Center, College of Engineering, University of California, Berkeley.

Yang, T. Y., Moehle, J. P., Stojadinovic, B., & Kiureghian, A. Der. (2009). Seismic Performance Evaluation of Facilities : Methodology and Implementation. *Journal of Structural Engineering*, (October), 1146–1154.

Yoshino, T., & Karino, Y. (1971). Experimental Study on Shear Wall with Braces: Part 2. In *Summaries of technical papers of annual meeting. Architectural Institute of Japan papers* (pp. 403–404).

Appendices

Appendix A

The following design sample is based on prototype BRKBTMF with 63° BRB inclination as shown in Figure A.1.

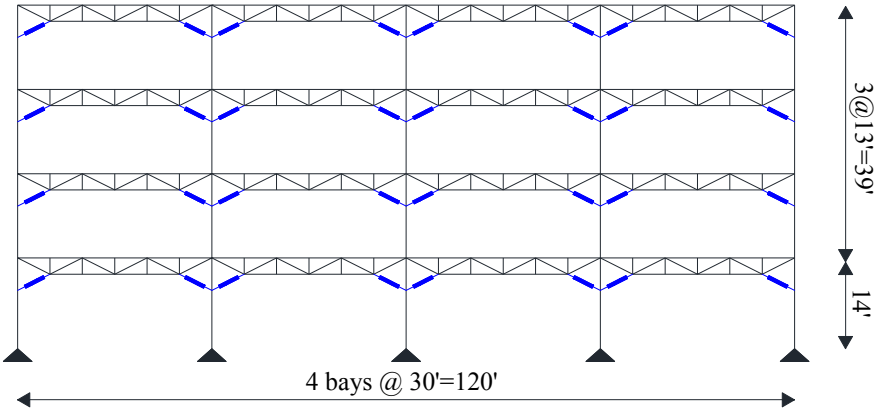

Figure A.1 Prototype BRKBTMF

A.1 Gravity Loads Calculation

The following gravity loads are assumed for the design of archetype structure (Goel and Chao, 2008).

Dead Load

Typical floor (Floor 2, 3, 4)	= 90 psf
Roof	= 85 psf

Live Load

Typical floor (Floor 2, 3, 4)	= 50 psf
Roof	= 20 psf

Building Envelope

Floor slab envelope (for dead load calculation)	= 182 x 122 ft. x ft.
Floor slab envelope (for live load calculation)	= 182 x 122 ft. x ft.

Dead loads (due to exterior curtain wall)

At the roof level with 10’ – 0’’ tributary height: Wwall	= 250 plf
At levels 3 and 4 with 13’ – 0’’ tributary height: Wwall	= 325 plf
At level 2 with 13’ – 6’’ tributary height: Wwall	= 338 plf

Floor Seismic Dead Weight (full structure)

Roof = (101.9 x 180 x 120) / 1000	= 2201 kips
Level 4 = (98.5 x 180 x 120) / 1000	= 2128 kips
Level 3 = (99.4 x 180 x 120) / 1000	= 2147 kips
Level 2 = (99.7 x 180 x 120) / 1000	= 2155 kips
Full structure	= 8631 kips

Beam Load Calculations (for exterior moment frame)

The exterior beams take the dead load from 16 feet of slab (which accounts for 1 foot for overhang). The live load is calculated based on a 15-ft tributary width only.

Uniformly distributed loads on the exterior beam:

Roof

From slab (dead load) = 0.085 x 16	= 1.36 kip/ft
From exterior wall (dead load)	= 0.25 kip/ft
From slab (live load) = 0.020 x 15	= 0.30 kip/ft

Level 3, 4

From slab (dead load) = 0.090 x 16	= 1.44 kip/ft
From exterior wall (dead load)	= 0.325 kip/ft
From slab (live load) = 0.050 x 15	= 0.75 kip/ft

Level 2

From slab (dead load) = 0.090 x 16	= 1.44 kip/ft
From exterior wall (dead load)	= 0.338 kip/ft
From slab (live load) = 0.050 x 15	= 0.75 kip/ft

Concentrated Loads at Column Lines (values for one exterior moment frame)

These loads are due to the transverse beams in the E-W direction as well as the exterior wall

Roof

Dead load (exterior column lines) = 016 x 4.75 x 0.085 + 2 x 16 x 10 x 0.025	= 14.46 kips
Live load (exterior column lines) = 15 x 3.75 x 0.020	= 1.125 kips
Dead load (interior column lines) = 0 + 30 x 10 x 0.025	= 7.5 kips
Live load (interior column lines) = 15 x 7.5 x 0.02	= 2.25 kips

Level 3, 4

Dead load (exterior column lines) = 016 x 4.75 x 0.090 + 2 x 16 x 13 x 0.025	= 17.24 kips
Live load (exterior column lines) = 15 x 3.75 x 0.050	= 2.8125 kips
Dead load (interior column lines) = 0 + 30 x 13 x 0.025	= 9.75 kips
Live load (interior column lines) = 15 x 7.5 x 0.05	= 5.625 kips

Level 2

Dead load (exterior column lines) = 016 x 4.75 x 0.090 + 2 x 16 x 13.5 x 0.025	= 17.64 kips
Live load (exterior column lines) = 15 x 3.75 x 0.050	= 2.8125 kips
Dead load (interior column lines) = 0 + 30 x 13 x 0.025	= 10.125 kips
Live load (interior column lines) = 15 x 7.5 x 0.05	= 5.625 kips

Load Combination (gravity load only)

Loads on beams and columns are calculated based on ASCE7:

$(1.2 + 0.2S_{DS})DL + 0.5LL$

Live loads is reducible and assumed 60% of this value. S_{DS} = 1.27g (UCB, 2003), therefore:

(1.2 + 0.2 x 1.27) DL + 0.5 x 0.6 LL = 1.45DL + 0.3LL

Summary of gravity loading (pattern loadings is not accounted for)

w_1 (level 2) = 1.45 x (1.44 + 0.338) + 0.3 x 0.75	= 2.80 kip/ft
w_2 (level 3, 4) = 1.45 x (1.44 + 0.325) + 0.3 x 0.75	= 2.78 kip/ft
w_3 (roof) = 1.45 x (1.36 + 0.25) + 0.3 x 0.3	= 2.42 kip/ft
L_1 (level 2) = 1.45 x 17.64 + 0.3 x 2.8125	= 26.42 kips
L_2 (level 2) = 1.45 x 10.125 + 0.3 x 5.625	= 16.37 kips
L_3 (level 3, 4) = 1.45 x 17.24 + 0.3 x 2.8125	= 25.84 kips
L_4 (level 3, 4) = 1.45 x 9.75 + 0.3 x 5.625	= 15.80 kips
L_5 (roof) = 1.45 x 14.46 + 0.3 x 1.125	= 21.30 kips
L_6 (roof) = 1.45 x 7.50 + 0.3 x 2.25	= 11.55 kips

The loading of the building is shown in Figure A.2.

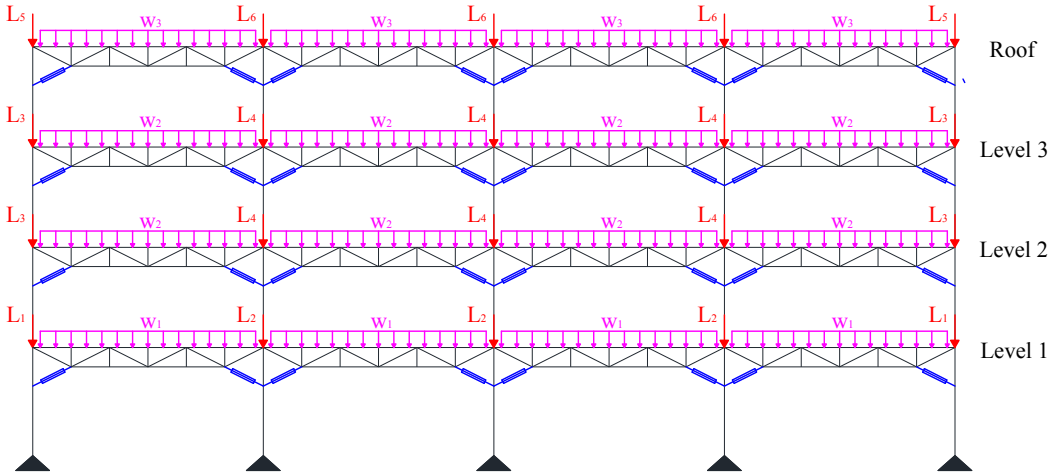

Figure A.2 Loading of the prototype building

A.2 Design Base Shear Calculation

The design base shear for the building is determined by satisfying two performance objectives, which are (1) maximum 2.5% story drift ratio under 10/50 hazard level, and (2) maximum 3.5% story drift ratio under 2/50 hazard level. The design spectra have been shown in Figure 4.2.

The period of the archetype structure is estimated 1.0 sec, the energy modification factor γ can be found from Figure 2.2 by using the structural period and structural ductility:

$$\mu_s = \frac{\theta_u}{\theta_y} = \frac{2.5}{0.75} = 3.33$$

On the other hand, the calculation of γ can follow the below Table A.1 (Lee, 2002; Newmark & Hall, 1982).

Table A.1 R_μ-μ-T relationship

Period Range	Ductility Reduction Factor
$0 \le T \le \frac{T_1}{10}$	$R_\mu = 1$
$\frac{T_1}{10} \le T \le \frac{T_1}{4}$	$R_\mu = \sqrt{2\mu_s - 1}\left(\frac{T_1}{4T}\right)^{2.513\log\left(\frac{1}{\sqrt{2\mu_s-1}}\right)}$
$\frac{T_1}{4} \le T \le T_1$	$R_\mu = \sqrt{2\mu_s - 1}$
$T_1^{'} \le T \le T_1$	$R_\mu = \frac{T\mu_s}{T_1}$
$T_1 \le T$	$R_\mu = \mu_s$

Note: $T_1 = 0.57\,\text{sec}$, $T_1^{'} = T_1\sqrt{2\mu_s - 1} / \mu_s$

In this case, $R_\mu = \mu_s = 3.33$

$$\gamma = \frac{2\mu_s - 1}{R_\mu^2} = \frac{2(3.33) - 1}{3.33^2} = 0.51$$

The lateral force distribution factor, λ, and the story shear ratio, β is calculated by **Equation 2.7** to **Equation 2.9**. The distribution follows Chao et al. (2007).

$$\alpha_0 = \frac{8\pi^2}{T^2 g}\left(\sum_{i=1}^{n}\lambda_i h_i\right)\theta_p = \frac{8(3.14)^2}{(1)^2(32.2)}(42.45)(0.025 - 0.0075) = 1.821$$

Therefore, the base shear coefficient for the building at 2/3MCE is:

$$\frac{V_y}{W} = \frac{-\alpha_0 + \sqrt{\alpha_0^{\,2} + 4\gamma S_a^2}}{2} = \frac{-1.821 + \sqrt{1.821^2 + 4(0.51)(0.78)^2}}{2} = 0.157$$

$V_y = 0.157W = 0.157(8631/2) = 677.5kips$ per frame

Following the same procedure, the design base shear can be calculated correspondingly. Table A.2 shows the design result for both performance objectives.

Table A.2 Design parameters

Design Parameters	10/50 hazard level (2/3MCE)	2/50 hazard level (MCE)
S_a	0.78	1.18
T	1.0	1.0
Yield Drift Ratio, θ_y	0.75	0.75
Target Drift Ratio, θ_u	2.5	3.5
Inelastic Drift Raio, $\theta_p = \theta_u - \theta_y$	1.75	2.75
R_μ	3.33	4.67
γ	0.51	0.38
α	1.82	2.86
V/W	0.158	0.174
Design base shear V (kips) per frame	683	751

The equivalent lateral forces can be calculated by **Equation 2.7** to **Equation 2.9**. The result of the lateral forces is shown on Table A.3.

Table A.3 Lateral force distribution calculation

Floor	h_i (ft)	w_i (k)	$w_i h_i$	$\sum w_i h_i$	β_i	λ_i	F_i (k) per frame	F_i' (k) per bay
Roof	53	2201	116653	116653	1.000	0.505	379	94.8
4	40	2128	85120	201773	1.508	0.257	193	48.2
3	27	2147	57969	259742	1.823	0.159	119	29.8
2	14	2155	30170	289912	1.979	0.079	59	14.9

*Sample calculation:

$$\beta_4 = \frac{V_i}{V_n} = \left(\frac{\sum_{j=i}^{n} w_j h_j}{w_n h_n} \right)^{0.75T^{-0.2}} = \left(\frac{116653 + 85120}{116653} \right)^{0.75(1)^{-0.2}} = 1.508$$

$$\lambda_4 = (\beta_4 - \beta_5)\left(\frac{w_n h_n}{\sum_{j=1}^{n} w_j h_j}\right)^{0.75T^{-0.2}} = (1.508-1)\left(\frac{116653}{289912}\right)^{0.75(1)^{-0.2}} = 0.257$$

$$F_4 = \lambda_4 V_y = 0.257 \times \max(677.5, 750.9) = 193 kips$$

$$F_4^{'} = F_4 / 4 = 193/4 = 48.2 kips$$

A.3 Element Design

A.3.1 BRB Design

The energy equilibrium is used to calculate the required strength for BRBs. The plastic energy of the building is equal to the energy as shown in the **Equation 2.10**. The required strength for the BRB is shown in Table A.4.

Table A.4 Design results of BRBs

Floor	Required yield strength, $\frac{P_y}{\phi}$	P_y	Maximum tension	Maximum compression
Roof	141	157	236	275
4	213	237	356	415
3	258	286	430	501
2	280	311	467	544

* Sample calculation:

$$\delta_p = (D_0 \sin\alpha + l_1 \cos\alpha)\theta_p = (5 \times \sin(63.4) + 5 \times \cos(63.4)) \times 0.0275 = 0.123$$

$$E_p = V_y\left(\sum_{i=1}^{n} \lambda_i h_i\right)\theta_p = [(94.8+48.2+29.8)\times 13 + 14.9 \times 14] \times 0.0275 = 219.1 k - ft$$

$$N_{BRBroof} = \frac{E_p}{2\sum_{i=1}^{n}(\beta_i)(\delta_p)} = \frac{219.1}{2(\sum_{i=1}^{n}\beta_i)(0.123)} = 141 kips$$

$$N_{BRBroof} = 1.00 \times 141 = 414 kips$$

$$N_{BRB4} = 1.51 \times 141 = 213 kips$$

$$P_{y4} = \frac{N_{BRB4}}{\phi} = \frac{213}{0.9} = 237 kips$$

$$P_{\max}^{+} = \omega R_y P_y = 1.5(1)(237) = 356 kips$$

$$P_{\max}^{-} = \omega \beta R_y P_y = 1.5(1.17)(1)(237) = 415 kips$$

A.3.2 Truss Design

Trusses are the non-yielding elements in the building. The truss components can remain elastic during the earthquake event and require no repairing. In order to achieve that, the truss should be designed against the maximum forces created by the BRBs. AISC 361 (2010) permits that the maximum compression and tension in the BRB can be calculated by the product of yielding strength and overstrength factor of BRBs. Furthermore, the overstrength factor can be obtained through component testing permitted by AISC 361 (2010).

The internal forces in trusses can be calculated by using the free body diagram shown in Figure A.2. P_w is the gravity load from the corresponding tributary area of the truss and P_{BRB}^{+} and P_{BRB}^{-} are the maximum tension and compression from BRB. Since the BRB has been oriented to 90˚, the forces to the truss will be horizontal. In this case, the truss on the 4th floor was selected for sample calculation, where $P_w = 13.5 kip$, $P_{BRB}^{+} = 356 kips$ and $P_{BRB}^{-} = 415 kips$. The demands on the trusses are determined through force equilibrium as shown in Figure A.3, and the members can be designed correspondingly.

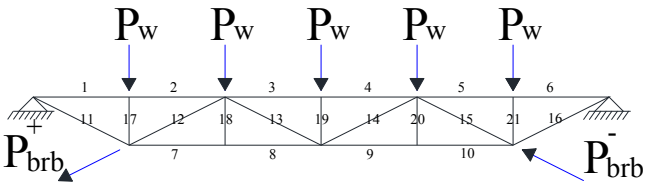

Figure A.3 Truss free body diagram for prototype BRKBTMF

Table A.5 Internal forces of truss members

Member	Due to gravity (kips)	Due to BRB forces (kips)	Combination	Maximum demands
1	-67.5	-459.8	-527.3	
2	-67.5	-459.8	-527.3	
3	-121.5	0.0	-121.5	
4	-121.5	0.0	-121.5	
5	-67.5	459.8	392.3	459.8
6	-67.5	459.8	392.3	-527.3
7	108.0	177.8	285.8	
8	108.0	175.4	283.4	
9	108.0	-282.0	-174.0	
10	108.0	-282.0	-174.0	
11	75.5	99.5	175.0	
12	-45.3	256.0	210.7	
13	15.1	-256.0	-240.9	271.1
14	15.1	256.0	271.1	-301.3
15	-45.3	-256.0	-301.3	
16	75.5	-158.8	-83.3	
17	-13.5	0.0	-13.5	
18	-13.5	0.0	-13.5	
19	-13.5	0.0	-13.5	0.0
20	-13.5	0.0	-13.5	-13.5
21	-13.5	0.0	-13.5	

* Design sample of top chord:

Compression demands: 527.3 kips

Tension demands: 459.8 kips

Section selection: 2MC10x25 with 3/8 in. separation at every l/3 of each segment length.

Section properties: $A = 14.7 in^2$; $r_x = 3.87 in$; $r_y = 1.51 in$

$$\frac{kl}{r_x} = \frac{5 \times 12}{3.87} = 15.5; \frac{kl}{r_y} = \frac{5 \times 12}{1.51} = 39.7$$

From AISC (2010b) Section E3:

$$\left(\frac{kl}{r}\right)_{\max} = 39.7 < 4.71\sqrt{\frac{E}{F_y}} = 4.71\sqrt{\frac{29000}{50}} = 113.4$$

$$F_e = \frac{\pi^2 E}{\left(\frac{KL}{r}\right)^2} = \frac{3.14^2 (29000)}{(39.7)^2} = 181.4$$

$$F_{cr} = \left[0.658^{\frac{F_y}{F_e}}\right] F_y = \left[0.658^{\frac{50}{181.4}}\right] \times 50 = 44.6$$

Compression capacity:

$$\phi_c P_n = \phi_c F_{cr} A_g = 0.9 \times 44.6 \times 14.7 = 590 kips > 527 kips$$

Tension capacity:

$$\phi_t P_n = \phi_c F_y A_g = 0.9 \times 50 \times 14.7 = 661.5 kips > 460 kips$$

A.3.3 Column Design

Columns are also capacity designed against BRB. The demands of the columns are from both BRBs and truss. The additional lateral loads demand from **Equation 2.6** is also considered during the design. The column tree is shown in Table A.4

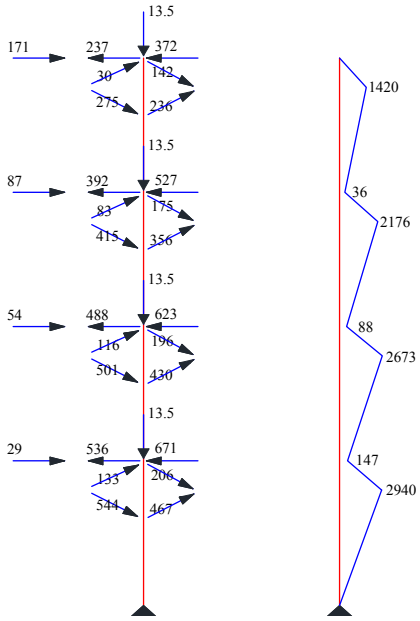

Figure A.4 Sample column tree [unit: kip-ft]

*** Sample calculation for 3rd column design check**

Moment demand: 2176 kips-ft

Axial force demand: 409kips

Shear demand: 261kips

Equivalent inertia of truss girder at third floor:

$$\sum(I + Ad^2) = 4(110) + 4(7.45)(15)^2 = 7055in^4$$

Equivalent inertia of truss girder at second floor:

$$\sum(I + Ad^2) = 4(126) + 4(8.37)(15)^2 = 8037in^4$$

Column at third level: W24x229 ($I = 7650in^4$, $r_x = 10.7in$; $r_y = 3.11in$)

Column at second level: W24x306 ($I = 7650in^4$)

Shear strength of column:

From AISC (2010b) Section G2:

$$\frac{h}{t_w} = 22.5 < 1.10\sqrt{\frac{k_v E}{F_y}} = 1.10\sqrt{\frac{5(29000)}{55}} = 56.5$$

$$\therefore C_v = 1$$

$$\phi_v V_n = \phi_v 0.6 F_y A_w C_v = 0.9 \times 0.6 \times 55 \times 0.96 \times 20.75 \times 1 = 592 kips > 261 kips$$

Compression strength of column:

$$G_a = \frac{\sum (EI/L)_c}{\sum (EI/L)_b} = \frac{7650/13 + 7650/13}{7055/30 + 7055/30} = 2.50$$

$$G_a = \frac{\sum (EI/L)_c}{\sum (EI/L)_b} = \frac{7650/13 + 10700/13}{8037/30 + 8037/30} = 2.63$$

$k_x = 1.75$ (based on alignment chart – sideways uninhibited)

$k_y = 1.0$ (assuming the column is laterally braced in y-direction)

$$\frac{kl}{r_x} = \frac{1.75 \times 13 \times 12}{10.7} = 25.5\,;\ \frac{kl}{r_y} = \frac{13 \times 12}{3.11} = 50.2$$

From AISC (2010b) Section E3:

$$\left(\frac{kl}{r}\right)_{\max} = 50.2 < 4.71\sqrt{\frac{E}{F_y}} = 4.71\sqrt{\frac{29000}{55}} = 108.1$$

$$F_e = \frac{\pi^2 E}{\left(\frac{KL}{r}\right)^2} = \frac{3.14^2 (29000)}{(50.2)^2} = 113.5$$

$$F_{cr} = \left[0.658^{\frac{F_y}{F_e}}\right] F_y = \left[0.658^{\frac{55}{113.5}}\right] \times 55 = 44.9$$

Compression capacity:

$$\phi_c P_n = \phi_c F_{cr} A_g = 0.9 \times 44.9 \times 67.2 = 2715.6 kips > 409 kips$$

Flexural strength of column:

$$\frac{b}{t} = 7.58 < 0.38\sqrt{\frac{E}{F_y}} = 0.38\sqrt{\frac{29000}{55}} = 8.73$$

$$\frac{h}{t_w} = 22.5 < 1.49\sqrt{\frac{E}{F_y}} = 1.49\sqrt{\frac{29000}{55}} = 34.2$$

The section is compact.

$$L_p = 1.76 r_y \sqrt{\frac{E}{F_y}} = 1.76(3.11)\sqrt{\frac{29000}{55}} = 125.7in \quad \text{and} \quad L_b = 12(13-5) = 96 < L_p = 125.7in$$

$\therefore$ The limit state of lateral torsional buckling does not apply.

$$\phi_b M_n = \phi_b M_p = \phi_b F_y Z_x = 0.9(55)(675) = 3341k-ft > 2176k-ft$$

Since $\frac{P_u}{\phi_c P_n} = 0.15 < 0.2,$ the following equation should be satisfied.

$$\frac{P_r}{2\phi_c P_n} + \left(\frac{M_{rx}}{\phi_b M_{nx}}\right) \le 1.0$$

where,

$M_r = B_1 M_{nt} + B_2 M_{lt}$ and $P_r = P_{nt} + B_2 P_{lt}$

For members in which $B_1 \le 1.05$, it is conservative to amplify the sum of the non-sway and sway moment by the B_2 amplifier, in other words, $M_r = B_2(M_{nt} + M_{lt})$.

$$B_2 = \frac{1}{1 - \frac{\alpha \sum P_{nt}}{\sum P_{e2}}} \ge 1$$

where α=1.0 (LRFD), $\sum P_{nt}$ =total vertical load supported by the story unsing LRFD load combinations, including gravity column loads, kips

$$\sum P_{e2} = R_M \frac{\sum HL}{\Delta_H}$$

where $R_M = 0.85$ for moment-frame and combined systems, unless a larger value is justified by analysis. $\sum H =$ story shear produced by the lateral forces used in compute ΔH , kips. $\Delta H =$ first-order Inter-story drift due to lateral force, in.

Therefore, $\sum P_{e2} = 0.85\frac{1144.3}{0.035} = 27790 kips$

$$B_2 = \frac{1}{1-\frac{(1)(4329)}{27790}} = 1.2$$

$$\frac{B_2 P_r}{2\phi_c P_n} + \left(\frac{B_2 M_{rx}}{\phi_b M_{nx}}\right) = \frac{1.2(409)}{2(2715)} + \left(\frac{1.2(2176)}{3341}\right) = 0.87$$

Therefore W24x229 meets the demand requirement. The sizes of BRB, truss and columns are summarized in Table A.6.

Table A.6 Sizes of structural components

Fl.	BRB Strength (kips)	Column Sizes		Truss			
		Exterior	Interior	Top/Bottom Chord	Diagonal Chord	Vertical Chord	Ext. Vert. Chord
4	172	W24x207	W24x229	2MC8x18.7	2MC6x12	L3.5x3.5x 5/16	2L3.5x3.5x 5/16
3	259			2MC10x25	2MC6x15.3	L3.5x3.5x 5/16	2L3.5x3.5x 5/16
2	312	W24x279	W24x306	2MC10x28.5	2MC6x15.3	L3.5x3.5x 5/16	2L3.5x3.5x 5/16
1	339			2MC10x28.5	2MC8x18.7	L3.5x3.5x 5/16	2L3.5x3.5x 5/16